NASA CR-72440

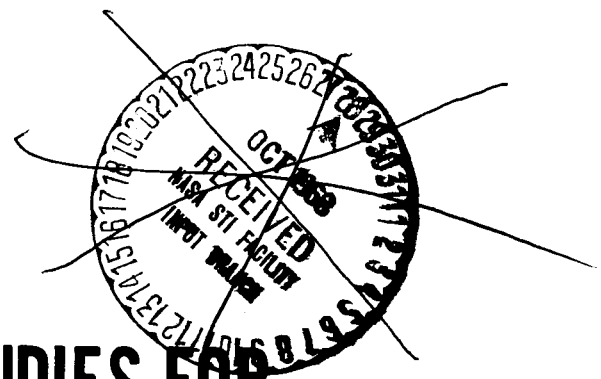

DISCHARGE CHAMBER STUDIES FOR MERCURY BOMBARDMENT ION THRUSTERS

by

W. Knauer, R.L. Poeschel, H.J. King, and J.W. Ward

CONTRACT NAS 3-9703

prepared for

NATIONAL AERONAUTICS AND SPACE ADMINISTRATION

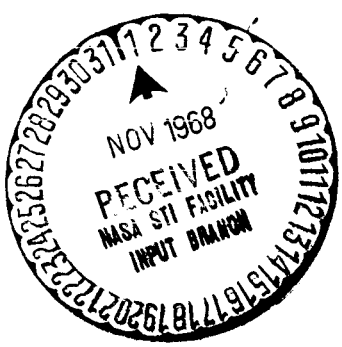

HUGHES RESEARCH LABORATORIES
A DIVISION OF HUGHES AIRCRAFT COMPANY
3011 MALIBU CANYON ROAD
MALIBU, CALIFORNIA 90265

NASA CR-72440

FINAL REPORT

DISCHARGE CHAMBER STUDIES FOR MERCURY BOMBARDMENT ION THRUSTERS

by

W. Knauer, R. L. Poeschel, H. J. King, and J. W. Ward

prepared for

NATIONAL AERONAUTICS AND SPACE ADMINISTRATION

September 1968

CONTRACT NAS 3-9703

Technical Management
NASA Lewis Research Center
Cleveland, Ohio

HUGHES RESEARCH LABORATORIES
A Division of Hughes Aircraft Company
3011 Malibu Canyon Road
Malibu, California

TABLE OF CONTENTS

LIST OF ILLUSTRATIONS

I. INTRODUCTION

A. PROGRAM OBJECTIVES

The performance of Kaufman thrusters has improved dramatically in recent years. The energy expended in the discharge of the original thruster was about 1000 eV/expelled ion at a propellant utilization of about 90%. A number of investigators[1-5] have succeeded in reducing this expenditure considerably. About a year ago, when this contract was initiated, the energy consumption of the most advanced thrusters (of the NASA-SERT II type) had been reduced to less than 250 eV/ion at 90% propellant utilization. Even at this point the energy loss per ion remained orders of magnitude above the absolute low limit at which not more than the ionization energy (10.44 eV for mercury) is consumed. It was thus highly likely that additional energy could be saved, and the objective of this contract was to achieve further optimizations of the thruster discharge.

Almost all of the earlier advances had been accomplished by empirical parameter studies, with little regard for the underlying discharge mechanism. This suggested that a more physically oriented approach might have merit. Accordingly, a program was formulated which comprised the following general tasks:

1. parameter studies
2. discharge diagnostics
3. discharge theory
4. optimization efforts.

It was hoped that the first three tasks would combine to provide a high level of understanding which ultimately would aid the optimization effort.

B. TECHNICAL SUMMARY

We believe that the physical approach has been very successful. The results obtained under the contract may be summarized briefly as follows:

1. Substantial new knowledge has been gained concerning the properties of the hollow cathode plasma and the interaction of this plasma with the discharge plasma. These findings are of considerable importance to (a) the understanding and prevention of hollow cathode-tip sputtering, and (b) the "decoupling" between hollow cathode and discharge plasmas. The latter is desirable because it leads to a lower rate of electron injection into the discharge plasma,[1] which aids performance and eliminates a control problem.

2. A detailed understanding of the thruster discharge mechanism has been gained. Based on this understanding, specific design rules for high performance thrusters have been postulated.

3. A thruster optimization effort has been conducted with two 15 cm diameter thrusters. Both thrusters employed electromagnets and both were operated without neutralizers. Using the design rules mentioned above, this effort led to

   a. an optimized oxide cathode thruster configuration with the following performance characteristics:

discharge chamber losses	154 eV/ion
propellant utilization	82 %
beam current	271 mA
beam potential	3 kV
decel potential	2 kV
discharge voltage	42.5 V

   b. a new hollow cathode thruster configuration, incorporating radial magnetic fields, with the following performance characteristics:

discharge chamber losses	190 eV/ion
propellant utilization	90 %
beam current	380 mA
beam potential	3 kV
decel potential	2 kV
discharge potential	42.5 V

   This new configuration has the following advantages:

   - a substantially increased ion beam uniformity. The ion beam of the radial field thruster is approximately twice as uniform as that of the NASA SERT-II thruster; therefore, it utilizes the perveance of the ion optics approximately twice as well (for a precise definition of the term "perveance utilization" see Section II.F). The radial field thruster thus can provide nearly twice the thrust.

   - a center post along the discharge axis can serve as a support for the ion optical system and a centrally mounted neutralizer.

   - a shorter length, using less space and weight.

The results summarized above and described in detail below were extracted from a large volume of experimental data. To keep this report concise, less meaningful experiments will be reported only briefly; complete sets of the corresponding data will be collected in a separate data book, several copies of which will be submitted to NASA together with this report.

The results will be presented under the headings 'NASA-SERT II Thruster", "Oxide Cathode Thruster", "Hollow Cathode Thruster", and "Radial Field Thruster". Under "NASA-SERT II Thruster", measurements

are reported which were obtained with a NASA supplied thruster. In part, these measurements were intended to serve as a standard of comparison for the performance obtained with various thruster configurations explored under the contract. In part, they were performed upon request by NASA to gather more information about the SERT-II thruster. Included among the latter experiments were a parameter study using different types of cathodes and a diagnostic study.

During most of the contract period, separate investigations were conducted with oxide and hollow cathode thrusters. The properties and problems of the two configurations were sufficiently different to warrant this procedure. It should be stressed, however, that these investigations were not independent, even though they were separate. Especially toward the end of the contract, when a more general understanding of the discharge behavior evolved, considerable interaction existed between both.

II. EXPERIMENTAL PROGRAM

A. APPARATUS

In this section, we describe the apparatus which has a direct bearing on the experimental results. The thruster experiments were performed in three cryogenically pumped vacuum tanks of 2, 5, and 9 ft. diameter. Ambient pressure in these chambers during thruster operation was always less than 10^{-6} Torr, and typically was on the order of 2 to 5 x 10^{-7} Torr. Ion current was collected with a water cooled, stainless steel target and neutralizers were not employed for any experiments. Two sets of power conditioning were used, both sets using the metering circuits and connections shown schematically in Fig. 1. The location of the meters in this schematic diagram defines the parameters mentioned throughout the text.

Two experimental thrusters were designed to facilitate parameter variation and diagnostics in the discharge chamber studies. Figure 2 shows the essential features of these thrusters. The magnetic field is generated by a solenoid constructed from eight segments, each having 50 turns. These segments can be separated for insertion of soft iron "pole pieces" or disconnected altogether to provide a variety of magnetic configurations. The cathode and its supports are relatively easy to remove or modify, thus making it relatively simple to change cathodes or cathode locations. The feed tubes are connected to the feed manifold with "Swagelok" fittings to permit easy change of the location or direction of propellant injection into the discharge chamber. The ion extraction optics, anode, cathode support electrode, and feed tubes are all isolated electrically in order to permit independent monitoring of currents. In addition, cylindrical, insulated electrodes can be fitted tightly inside the anode to monitor the anode current distribution or to serve as electron confining devices by operation at cathode potential. Provision is also made for inserting a probe support rod through the cathode end of the thruster chamber, as shown in Fig. 2. The several types of probes are described in Section II-B. The oxide cathodes used under the contract were constructed of directly heated nickel mesh, wound in a spiral, and sprayed with a nickel encapsulated barium carbonate. The latter material was prepared by the apparatus developed under an earlier NASA contract[6] using a technique described by D. M. Maurer and C. M. Pleass.[7] Figure 3 shows a photograph of a cathode of this type. The cathodes used for hollow cathode thruster operation were supplied by NASA LeRC, and the cathode, cathode pole piece, baffle, and keep-alive electrode are described by R. T. Bechtel, et. al., in Ref. 3 (shown in Fig. 3 of that report). Two types of ion extraction optics were used. Their critical dimensions are given in Table I. Type B optics was supplied by NASA-LeRC for use with the SERT-II thruster and was adapted to the experimental thrusters.

The final experimental thruster configuration tested was a modification of the thruster chamber shown in Fig. 2 . A radial magnetic field was generated by means of a center post; in addition, the role of anode and cathode was interchanged. A complete set of detailed drawings for

this configuration is supplied with this report. Figure 4 shows photographs of this thruster chamber (a) with optics removed and (b) with both optics and part of the center post (serving also as a combination of pole piece and baffle) removed. The propellant feed tubes have small orifices directed toward the rear of the chamber. The feed manifold and electrical isolator heater also can be readily identified from Fig. 4. The electrical isolator serves to separate electrically the thruster and reservoir. This was accomplished by spacing a sufficient number of optically dense wire mesh discs within an insulating segment of the feed line to maintain the voltage drop across each interdisk spacing below the Paschen minimum. An oxidized stainless steel mesh was used as a phase separator between the liquid and vapor phases of the propellant. Control over the propellant feed rate was provided by a thermostatically regulated heater. The propellant feed rate was determined via periodic volume measurements of the mercury delivered from the propellant reservoir. Two such systems were used: (1) a spring-loaded, piston-driven diaphram system, and (2) a gravity flow, calibrated pipette system. The pipette system was read directly in milliliters per hour, while the piston system employed a dial indicator to monitor piston travel per hour. Both systems proved to be reliable.

B. DIAGNOSTIC TECHNIQUES

1. Langmuir Probe

The Langmuir probe technique used for the measurements in this investigation will be discussed first. Two probe configurations, shown in Fig. 5 were used to probe the thruster discharge plasma. The probe positioning method is shown in Fig. 6(a). The probe shown as No. 1 in Fig. 5 was capable of operation as an emissive probe when heated to emissive temperature by passing current through the wire loop of the probe. In principle, the plasma or space potential may be obtained unambiguously by superposition of the voltage-current characteristic of this probe operated as an emissive probe on the characteristic of the same probe operated as a cold collector. Figure 6(b) shows an example of these characteristics and the method of identifying the plasma potential. The emissive probe characteristic separates from the nonemissive characteristic when the probe potential becomes less than the plasma potential because the emissive probe then emits electrons into the plasma. Consequently, this point of separation can be used to indicate the plasma potential,[8] and the nonemissive probe characteristic can be analyzed in the usual manner.[9] In practice, it was difficult to use emissive probes because heating the loop to emission temperature changed the mechanical contact with and the electrical conductivity of the ceramic probe insulator; this caused an increase in the collection area and a corresponding increase in collected electron current, even at probe potentials above plasma potential. This can be avoided only by carefully centering the probe wire in the insulator (which is difficult to accomplish). For this reason, and because of frequent destructive arcings when the probe was operated as an emitter, this technique was abandoned and all probe measurements were made with the probe as a nonemissive collector.

The first probe measurements were made with the type 1 probe, using a manual, point-by-point method of obtaining the probe voltage-

current characteristic (varying the probe voltage manually and reading the probe voltage and current on meters). The probe characteristics immediately disclosed the existence of a non-Maxwellian distribution of electron energies in the discharge plasma. Consequently, the analytical technique of Strickfaden, et. al.,[10,11] was attempted and found to be applicable. This technique is based on the assumption of the existence of two species or components of plasma electrons: monoenergetic primary electrons from the cathode, and electrons with a Maxwellian energy distribution from ionization of neutrals. The electron current collected by the probe can thus be expressed in two components as

$$i_{probe} = i_{primary} + i_{maxwellian}$$

For retarding potentials, these components may be expressed mathematically as

$$i_{primary} = A n_{pr} \left(\frac{2eV_{pr}}{m_e}\right)^{1/2} \left(1 + \frac{V}{V_{pr}}\right), \quad \left|\frac{V}{V_{pr}}\right| < 1 \qquad (1)$$

and

$$i_{maxwellian} = A n_m e \left(\frac{kT_e}{2\pi m_e}\right)^{1/2} \exp\left(\frac{eV}{kT_e}\right), \quad V \leq 0 \qquad (2)$$

where

A	$\equiv$	collecting area of probe
T_e	$\equiv$	temperature associated with Maxwellian component of plasma electrons
n_m	$\equiv$	density of Maxwellian component of electrons
n_{pr}	$\equiv$	density of primary component of electrons
eV_{pr}	$\equiv$	average energy of primary electrons
e	$\equiv$	electronic charge
m_e	$\equiv$	electronic mass
V	$\equiv$	potential of probe measured with respect to plasma potential.

When eV_{pr} is appreciably larger than kT_e it is relatively simple to separate the two components and obtain the desired quantities through (1) and (2). On a linear scale the voltage-current characteristic would appear as shown in Fig. 7(a). By drawing the linear tangent to the characteristic at the high retarding potential portion of the curve, the Maxwellian component of the current can be separated from the primary compound as shown. Replotting this Maxwellian component on a semilogarithmic scale as shown in Fig. 7(b) locates V_{plasma} and yields the plasma density using (1) and (2)

(T_e and V_{pr} can be obtained directly from the voltage-current characteristics and the component densities computed from the values of the current components, shown in Fig. 7(a), at V_{plasma}). This method of analysis requires that the primary electrons be monoenergetic and have an isotropic velocity distribution in order to separate the electronic components by means of the linear tangent. A number of probe characteristics were obtained which do not have a well-defined linear region; consequently, an attempt was made to employ a probe which measures total energy. The configuration attempted was that of a Faraday cup probe with a hemispherical collector. This probe failed because its physical size severely perturbed the discharge, and no data were collected. As a result, the two-component electron analysis was used throughout the study.

Because a linear display of the voltage-current characteristic is required for data analysis, this method lends itself to data recording by an x-y recorder. Figure 8 shows a block diagram of the components used, to collect data with the type 2 probe. This system has the advantage of being controlled by grounded instruments; thruster operation thus is continuous during measurement. The characteristics of the equipment essential to successful operation are

1. The dc power supply is regulated (constant voltage) against load changes and the voltage output is linearly proportional to the resistance of the programming resistor

2. The clamp-on milliameter has an output which is linear with respect to input.

The voltage and current meters shown in the high voltage circuit provide a constant check on the calibration. The wire which carried the probe current is looped 10 times through the probe of the clamp-on milliameter to improve sensitivity (only one loop is shown). Mechanical linkage between the x-axis potentiometer and the variable programming resistor is achieved with a standard piece of electronic hardware - a geared, right angle shaft coupling, and a fiber (insulating) shaft. With this set of equipment, Langmuir probe data can be collected quite rapidly, thus insuring a minimum variation of discharge conditions. Good reproducibility is also obtainable.

2. Faraday Cup Probe

A Faraday cup probe was used to determine the extracted ion beam current density profile. Figure 9 shows an example of the type of probe used. The main objective of the Faraday cup is to return secondary electrons resulting from the impact of ions on the collecting surface, thus rendering the current measurement more accurate. In accomplishing this, the probe of Fig. 9 is also made highly directional. To correct this, a spherical probe with spherical retarding screen was constructed, however, there was insufficient time for testing this device.

3. Magnetic Field Maps

Magnetic field mapping with powdered iron has long been a method of demonstrating the presence of magnetic lines of force. When such a field map is made permanent, it becomes a useful (though qualitative) means for estimating the effectiveness of magnetic configurations. The technique for mapping the magnetic configuration of a thruster chamber is relatively simple. First, a polyethylene bag is used to protect the chamber from contamination by powdered iron. Next a smooth white piece of paper, cut to fit inside the thruster, is sprinkled lightly with powdered iron. This paper is then inserted carefully into the magnetic field of the chamber; once in place, it is tapped lightly until the pattern of the field lines is clearly visible. The powdered iron pattern is then carefully coated with a light spray of clear lacquer. When this coating has dried, the pattern may be removed and coated more heavily for greater permanence. An example of the results of this technique is shown in Fig. 10.

C. NASA SERT-II THRUSTER STUDIES

1. Performance Mapping

At the beginning of the contract a SERT-II type thruster, described in Ref. 2, was supplied by NASA LeRC for the purpose of establishing performance standards. This thruster was operated with three cathode types: (1) a NASA magazine type oxide cathode, (2) an oxide coated nickel spiral cathode, and (3) a hollow cathode. In all performance tests, the thruster was operated for a sufficient time to establish stability in neutral propellant flow rates, equilibrium temperature of components, and cathode emission. Chamber pressures were typically of the order of 5×10^{-7} Torr. Figure 11 shows performance mappings for thruster operation with the three cathode types. The performance of this thruster is generally very good. As will be seen below, the SERT-II thruster discharge has the desirable discharge plasma characteristics outlined in Section II-4.

2. Diagnostics

The first measurement made with the SERT-II thruster was a powdered iron mapping of the magnetic field. For the hollow cathode configuration a magnetic field map is presented in Fig. 10. Figure 12 shows a tracing of a similar mapping for the oxide cathode configuration and lists an array of measured values of axial magnetic field strengths. It is apparent that electrons which follow the indicated lines of force essentially "cover" the entire screen area. Based on the findings of Section II-4, it is also apparent that the extremely divergent magnetic configuration of the SERT-II thruster would deteriorate the performance if the propellant were introduced near the screen pole piece, as was found by Bechtel.[2]

The extracted ion beam profile, normalized to the central value, is shown in Fig. 13. This profile was measured with a Faraday cup probe at a plane 18 cm downstream from the extraction optics. This

profile differs only slightly from others measured in the experimental thrusters (except for the radial field thruster).

At the request of NASA LeRC, a set of Langmuir probe measurements was made in the SERT-II thruster. The probe used was similar to that used in the experimental hollow cathode thruster, and the results were strikingly similar. To provide a graphical illustration of probe results, the plasma density, the normalized plasma potential, and the Maxwellian electron temperature are shown in three-dimensional plots in Fig. 14(a), (b), and (c), respectively. Only one set of measurements was made inside the cathode pole piece because it was considered undesirable to modify the baffle or cathode pole piece to permit entry of the probe. It is apparent that the plasma density is relatively low, as was the case when the experimental thruster was operated with high transmission optics. The potential distribution is also seen to display a potential ridge near the anode and to have a gradient in the direction of the extraction screen; this prevents radial ion loss and tends to establish an ion drift toward the screen. The distribution of Maxwellian electron temperature indicates the region of the discharge in which primary electrons ionize neutrals and interact with the plasma electrons. This region which is characterized by higher electron temperature, can be seen in Fig. 14(c) to expand radially from cathode to screen in much the same manner that the magnetic field lines are seen to diverge.

D. OXIDE CATHODE THRUSTER

The objective of the oxide cathode thruster studies was to investigate thruster performance by parameter variation and to gain a physical understanding of the changes in discharge plasma properties effected by favorable parameter modifications. The following parameters were varied:

1. Magnetic field configuration and strength
2. Length of the discharge chamber
3. Cathode location
4. Propellant introduction
5. Ion extraction optics.

Diagnostic measurements were made for those parametric variations which displayed significant differences in thruster performance. The diagnostics included

1. Langmuir probe measurements in the discharge plasma
2. Faraday cup probe measurements in the extracted ion beam
3. Powdered iron magnetic field maps
4. Current measurements in isolated segments of the discharge chamber electrodes.

The parametric studies have shown that improved thruster performance results when an optimal combination of the above parameters is used. Consequently, any attempt to state an optimum value or configuration for any single parameter would be an oversimplification. Indeed, diagnostic measurements have shown that thruster configurations which

display superior performance have in common certain physical rather than configurational properties:

1. The plasma density is relatively uniform across the extraction screen and there are no exaggerated local maxima or "peaks" in the spatial density distribution.

2. The plasma potential is essentially constant over the discharge chamber, generally above anode potential, and displays a slight gradient toward the screen electrode. In addition, there is a slight rise in potential near the anode.

3. The plasma electron density is composed of a distinct high energy component of "primary" electrons from the cathode, and a low energy component arising from ionization of the neutral gas. This low energy component has a more or less Maxwellian energy distribution with an electron temperature of the order of 7 eV, while the primary component has an appreciable fraction of the energy associated with the anode voltage. The "Maxwellian" electron temperature is found to be essentially constant across the diameter at the screen for divergent field configurations.

1. Magnetic Field Variation Studies

A number of magnetic configurations were explored using the iron filing mapping technique described above under 'Diagnostic Techniques". The configurations displaying discernible differences were used in performance tests using a 13 cm long thruster chamber, standard reverse propellant injection, and Optic A (see Table I for details). The most representative performance mappings of these experiments are shown in Fig. 15. Figure 16 gives "tracings" of the magnetic field maps for four magnetic configurations with a set of axial magnetic field strength values for each configuration. The magnetic field lines diverge increasingly from 16A to 16D, with configuration 16A essentially a uniform field configuration. It is apparent that the performance of the thruster improves as the magnetic configuration becomes more divergent. Other configurations were tested which employed a variety of pole pieces at the cathode and screen; however, these experiments provided no additional significant results. If the current in coil number one was reversed, an extremely divergent magnetic configuration could be obtained; however, this permitted direct anode interception of cathode electrons, and the discharge could not be sustained. Because of the wide difference in both magnitude and shape of the performance mappings of magnetic configuration 16A and 16D, these configurations were selected for Langmuir probe diagnostic measurements.

It is well know that thruster performance is improved as the magnetic configuration is made to diverge from the cathode toward the screen. This is relatively easy to interpret physically because the trajectories of the primary electrons are spread over a larger volume of the discharge chamber, thereby "spreading out" the plasma generation volume

and consequently causing the plasma density distribution to be more uniform. It is obvious that extreme divergence will negate the confining effect of the magnetic field, if primary electrons have trajectories which intersect the anode. This will tend to extinguish the discharge. A magnetic field configuration which disperses (spatially) the primary electrons is also capable of lowering the over-all plasma density without increasing the probability that a neutral atom will cross the thruster chamber without being ionized. A lower plasma density means that there will be fewer Coulomb collisions and less transfer of energy between primaries and secondaries. Thus, distinct primary and Maxwellian electronic components remain in existence. It may be concluded, therefore, that an optimum magnetic configuration is one which diverges sufficiently to distribute the primary electrons more or less uniformly in the volume adjacent to the extraction screen, yet prevents direct or near direct interception by the anode.

Several magnetic configurations tested in this study (including a NASA LeRC SERT-II thruster, a cusped magnetic field configuration, and a radial magnetic configuration) all exhibit similar performance and are believed to be more or less equally effective in dispersing primary electrons uniformly across the face of the screen.

2. Discharge Chamber Length

The experimental thruster was operated with the entire cathode housing and discharge boundary electrode constructed to be continuously adjustable. The discharge chamber length could be adjusted from 4 to 20 cm during thruster operation. Performance mappings were made for a number of discharge chamber lengths and magnetic configurations, using standard reverse propellant injection and Optic A. The most significant results appear in Figs. 17 and 18. It is seen that performance varies more significantly with discharge chamber length in a uniform magnetic configuration (Fig. 17) than in a suitably divergent configuration (Fig. 18).

An additional finding is that in 15 cm diameter thrusters the magnetic field cannot be made sufficiently divergent to provide the above described, desired plasma spreading if the length-to-diameter ratio is less than 0.4.

3. Cathode Location

The cathode location experiments were performed in a uniform magnetic field thruster with optics A, a discharge chamber length of 13 cm, and standard reverse propellant injection. The oxide cathode was a directly heated nickel mesh, without heat shielding, and was mounted on the probe positioning mechanism so that it could be positioned at any desired axial or radial position within the chamber. Two types of experiments were performed. In the first type, the discharge chamber was operated at constant power and neutral flow and the extracted ion beam current was observed for each cathode location. The magnetic field strength was varied at each location, but it was ineffective in producing additional beam current if the central field strength was of the order of 20 gauss or more. Table VII gives the results of these experiments for two values of discharge power. After

it was discovered that an axial location is superior, performance mappings were made for several axial locations. These results are shown in Fig. 19.

In a uniform magnetic configuration, the best location for the cathode was found to be on the discharge chamber axis and in the plane of the discharge boundary opposite the extraction screen. This is understandable because an axial location provides equal diffusion lengths for the primaries to reach the anode. Furthermore, a more central location (between the extraction screen and the opposite electrode) will tend to divide the plasma into two plasma regions with that in the vicinity of the screen providing most of the ions for extraction and the other contributing only to losses.

4. Propellant Injection

A series of experiments was performed to determine the effects of various methods of propellant injection in both a relatively uniform and a relatively divergent magnetic configuration. These configurations are shown in Fig. 20. Both configurations use a soft iron cathode pole piece and have an effective chamber length of approximately 10 cm. All propellant injection experiments shown here were performed with ion extraction optics A (48% open area). Figure 21 shows the performance mappings for three modes of propellant injection. The forward or through-feed mode of injection is seen to be relatively poor. This is thought to result because too many neutrals are being fed into the chamber near the electron source. The distributed reverse feed consequently provided little improvement in the performance while the standard reverse was the best for the magnetic configuration 20A. Figure 22 shows that the opposite is the case for a divergent configuration such as 20B. Injection of neutrals near the point where the magnetic field lines intercept the anode (standard reverse feed) increases the discharge current and causes larger discharge losses. Injection of half of the propellant nearer the discharge center decreases the discharge losses, while more uniform distribution of the propellant injection (one half at one third anode radius, one half at two thirds anode radius) gives best performance.

These observations are relatively easy to interpret. With a uniform magnetic field configuration, primary electrons ionize efficiently in the center and any enhanced influx of neutrals there tends to increase the local plasma density. This leads to increase both Coulomb and neutral collision frequency on and near the discharge axis. Thus, primary electrons lose their energy rapidly to neutrals and to the Maxwellian component of electrons. Consequently, they have lost an appreciable portion of their energy before they have diffused very far radially. The plasma generation volume thus becomes relatively smaller, resulting in a more "peaked", diffusion dominated plasma density distribution. In a thruster with a divergent magnetic configuration, the energetic primaries are more or less evenly distributed in the volume adjacent to the extraction screen. It is not surprising, therefore, that performance is observed to improve when the propellant injection is also more evenly distributed. Moreover, because most of the anode current is found to be collected in a relatively small portion of the anode near the screen, it is understandable that injection of neutrals near this location will enhance the cross field mobility of the electrons there, causing an increase in discharge current with a resultant deterioration of performance.

5. Ion Extraction Optics

During the parameter studies with oxide and hollow cathode thrusters, it was noted that configurations similar to geometries tested at NASA LeRC generally gave poorer performance. The only evident difference was the ion-optical system. Therefore, the type A optics with an open area of 48% were replaced by the NASA LeRC SERT-II optics (here labeled type B) which have an open area of 71%.

Performance mappings with type B optics were made for the magnetic configurations 16A and 16D and standard reverse propellant injection. Figure 23 shows the results of these experiments together with the mappings for the same configuration with type A optics. It is apparent that installation of the type B optics provides a greater improvement in thruster performance than changing the magnetic configuration, and that operation with the type B optics is improved only slightly by changing from a uniform to a divergent magnetic configuration. It is interesting to note that for type A optics with a geometrical open area 48%, the ratio of extracted ion current to screen current is approximately 1.5, corresponding to about 60% "effective" open area, if used in configuration 16D; it is only 1.2, equivalent to 53% effective transmission, for configuration 16A. Type B optics has a geometrical open area of 71%, and the ratio of extracted ion current to screen current was found to be approximately 7 (or 87.5% effective open area) for either magnetic configuration.

The change in ion optics from low to high transmission originally was not meant to be part of the discharge study. It was intended to upgrade the over-all thruster performance under use of the latest SERT-II components. Analysis of Langmuir probe data disclosed, however, that the ion optical configuration is of major importance to the discharge properties. Indeed, we found that ion optical modifications can lead to more significant changes in discharge behavior than does the transition from uniform to divergent B-field. This is reflected in the observed performance changes. The transition from an ion optical system with 48% open area to one with 71% open area improved the performance of a uniform magnetic field thruster from 254 eV/ion to 178 eV/ion (90% propellant utilization). In contrast, the change from a uniform to a divergent magnetic configuration reduced the energy expenditure more modestly from 254 eV/ion to 210 eV/ion.

Large performance improvements associated with ion optical changes were reported also by R. T. Bechtel[2] and by T. D. Masek and E. V. Pawlik.[1] In their cases the performance improved from 570 eV/ion to 280 eV/ion (80% propellant utilization), and from 540 eV/ion to 130 eV/ion (90% propellant utilization) respectively.

These three thrusters differ in many respects, including thruster size, propellant injection mode, and cathode type. However, they have in common that the improvements are associated with ion optical changes toward higher transparency for either ions or neutral atoms or for both. Therefore, in all cases the number of neutrals returned into the discharge is reduced. Langmuir probe measurements have disclosed that this change in neutral backscatter results in significant changes of the afore-

mentioned critical plasma properties. The changes consist of

1. A plasma potential distribution which inhibits radial ion loss and thereby enhances ion extraction

2. A lower over-all plasma density

3. Less exchange of energy from primary to Maxwellian electrons, resulting in lower electron temperatures.

With low ion optical transmission (i.e., with high neutral backscatter), a central potential ridge extends along the discharge axis. In terms of the discharge model described in Section III-A this can be explained as the result of excessive ionic space charge. Because ions are less mobile than electrons, they accumulate until their space charge fields drive them out at rates for which production and losses are balanced.

With high ion optical transmission the center ridge is decreased and a smaller ridge near the anode becomes prominent. We attribute the decrease in height of the center ridge to the smaller rate of neutral backscatter from the ion optical system and the associated smaller rate of ion generation in the discharge volume. The cause for the anode ridge, which exists in both situations, is not fully understood. It is possible that it results from the finite electron cyclotron diameter. If an electron reaches within one cyclotron diameter of the anode, it is quickly intercepted. Therefore, a layer one cyclotron diameter thick next to the anode is depleted of electrons and the resulting excess of ions may cause the observed potential hump.

In any case, the two different potential distributions lead to significantly different ion flow patterns. With a predominant anode ridge, ions are confined radially and must leave in both axial directions. With a high center ridge, however, many ions will reach the anode and lose their charge. These neutrals rebound into the discharge and eventually become ionized again. Neutrals which rebound from areas adjacent to the extraction screen have a high probability for escape through the screen. As is pointed out in Section III-A, the plasma density must be made excessively high to prevent their loss. It is not unexpected, therefore, that in the case of high ion optical transmission propellant utilization comparable to that for low transmission can be obtained with plasma densities which are lower by a factor of 2 to 5. It is obvious that this should make itself felt in reduced discharge losses. The saving should result from both a decrease in the number of required ionizations and a decrease in the transfer of primary electron energy to Maxwellian electrons through Coulomb collisions.

Finally, the absence of rebounding neutrals also can be held responible for a smaller difference in performance between uniform and divergent magnetic configurations if high transmission optics are used. Without these neutrals, less ionization takes place at the larger radii near the screen. Consequently, even with a diverging magnetic field configuration the plasma density should drop off radially (as confirmed by Langmuir probe data). Accordingly, similar performance may be expected for uniform and diverging field configurations.

6. Diagnostics

Langmuir probe measurements were made in the thruster configurations whose performance mappings are shown in Fig. 23. The results of these probe measurements are shown as three-dimensional plots in Figs. 24 through 29, where the vertical coordinate is used for plasma density, normalized plasma potential, or the Maxwellian electron temperature. The probe measurement technique is described in Section II-B. The probe measurements made in the thruster chamber using type A optics were performed quite early in the contract, with a point-by-point data collection technique. Since considerable time elapsed during acquisition of the individual probe curves, the data are more scattered than those collected more recently with a fast, semiautomatic data recording technique. The curves in Figs. 24 through 26, which link the data points, have therefore been smoothed in an effort to produce what may be considered to be "most plausible" distributions. Figures 24 through 26 compare plasma density distribution, normalized plasma potential, and Maxwellian electron temperature, for magnetic configurations 16A and 16D when operated with type A optics. It is apparent from Fig. 24 that the divergent magnetic configuration eliminates the central "peak" in the spatial plasma density distribution, increases the plasma density near the screen, and thereby renders the plasma density more uniform spatially. Figure 25 shows that there is no essential difference between the plasma potential distributions for the two magnetic configurations, that the plasma potential is essentially constant throughout the discharge chamber, and that it is appreciably above anode potential with slight gradients in the directions of the extraction screen and the anode. It is somewhat inaccurate to describe the plots of Fig. 26 as "Maxwellian" electron temperature. Langmuir probe characteristics indicate that there are no distinct primary and Maxwellian electronic components in the central regions of the discharge chamber. The distributions here can at best be called "near"-Maxwellian. Consequently, the temperatures which are shown in Fig. 26 and which have been derived from slopes "best fitting" the semilogarithmic probe curves must be taken with some caution. The main purpose here was to show that average electron energy is somewhat lower in a divergent magnetic configuration and that the interaction between primary and ionization product electrons is decreased in the divergent configuration. Figures 27 through 29 compare the same quantities for configuration 16A and 16D with type B optics. It is immediately obvious that all three plasma properties are significantly different from those of the thruster operated with type A optics, whereas the differences seen between configuration 16A and 16D using the type B optics are relatively insignificant. Figure 27 shows that in both magnetic configurations the plasma density has a diffusion dominated distribution and is lower in density by at least a factor of two than in the same configuration operated with the type A optics. Figure 28 shows, relatively little difference between magnetic configurations, but an essential difference in potential distribution from that observed with the type A optics. The plasma potential with the type B optics is seen to be lower in general and to fall even below anode potential near the screen. In addition, the potential rises near the anode to form a potential barrier for ions. Consequently, the plasma potential distribution with type B optics should be far superior in trapping ions and

establishing an ion drift toward the extraction screen. Finally, Fig. 29 shows the spatial energy distribution of the Maxwellian plasma electrons with type B optics. It can be seen that the temperature distribution is slightly different for the two magnetic configurations, which probably accounts for the small difference in observed thruster performance. Since the Maxwellian electrons must gain energy through collision with primaries, the distribution of temperatures seen in Fig. 29 points out the regions of the discharge chamber in which primary and Maxwellian interact most strongly. In the divergent magnetic configuration, the primary electrons are distributed in a relatively large volume in the vicinity of the screen and the Maxwellian electron temperature is seen to be relatively more uniform and lower than in the uniform magnetic configuration. In the latter configuration the primaries are confined more to the axis. The Maxwellian temperatures are therefore highest on the discharge axis and decrease in the radial direction.

E. HOLLOW CATHODE THRUSTER

The following investigations were conducted with the dual objectives of improving the understanding of the thruster discharge and optimizing performance:

1. a study of hollow cathode discharge operation
2. a study of the interface between hollow cathode and discharge plasma
3. a parametric and diagnostic study of the discharge plasma.

Except for the hollow cathode diode tests, all studies to be reported here were conducted with an experimental thruster of the type used in the oxide cathode thruster studies. This thruster (No. 2) was designed to facilitate variations of magnetic field strength and shape, discharge chamber length, and location of propellant introduction. In addition, provision was made to permit insertion of Langmuir probes into the discharge region and to monitor separately currents collected by the screen electrode, cathode housing, and several anode segments.

1. Hollow Cathode Diode Experiments

At the beginning of this contract only limited knowledge was available about the operation of hollow cathodes in thruster discharges. It was considered likely that in 15 cm and larger diameter thrusters, where the discharge current exceeds about 1A, hollow cathodes operate in the "spot" mode. This conclusion was based on diode experiments in which an abrupt transition occurs from "plume" to "spot" mode when the current exceeds about 0.8 A.

A separate experiment was set up in a small vacuum facility with the dual objectives of better understanding the hollow cathode discharge plasma and determining the conditions under which cathode tip sputtering would take place. The role of the keeper in reducing sputtering was considered of particular interest.

The experimental arrangement is shown schematically in Fig. 30. The anode and Langmuir probe were independently movable. Their position was monitored with micrometer heads; these precision gauges were incorporated because it was anticipated that significant changes of the plasma properties might occur over very short distances in the narrowly confined space between cathode tip and keeper electrodes.

The sputtering measurements were deemed inconclusive after it was found that in spot mode operation in the thruster, only ions from the thruster discharge have sufficient energy to cause sputter erosion. Therefore, pertinent sputtering results were not obtained in the absence of a thruster discharge; the data collected on sputtering appear in the data book.

Considerably more meaningful results were obtained from Langmuir probe measurements. They revealed that an invisible plasma cone extends between cathode tip and anode in the spot mode. The plasma density decreases monotonically with distance from the cathode, the electron temperature is constant (about 0.8 eV), and the plasma potential is level at about 12 V above cathode potential. (Very similar properties are observed in thruster operation. In particular, the plasma potential is level between cathode tip and baffle and is about 13 to 14 V above cathode potential.)

These diode measurements were conducted only within a short distance of the cathode, since they were planned to give information about the effect of the keeper. It was found that the keeper does not significantly influence the hollow cathode plasma. Data obtained with the keeper removed match those with keeper in place.

Several conclusions may be drawn from these observations:

1. Electrons injected into the discharge plasma from the hollow cathode region possess a kinetic energy which is smaller by about 12 to 13 eV than the energy equivalent of the full discharge potential. Accordingly, primary electrons in hollow cathode thrusters are considerably less energetic than those in oxide cathode thrusters.

2. A fraction of input power, approximately equal to the product of discharge current and hollow cathode plasma potential, is consumed by the hollow cathode discharge and serves to heat the hollow cathode.

3. Ions from the hollow cathode plasma impact on the hollow cathode body with kinetic energies on the order of 13 to 14 eV, which is below the minimum energy for sputter erosion by mercury ions. Therefore, ions from the thruster discharge plasma must cause cathode tip sputtering.

2. Plasma Interface Study

The interface between discharge and hollow cathode plasmas was studied with experimental thruster No. 2 in the 5 ft vacuum facility. A parametric investigation of various baffle and cathode housing configurations was conducted initially. Langmuir probe measurements revealed the existence of two separate plasma inside and outside the cathode housing,

and magnetic field tracing disclosed a magnetic barrier at the interface. It thus became clear that the baffle and cathode housing, which separate hollow cathode and discharge plasmas, must be designed so that the impedance for electron outflow is sufficiently high to prevent "flooding" of the discharge chamber by primary electrons. Measurements presented in Fig. 31 show how the electron current increases and the discharge voltage decreases while the baffle is moved in a direction where it provides a lower impedance to electron flow. Figure 32 shows the dependence of thruster performance on baffle position and makes clear that in SERT-II type configurations with a magnetic housing and nonmagnetic baffle the impedance results from a combination of geometrical and magnetic obstruction.

It is useful to compare these findings with the results obtained earlier at NASA LeRC with SERT-II type configurations. We believe that the data of R. T. Bechtel, G. A. Csiky, and D. C. Byers[3] on baffle size support our contention of a changing impedance for electron passage into the discharge. These authors found a systematic increase in the ratio between discharge voltage and discharge current as the baffle was increased. At the same time, thruster performance improved. Indeed, Bechtel, et al., obtained the best performance with a baffle which is larger than that of the SERT-II. The latter was used in nearly all studies under this contract. This explains why our experimental thruster, with a magnetic field configuration very similar to that of the SERT-II thruster, could equal the performance of the SERT-II; however, it fell short of the performance attained more recently by Bechtel[3] with a "modified" SERT-II configuration (see Fig. 48, which will be discussed later).

The results of the plasma interface studies can be summarized as follows:

1. A plasma sheath approximately 1.5 cm thick extends across the openings between baffle and cathode housing. The potential within the sheath rises from about 13 V on the inside to discharge plasma potential on the outside.

2. If baffle and cathode housing are both nonmagnetic, the best thruster performance is obtained when the baffle is located far back in the cathode housing.

3. If a nonmagnetic baffle and a magnetic cathode housing are used, best performance is obtained with the baffle located across the open end of the housing.

4. As the baffle is moved away from the optimum position, the discharge "impedance" (ratio of discharge voltage to discharge current) decreases.

We believe that the "impedance" provided by baffle and magnetic field serves to stabilize electron flow through the discharge. In Section III-A we show that diffusion of electrons across the discharge plasma to the anode is governed by Coulomb collisions, where the diffusion rates are inversely proportional to the square root of the electron energy.

Accordingly, as the discharge potential is decreased and the electron energy drops, the discharge current tends to rise. Hence, the discharge plasma has an impedance characteristic with negative slope. With a practically infinite supply of electrons from the hollow cathode, the discharge therefore tends to draw excessive currents unless a stabilizing positive impedance is introduced. The obstruction provided by the baffle serves this purpose.

In the case of a nonmagnetic baffle with nonmagnetic housing, hollow cathode electrons find it increasingly difficult to pass into the discharge plasmas as the baffle is moved back into the housing. A decrease in transmitted electron current leads to an increase in discharge potential and more energetic electrons. These ionize more efficiently, and performance improves.

In the case of a nonmagnetic baffle with magnetic housing, performance is best with the baffle mounted across the open end of the housing; this suggests that in this position the electrons are obstructed most severely. Magnetic field mappings (see Fig. 36, for example) have disclosed that electrons must cross magnetic field lines in order to reach the discharge plasma.

3. Discharge Plasma Studies

All investigations of hollow cathode thruster discharges were conducted with experimental thruster No. 2 in either a 5 or a 9 ft vacuum facility, and all measurements were obtained while an ion beam was drawn. Performance data were taken only after the neutral flow had been stabilized for several hours.

Because experiments with the oxide cathode thruster had already provided the necessary information about a number of parameters, including length of the discharge chamber, cathode position, and location of propellant introduction, much of the hollow cathode thruster effort was devoted to

1. a parametric magnetic field study
2. a diagnostic study of the discharge plasmas obtained with uniform and divergent magnetic fields and with high ion optical transmission.

Basically, this parametric study involved three steps. Initially, the magnetic fields were shaped using solenoids only. Cathode pole pieces were then added. Finally, screen pole pieces were also included. During the magnetic field study the ion optical system was upgraded from 48% open area (type A optics) to 71% open area (type B optics) for better over-all performance. Only later was the associated fundamental change in discharge properties realized. Accordingly, the results of the early phases, when low transmission optics were used, are not fully consistent with some of the later findings.

We present the results by proceeding from a uniform magnetic field configuration toward increasingly shaped field geometries. First, as the field lines begin to diverge in the direction of the screen, performance improves (see Fig. 33). The same result was obtained with oxide cathode thrusters and, undoubtedly for the same reasons, the distribution in plasma density and electron temperature became more uniform. Performance improves still further as a cathode pole piece is added. We believe that this improvement results primarily from the previously described increase in baffle impedance; with a magnetic cathode housing, electrons find it harder to enter the discharge, which results in a higher discharge potential and therefore in better performance. Third, addition of a screen pole piece to render the field distribution still more diverging in the experimental thruster does not improve performance (see Fig. 37). In fact, too much spread results in deterioration of the performance. This results because the discharge current increases with increasing field spread and the discharge voltage becomes lower, indicating that electrons can now reach the anode too easily.

The change from 48% to 71% optical open area results in a significant improvement in performance, as can be seen in Fig. 41. Langmuir probe measurements of the configuration shown in Fig. 43 revealed the same potential ridge (see Fig. 44) near the anode as is found in oxide cathode thrusters with high transmission optics. Therefore, we believe that the explanation for the performance improvement, given in Section II-D, applies to the present case as well. Furthermore, with high transmission optics the difference in performance between uniform and divergent magnetic field configurations becomes relatively small.

An interesting observation can be made at this point concerning the magnetic configuration. Note that configuration 42 employs a screen pole piece, but optimum performance results when the magnet windings are operated to produce a relatively uniform magnetic configuration. According to the oxide cathode thruster studies, this is plausible because configuration 42 employs "standard reverse" propellant injection, an injection mode which is suited only for uniform magnetic configurations.

When these results are compared with Bechtel's magnetic field studies,[2] it must be considered that his effort was devoted to optimization attempts with a permanent magnet thruster, while ours used electromagnets and pole pieces. With this in mind, our findings correlate well with those of Bechtel. His parameter study of the screen collar length shows a decrease in performance as the length exceeds an optimum value. We believe that this is the result of an excessively diverging field where field lines from the cathode pole piece pass through the anode to the collar and cause direct interception of primary electrons by the anode. If the collar is shorter than optimum, it is assumed that virtual poles of the permanent magnets are uncovered and strong local fields again attract primary electrons to the anode. The absence of any significant performance change with variations of the screen pole piece in our tests is not unexpected because the pole piece is located in front of the anode and serves as a shield (at cathode potential).

The following conclusions may be derived from these results:

1. A high transmission ion optical system is most important for good thruster performance. Use of such a system results in changes in the discharge properties and leads to a potential distribution which confines the

ions radially. This prevents power losses associated with unnecessary reionization of the propellant gas.

2. With a high transmission ion optical system the radial distributions of plasma density and electron temperature are very similar for uniform and divergent magnetic fields. As a result, performance is very similar in both cases.

F. RADIAL FIELD THRUSTER

1. Configuration

In the final phases of the contract several experiments were conducted in a discharge chamber with a predominantly radial magnetic field configuration. This geometry was chosen with the intention of replacing the diffusion controlled, centrally peaked density profile with a distribution rendered radially uniform by unobstructed motion of electrons along radial field lines.

The configuration of this "radial field thruster" is shown in Fig. 45. It can be seen that the desired magnetic field shape is obtained with a soft iron center post. This post also serves as a cathode housing and baffle for the hollow cathode. The outer chamber cylinder, formerly the anode, is now kept at cathode potential to provide the necessary confinement for the electrons in a Penning type discharge. The anode is located in the rear of the chamber and consists of a flat disk. Propellant is introduced in the same locations as in the other discharge chamber studies.

2. Test Results

In operation the behavior of this thruster was similar to that of other hollow cathode thrusters, except that it produced a very flat ion beam profile. The magnetic field configuration initially had the shape shown in Fig. 45, and performance was so poor that no performance mapping was undertaken. A change of the magnetic field to the configuration shown in Fig. 46 reduced the discharge losses from above 400 eV/ion to 230 eV/ion at about 90% mass utilization (see Fig. 47). The reason for this improvement is not fully understood. In the first configuration, injection of propellant occurred into a plasma region where many primary electrons are present; this may have led to a high center potential, similar to that in conventional thrusters with low transmission ion optical systems. In the second configuration, neutrals were injected into a region where primary electrons should be rare. The associated distributed ion production conceivably may have lowered the center potential sufficiently to provide ion trapping as in conventional thrusters with high transmission optics. Unfortunately, no time remained under the contract for the necessary diagnostic measurements.

Prior to the duration test, thruster performance curves were obtained for two levels of propellant flow. Figure 47 shows that a change

from 334 mA to 426 mA has little effect upon performance.

Even though little time was available to test the radial field configuration, the results obtained are very encouraging. The performance is slightly better than that of any known 15 cm hollow cathode thruster (see Fig.48); it is more important that the flatness of the ion beam profile is significantly superior to that of any other thruster (see Fig. 49). This latter improvement may be assessed quantitatively in terms of the ratio

$$\epsilon = \frac{2\pi \int_0^{r_b} j\, r\, dr}{\pi r_b^2\, j_{max}}$$

where j is the current density at radius r, j_{max} is the current density maximum (usually in the center), and r_b is the ion beam radius at the thruster. We label ϵ "perveance utilization" and express it in per cent. From the normalized beam profiles in Fig. 50 we find that the perveance utilization of the SERT-II thruster is about 38%, while the radial field thruster yields 67%. These values are somewhat inaccurate because the beam profile was measured slightly downstream of the ion optical system. In essence, with identical beam voltages and with the same life expectancy, the radial field thruster can deliver about twice as much thrust as a SERT-II thruster of the same size.

The radial field thruster was chosen as the "final configuration" under the contract and a continuous 24 hour test was performed. The details of this thruster configuration, including the location of propellant introduction are given in the prints which accompany this report. Throughout the test the thruster operated smoothly and stably. Table XVIII gives data recorded hourly; Table XIX contains 4 hour averages of these data. Inspection of the thruster after the test indicated no unusual wear. In particular, the hollow cathode sustained practically no sputter damage.

Based on the results given above, the following conclusion can be drawn: A significant improvement in ion beam uniformity can be achieved with a radial field configuration. It is believed (but has not yet been confirmed experimentally) that with a radial B-field the radial plasma density is quite uniform since the electrons can move freely in and out along field lines. Consequently, the ion beam profile should be flat, as it is indeed found to be. Additional advantages of the radial field configuration are a shorter discharge chamber and the existence of a center post, which serves to provide the radial magnetic field and which can be used as a support for the ion optical system and for a centrally located neutralizer.

III. THEORETICAL PROGRAM

A. BASIC PROPERTIES OF THE THRUSTER DISCHARGE

1. Discharge Regime

Kaufman thrusters utilize a Penning-type discharge to ionize the propellant gas. This discharge mode can be established at low pressures where the neutral atom mean free path exceeds the discharge dimensions and where ordinary glow discharges fail to operate. The crucial features of the Penning discharge is a magnetic confinement field. The lines of force pass into and out of the discharge across electrodes which are at cathode potential, so that the discharge electrons are trapped. They remain in the discharge long enough to undergo one or more ionizing collisions; consequently, a discharge can be sustained.

In the conventional Kaufman thruster configuration, electron confinement is provided by a discharge chamber with a cylindrical anode, axial magnetic field, and two flat endplates at cathode potential (one of the latter serves as the ion extraction screen). In order that electrons injected from an axially located thermionic source will remain sufficiently well trapped, the magnetic field strength must be so large that the electron cyclotron diameter is small compared with the discharge diameter. It has been found empirically that for good performance the magnetic field of a 15 cm thruster must be on the order of 20 gauss. The cyclotron diameters of the more energetic electrons are thus about 1.5 cm.

Even well trapped electrons eventually have to leave the discharge. Collisions with other particles can lead to cross-field drifts (in the presence of an E-field) and diffusion (under a density gradient) in the direction of the anode. The velocity associated with this cross-field transport depends upon the type and frequency of the prevailing collision mechanism. Using empirical information concerning the discharge, we will now assess the relative importance of different collision processes. In addition, we will determine whether drift or diffusion carries the electrons to the anode. Based on this we will postulate a qualitative discharge model.

2. Empirical Discharge Properties

First, we establish the approximate magnitudes of the neutral and charged particle densities in the discharge and also of the electron temperatures. An estimate of the neutral density N may be obtained under use of the molecular flow expression

$$n = 1/4\ \nu_n N$$

where ν_n is the thermal velocity and n is the propellant influx per unit area and time. A typical 15 cm thruster operates at a propellant flow rate

equivalent to about 0.3 A; hence, n is about 10^{16} particles/cm^2 sec. Furthermore, if the propellant is mercury and if the gas temperature is 250°C, the thermal gas velocity becomes about 3×10^4 cm/sec. The upstream neutral density should therefore be on the order of 1.4×10^{12} particles/cm^3. Since most atoms become ionized on their way to the extraction screen, the average neutral density should be less than half the above number, or about 7×10^{11} particles/cm^3 (equivalent to a pressure of 3×10^{-5} Torr).

The electron density is known roughly from Langmuir probe measurements in the discharge (see Section II-0 and Refs. 10 and 11). In the center, the density has been found to reach values on the order of 6×10^{11} particles/cm^3. Near the anode the density decreases to about 2×10^{11} particles/cm^3. Langmuir probe data have also been used to determine the electron temperature (or average energy). The latter is found to decrease from about 15 eV in the center to the order of 3 eV near the anode. These data pertain to conventional thrusters with ion optics which give about 50% transmission.

3. Collision Processes

With the above information we can derive approximate values for mean free paths and collision frequencies of the various collision processes. For collisions which involve neutral particles we take the literature values. For collisions between charged particles we use an expression for Coulomb collisions, given by

$$\nu_c = 2\pi \ell n \Lambda \epsilon^3 \left(\frac{2}{m}\right)^{1/2} (eV)^{3/2} \rho$$

where ν_c is the collision frequency, $\ell n \Lambda$ is a collision parameter (≈ 15), eV is the average particle energy, and ρ is the plasma density. Numerical values are given in Table XX; the numbers pertain to the first-named partner in each collision pair. The collision data of Table XX lead to the following conclusions:

1. Neutrals rarely collide among each other, and their flow is free-molecular. This fact was used in the earlier estimate of the neutral density.

2. Ions rarely collide with neutrals and, except in the center, rarely with other ions. Therefore, they leave the discharge on ballistic trajectories.

3. Electrons collide more frequently with ions than with neutrals. The transport across field lines therefore is determined by the plasma density and not by the neutral density.

4. Electron-electron collisions in which energy is exchanged are as frequent as electron-ion collisions which lead to cross-field transport. Therefore, high energy electrons which (because of their large cyclotron diameter) require few collisions to reach the anode are not very effectively thermalized. Low energy electrons, however, under-

go many collisions among each other, however, and thus form a Maxwellian distribution.

In addition to these collision properties we must consider the question of drift versus diffusion. Langmuir probe studies have disclosed that with a uniform B-field the plasma potential within the entire discharge volume is above anode potential and that it slopes downward to the anode with a gradient which increases with radius (see also Ref. 11). Consequently, the E-fields tend to drive the electrons toward the center rather than out to the anode. It must be concluded, therefore, that diffusion under a density gradient is the overriding mechanism for delivering electrons to the anode. It should be added that no evidence has been found to date for a third possibility,anomalous diffusion in the presence of instabilities.

4. Qualitative Discharge Model

If combined, the above described properties lead to the following qualitative discharge model: Electrons injected into the discharge center with an energy equivalent to plasma potential constitute a primary component. These electrons ionize as they diffuse out. Because the electron-electron collision cross section increases with decreasing particle energy, primarily those electrons which have lost energy in ionizing collisions undergo a thermalization process with other low energy electrons; this gives rise to a Maxwellian electron component. Both the primary and Maxwellian groups accumulate in the discharge until their radial density gradients have become sufficiently large to produce diffusion rates equal to the injection and production rates.

The newly born ions also accumulate until their removal rates become equal to the production rates. The observation of plasma potentials above anode potential implies that the ions tend to accumulate to a density exceeding that of the electrons, except that the slightest excess in positive space charge raises the plasma potential. This helps to remove ions in two ways: (1) they can now land on the anode, and (2) E-fields associated with the potential rise can accelerate the ions in the direction of the walls.

Evidently, few of the ions will speed directly toward the extraction screen. Most will impact on other electrodes where they lose their charge. They rebound into the plasma and eventually become reionized. Simply on the basis of the ratio of total discharge chamber surface to open area in the extraction screen, it can be estimated that the average ion undergoes some eight ionizations before it ejects through the screen. It is clear that each of these ionizations is obtained at the cost of energy.

While repeated ionizations are one cause for inefficiency, the nonuniformity of the plasma also is a contributing factor. The steep decrease with radius of electron density as well as electron energy leads to the escape of many neutrals through the peripheral screen areas. In order to reduce this loss to a tolerable level, the electron density near the anode must be raised. Unfortunately, any increase there also results in an increase in the central density gradients and leads to higher diffusion

currents which ultimately lower the efficiency of the ion generation process.

For these reasons a configuration in which the plasma is distributed more uniformly in density and electron energy throughout a layer across the ion extraction screen is advantageous. The diverging magnetic field configuration of SERT-II type thrusters and the radial magnetic field configuration represent steps in this direction.

B. DISCHARGE CHAMBER THEORY

1. Model

In this section we will present a theoretical analysis of the discharge regime in Kaufman thrusters. We confine the discussion to the following straightforward configuration:

1. The discharge chamber consists of a cylindrical anode and of two flat cathode end plates.

2. Propellant gas is injected through uniformly distributed openings in the "upstream" endplate.

3. Electrons are injected from a circular thermionic cathode located in the center of the upstream endplate.

4. Ions are extracted through uniformly distributed holes in the "downstream" endplate.

5. A uniform magnetic field extends axially through the discharge chamber.

2. Assumptions

The analysis is made under the following physical assumptions:

1. Electrons are in thermal equilibrium locally, and therefore possess a Maxwellian-Boltzmann distribution. The justification for this assumption will be given below.

2. Electrons are transported across magnetic field lines to the anode by cross-field diffusion (under a density gradient). Cross-field drift (under a potential gradient) can be ruled out since the potential gradients actually observed are small and usually so directed that they tend to drive the electrons inward.

3. Coulomb collisions between electrons and ions determine the rate of electron diffusion. Collisions between electrons and propellant atoms are rare and they contribute little to diffusion.

4. Ions accumulate in the discharge volume until the center potential has risen to the point where the associated E-fields

drive the ions out as fast as they are created. This implies that ions are free to move along ballistic trajectories. This assumption seems justified because collisions are sufficiently frequent to interrupt the flight paths (see Table XX) only near the discharge axis.

5. Propellant atoms are uniformly distributed across all radii. This assumption restricts the validity of the analysis to low and medium values of propellant utilization, as will be seen below.

6. Electron and ion dynamics are treated as if the discharge were infinitely long. This is considered well justified for electrons because they are fully reflected at both end plates. The situation is less clear with respect to the ions. Basically, the high mobility of electrons along lines of force of the B-field tends to prevent axial potential gradients and the ion outflow should be governed strictly by radial potential gradients, as in an infinitely long configuration. However, the two end plates at cathode potential perturb the plasma over distances which considerably exceed the width of the plasma sheath. In accordance with the laws governing the formation of cathode sheaths there must be "pre-sheath" regions if the ion temperature falls below that of the electrons within the plasma. Across these regions the potential gradually decreases by about $1/2\ kT_e/e$ toward cathode potential. With average electron energies on the order of 3 to 10 eV in the disharge, this axial potential drop may amount to several volts. Because the details of the pre-sheath regions are difficult to assess, we will simply ignore its effects upon radial ion flow.

7. A cylindrical center section of the discharge, carved out by the trajectories of the newly injected electrons, is treated as uniform in density and electron temperature. Because this section represents a relatively small portion of the discharge volume, the resulting error may be expected to be comparatively small.

3. Analysis

In accordance with the above described assumptions we use the following expression for cross-field diffusion as the equation of motion for the electrons

$$\nu_{\perp} = D_{\perp} \frac{\partial \rho}{\partial r} \rho^{-1} \qquad (3)$$

where $\nu_{\perp}$ is the radial electron velocity, $D_{\perp}$ is the cross-field diffusion coefficient and ρ is the electronic charge density.

The diffusion coefficient can be expressed as (in cgs units)

$$D_{\perp} = \frac{2}{3} \frac{m}{e} \left(\frac{c}{B}\right)^2 \nu_c V \tag{4}$$

where e and m are electron charge and mass, B is the magnetic field strength, c is the velocity of light, ν_c is the collision frequency, and eV is the kinetic electron energy.

For the collision frequency ν_c we use an expression for Coulomb collisions which includes multiple small angle scatterings

$$\nu_c = 2\pi \ell n\Lambda \; e^3 \left(\frac{2}{m}\right)^{1/2} (eV)^{-3/2} \rho \tag{5}$$

where $\ell n\Lambda$ is a collision parameter (the numerical value of which is taken to be 15). Introduction of (4) and (5) into (3) yields

$$\nu_{\perp} = -\frac{4\pi}{3} \ell n\Lambda \; (2m)^{1/2} e \left(\frac{c}{B}\right)^2 (eV)^{-1/2} \frac{\partial \rho}{\partial r}. \tag{6}$$

Equation (6) must be averaged over all electron energies. If we assume that the plasma electrons possess a Maxwellian energy distribution, electrons with energy eV contribute to the over all density the fraction

$$\frac{d\rho}{\rho} = \left(\frac{4}{\pi}\right)^{1/2} \left(\frac{eV}{kT}\right)^{1/2} \exp\left(-\frac{eV}{kT}\right) d\left(\frac{eV}{kT}\right) \tag{7}$$

where 3/2 kT is the average electron energy. The average drift velocity $v_{\perp}$ can be obtained with the help of

$$\overline{v_{\perp}} = \frac{1}{\rho} \int v_{\perp} \, d\rho. \tag{8}$$

If (6) and (7) are introduced into (8) integration yields

$$\overline{v_{\perp}} = \frac{8}{3} (2\pi m)^{1/2} \ell n\Lambda \; e \left(\frac{c}{B}\right)^2 (kT)^{-1/2} \frac{\partial \rho}{\partial r} \tag{9}$$

or

$$\overline{v_{\perp}} = C_o B^{-2} (kT)^{-1/2} \frac{\partial \rho}{\partial r} \tag{10}$$

where $C_o = 1.3$ cgs if $\ell n\Lambda$ is taken to be 15.

Prior to using (10) in the analysis we intend to establish the validity of the assumption of a Maxwellian distribution. According to Langmuir probe measurements made under this contract, the actual distribution in

thruster discharges with uniform B-field can be interpreted as a combination of typically 10% monoenergetic primary electrons and 90% thermalized electrons with a near-Maxwellian distribution. The temperature of the latter component is about 15 eV in the discharge center and 3 eV near the edge. In Table XXI we compare the diffusion coefficients and average ionization frequencies $\bar{\nu}_i$ of a pure Maxwellian distribution with that of a 1:9 mixture of primary and Maxwellian electrons. For the ionization frequencies of monoenergetic electrons we resort to literature values 15; for that of a Maxwellian distribution we use rates derived below (see Fig. 51).

According to Table XXI the two types of distributions yield values having relatively small differences, and the assumption of a pure Maxwellian distribution in the analysis appears well justified.

In addition to the above derived equation of motion (eq. (10)), we require a continuity equation. The radial flow of electrons must be subject to the conditions

$$\operatorname{div} j = \bar{\nu}_i \rho \tag{11}$$

where j is the radial electron current density and $\bar{\nu}_i$ is the average ionization frequency. Equation (11) can be rewritten as

$$\rho \frac{\partial \bar{v}_\perp}{\partial r} + \bar{v}_\perp \frac{\partial \rho}{\partial r} + \rho \frac{\bar{v}_\perp}{r} = \bar{\nu}_i \rho . \tag{12}$$

If (10) is differentiated with respect to r and if the expressions for $\bar{v}_\perp$ and $\partial \bar{v}_\perp / \partial r$ are introduced into (12), a differential equation for the charge density is obtained

$$\frac{\partial^2 \rho}{\partial r^2} + \frac{1}{r} \frac{\partial \rho}{\partial r} + \frac{1}{\rho} \left(\frac{\partial \rho}{\partial r}\right)^2 - \frac{1}{2} (kT)^{-1} \frac{\partial (kT)}{\partial r} \frac{\partial \rho}{\partial r} + \frac{B^2}{C_o} (kT)^{1/2} \bar{\nu}_i = 0 \tag{13}$$

Because (13) contains not only ρ but also the unknown function (kT) of r, a second equation must be provided. The following energy conservation condition can serve this purpose:

$$\frac{d(kT)}{dt} = \frac{\partial (kT)}{\partial t} + v^* \frac{\partial (kT)}{\partial r} . \tag{14}$$

First, since a steady state solution is being sought, the term $\partial / \partial r$ must vanish. Second, the average energy transport velocity v^* is determined by

$$v^* \frac{\partial (kT)}{\partial r} = \frac{1}{\rho} \int v \frac{\partial (kT)}{\partial r} d\rho = \frac{1}{\rho} \frac{\partial (kT)}{\partial r} \int v \, d\rho = \bar{v} \frac{\partial (kT)}{\partial r};$$

therefore, it is identical with the average diffusion velocity $\bar{v}$. Third, the term d(kT)/dt represents the average rate of energy loss by excitation and ionization in a Maxwellian distribution with temperature T. This loss rate and the average ionization frequency $\bar{\nu}_i$ in (13) are functions of the electron temperature

$$\frac{d(kT)}{dt} = - g(kT), \qquad \bar{\nu}_i = k(kT).$$

Both functions can be considered known because they can be derived from available collision data. For example, to obtain $\bar{\nu}_i$ one must take the familiar function of the ionization frequency ν_i versus electron energy eV (see Fig. 51) and compute $\nu_i \, d\rho$, where $d\rho$ is the number of electrons with energy eV in a Maxwellian distribution of temperature kT (see (7)). Integration over all energies and division by the total charge density then yields the average ionization rate at electron temperature T;

$$\bar{\nu}_i = \frac{1}{\rho} \int \nu_i \, d\rho \, .$$

If this expression is evaluated for a number of different temperatures, the functional dependence $\bar{\nu}_i = k(kT)$ can be found. This dependence has been computed for mercury (see Fig. 51). It can be seen that over the range of interest of electron temperatures (from about 3 to 20 eV), $\bar{\nu}_i$ increases linearly with T. Accordingly, the following approximation for $\bar{\nu}_i$ will be used here:

$$\bar{\nu}_i \equiv k(kT) \cong A_o p kT - A_1 p \qquad (15)$$

where

$$A_o = 1.38 \times 10^{20} \text{ erg}^{-1} \text{ sec}^{-1} \text{ Torr}^{-1}$$

$$A_1 = 6 \times 10^{8} \text{ sec}^{-1} \text{ Torr}^{-1}$$

and p is the gas pressure in Torr.

The average energy loss rate can be determined in a similar fashion from

$$\frac{d(kT)}{dt} = - g(kT) = - (eV_i + kT) \frac{1}{\rho} \int \nu_i \, d\rho - \sum_n eV_{ex} \frac{1}{\rho} \int \nu_{ex} \, d\rho$$

where eV_i is the ionization energy and eV_{ex} is the excitation energy associated with a specific level n. It should be noted that the energy loss in an ionization event also includes the energy which must be supplied to a newly born secondary electron so that it will share the average energy kT.

The energy loss rate g(kT) was determined for mercury, based upon losses associated with ionization (10.38 eV), with excitations[14] involving the transitions $1^1S_1 - 2^3P_2$ and $1^1S_1 - 2^1P$ (4.86 and 6.67 eV),

which by far dominate, and including the supply of kT to the newly born electrons. The resultant loss rate curve is shown in Fig. 52. This loss rate function will be approximated by

$$\frac{d(kT)}{dt} \equiv - g(kT) \tilde{=} - A_2 \, p \, (kT)^{3/2} \tag{16}$$

where $A_2 = 8.25 \times 10^{14}$ erg$^{-1/2}$ sec.$^{-1}$ Torr^{-1}.

Using (12) and (16), the energy conservation relation (eq. (14)) can now be expressed as

$$(kT)^{-2} \, d(kT) = \frac{A_2}{C_o} \, p \, B^2 \, \left(\frac{\partial \rho}{\partial r}\right)^{-1} dr, \tag{17}$$

or

$$\frac{1}{kT} - \frac{1}{kT_o} = - \frac{A_2}{C_o} \, p \, B^2 \int \frac{1}{\frac{\partial \rho}{\partial r}} \, dr, \tag{18}$$

or

$$kT = kT_o \left(1 - \frac{A_2}{C_o} \, p \, B^2 \, kT_o \int \frac{1}{\frac{\partial \rho}{\partial r}} \, dr \right)^{-1} . \tag{19}$$

If (15), (17), and (19) are introduced into (13), one obtains

$$\frac{\partial^2 \rho}{\partial r^2} + \frac{1}{r} \frac{\partial \rho}{\partial r} + \frac{1}{\rho} \left(\frac{\partial \rho}{\partial r}\right)^2 - \frac{1}{2} \, kT_o \, C_1 p \, B^2 \left(1 - C_1 \, p \, B^2 \, kT_o \int \frac{1}{\frac{\partial \rho}{\partial r}} \, dr \right)^{-1}$$

$$+ C_2 \, p \, B^2 \, (kT_o)^{3/2} \left(1 - C_1 \, p \, B^2 \, kT_o \int \frac{1}{\frac{\partial \rho}{\partial r}} \, dr \right)^{-3/2}$$

$$- C_3 \, p \, B^2 \, (kT_o)^{1/2} \left(1 - C_1 \, p \, B^2 \, kT_o \int \frac{1}{\frac{\partial \rho}{\partial r}} \, dr \right)^{-1/2} = 0 \tag{20}$$

where

$$C_1 = A_2/C_o$$

$$C_2 = A_o/C_o$$

$$C_3 = A_1/C_o \, .$$

Before we proceed to solve (20) for the radial charge density distribution we intend to derive an expression for the radial potential distribution. In

addition, we must define boundary conditions.

To compute the potential distribution we require Poisson's equation

$$\Delta V = - 4\pi (\rho_i - \rho_e) \tag{21}$$

where ρ_i is the ionic and, $\rho_e \equiv \rho$, the electronic space charge density. Under the assumption that ions flow out radially on ballistic trajectories, their density contribution at each location is given by[16]

$$\rho_i = \frac{1}{r} \int_o^r \frac{\xi\, g(\xi)}{\nu_i(\xi)}\, d\xi \tag{22}$$

where $g(\xi)$ is the ion generation rate per unit volume and time at radius ξ and where $v_i(\xi)$ is the velocity at radius r of an ion born at radius ξ. Since

$$g(\xi) = \rho\, \bar{\nu}_i$$

and since

$$v_i(\xi) = \left[\frac{2}{m_i}(V_r - V_\xi)\right]^{1/2}$$

eq. (22) can be written as

$$\rho_i = \frac{1}{r} \left(\frac{m_i}{2e}\right)^{1/2} \int_o^r \frac{\rho\, \bar{\nu}_i\, \xi\, d\xi}{(V_r - V_\xi)^{1/2}} \,. \tag{23}$$

In principle, a solution for the potential distribution requires that first ρ be obtained from (20), and second ρ and ρ_i (given by (23)) be used to solve equation (21). However, the potential variations are anticipated to be small (on the order of volts) and ΔV should therefore be negligible compared with either $4\pi\rho_i$ or $4\pi\rho_e$. Accordingly, we may approximate (21) by

$$\rho_i \tilde{=} \rho. \tag{24}$$

While this simplifies matters, nevertheless we must first solve (20) for ρ; next we must solve the integro-differential equation (23) where now ρ is substituted for ρ_i. The complicated nature of these equations precludes analytic solutions. Therefore, selected numerical solutions by computer must be sought.

In order to arrive at pertinent solutions, suitable boundary conditions must be specified. For this purpose we consider separately a small cylindrical volume surrounding the discharge axis and having the

radius of the thermionic cathode. We treat this volume summarily and assume that the newly injected electrons are thermalized there completely.

Energy balance within this volume requires that the power delivered by the injected electrons is equal to the sum of power removed by outflowing electrons and power consumed by inelastic collisions. This may be expressed as

$$I_c V_c = (I_c + \pi r_c^2 \ell \rho_c \bar{\nu}_{ic}) \frac{3}{2} \frac{kT_c}{e} + \pi r_c^2 \ell \frac{\rho_c}{e} \frac{d(kT_c)}{dT} \quad (25)$$

where I_c is the electron injection current, V_c is the plasma potential, ρ_c is the plasma density, $\bar{\nu}_{ic}$ is the ionization frequency, and T_c is the electron temperature in the center cylinder. Furthermore, r_c is the cathode radius and ℓ is the length of the discharge chamber.

If expressions (15) and (16) for $\bar{\nu}_{ic}$ and $d(kT_c)/dT$ are introduced into (25), eqs. (20) and (25) can be combined to yield computer solutions for ρ and kT as functions of r. For given discharge potential V_c, discharge current I_c, and neutral pressure ρ, only one set of values kT_c and ρ_c results in a radial density distribution which goes to zero at anode radius r_a. By trial and error (with the help of the computer) this solution can be singled out.

The potential distribution also requires separate treatment of the center section. If (23) is integrated from r = 0, a singularity in the integral causes computational difficulties. These can be prevented with the help of an analytic solution for V at small r. Conveniently, we can use the same assumption as above: viz., constant density ρ_c and electron temperature T_c for $r \tilde{=} r_c$. We then obtain a parabolic potential distribution which may be expressed as

$$V_r = \frac{m_i}{2e} \bar{\nu}_{ic}^2 r^2 . \quad (26)$$

If we split the integral in (23) into two parts, one extending from 0 to r_c and the other from r_c to r, we can perform the integration over the first part with the help of (26) and the singularity at r = 0 is eliminated. However, a similar problem arises at the upper limit. In order that the integrand will not go to infinity as V_ξ approaches V_r, the integral must be terminated at $(r - \Delta)$. To make up for the difference, an approximate expression for the residual contribution must be added. When these modifications are included, eq. (23) can be written as

$$\rho = \frac{\rho_c}{r\,\bar{\nu}_{ic}} \left\{ \left(\frac{2eV_r}{m_i}\right)^{1/2} - \left[\left(\frac{2eV_r}{m_i}\right) - \bar{\nu}_{ic}^{\,2}\right]^{1/2} \right\}$$

$$+ \frac{1}{r}\left(\frac{m_i}{2e}\right)^{1/2} \int_{r_c}^{r-\Delta} \frac{\rho\,\bar{\nu}_i\,\xi\,d\xi}{(V_r - V_\xi)^{1/2}} + 2\Delta^{1/2}\,\rho_r\,\bar{\nu}_{ir}\left(\frac{m_i}{2e}\right)^{1/2}\left(\frac{\partial V}{\partial r}\right)_r^{-1/2} \qquad (27)$$

where the index "r" stands for the location r. Together with (20), eq. (27) can now be used to yield computer solutions for ρ, kT, and ν as functions of the radius. In the actual computations r_c was taken to be 1.5 cm, r_c = 7.5 cm, and Δ = 0.1 cm (equal to the computing step width). Figure 53 shows representative results. In general, the shape of the distributions for ρ, kT, and V is very similar to that found empirically (see Fig. 54). Even quantitatively, the agreement can be considered satisfactory. Of the three computed distributions, that for V is perhaps least reliable because the axial potential variation in the acceleration of ions was neglected.

The agreement between theory and observation provides confidence that the underlying discharge model is essentially correct. This discharge model has already been used in the interpretation of the behavior of advanced thruster geometries studied under this contract, and has given guidance in the optimization task.

As a final item we would like to determine how restrictive is the earlier assumption of a uniform neutral density across (not along) the discharge. One way to establish this is to relate propellant utilization and mean free path. We assume that after the propellant enters the discharge it becomes gradually ionized on its way to the downstream extraction electrode and the propellant density decreases as

$$N = N_o \exp(-z/\bar{\lambda})$$

where $\bar{\lambda}$ is the average mean free path of gas atoms for ionization and z is the distance along the discharge axis.

To relate N_o to the in and outflux of the propellant gas, we consider first a situation without ionizing plasma, where the neutral outflux must match the influx. The latter can be expressed as

$$I_{in} = \pi\, r_a^2\, \frac{1}{2}\, v_n\, N_o\, \alpha \qquad (29)$$

where r_a is the anode radius, v_n is the thermal gas velocity, and α is the fraction of open area in the extraction electrode.

If a plasma is present, the neutral outflow is reduced to

$$I_{out} \tilde{=} \pi\, r_a^2\, \frac{1}{2}\, v_n\, N_o \exp(-z/\bar{\lambda})\, \alpha \,. \qquad (30)$$

Accordingly, the propellant utilization becomes

$$\eta \equiv \frac{I_{in} - I_{out}}{I_{in}} \simeq 1-\exp(-z/\bar{\lambda}) \qquad (31)$$

This is the relation between $\bar{\lambda}$ and η which we have sought. Table XXII shows numerical values. It can be see that up to above 70% mass utilization the mean free path is either longer than or comparable to the discharge chamber dimensions. Therefore, the neutral density should remain relatively uniform across the discharge up to this level of mass utilization. It should be added that because of the oversimplification in the neutral flow pattern considered in (28) through (31), great accuracy cannot be claimed for the results given in Table XXII. However, the only purpose here is to estimate the range of validity of the theory derived earlier.

In this conjunction it is well to remember that only radial variations of the neutral density affect the discharge model. The theory is insensitive to axial variations. Because the electrons sweep back and forth in the axial direction, only the average of the axial neutral density is significant and the detailed distribution is not important.

C. SCALING LAWS

In the past, most of the optimization effort on Kaufman thrusters has been devoted to thruster configurations of 15 cm diameter. With the present trend toward larger thruster diameters, it would be of considerable interest to have available general scaling rules. We will derive below the appropriate relations used in the discharge model discussed earlier.

According to our model the radial flow of electrons is determined by cross-field diffusion and can be described by the equation

$$v_\perp = C_o (kT)^{-1/2} \left(\frac{c}{B}\right)^2 \frac{\partial \rho}{\partial r}$$

where kT is the average electron energy, B is the magnetic field strength, c is the velocity of light, and $\partial\rho/\partial r$ is the radial density gradient. The radial current density j_e then becomes

$$j_e = C_o (kT)^{-1/2} \left(\frac{c}{B}\right)^2 \frac{\partial \rho}{\partial r} \rho \ .$$

It should be emphasized that the latter relation is not restricted to the assumption of a uniform magnetic field which was used in the theory. Even with arbitrary shaped magnetic fields the cross-field current density at any location is given by the above relation as long as cross-field diffusion governs electron transport to the anode. All indications are that

this is the case in thruster discharges using both uniform and diverging magnetic field configurations.

A second quantity required here is the extracted ion current density j_i. If the thermal ion energy is smaller than that of the electrons, as is the case in thruster discharges, a pre-sheath forms near the extraction surface. The potential drop across the pre-sheath is on the order of $1/2\ kT_e/e$, and ions arrive at the sheath edge with the velocity

$$v_i = \sqrt{\frac{kT_e}{m_i}}$$

The plasma density decreases slightly across the pre-sheath and at the sheath edge amounts to

$$\rho_s = C_1 \rho$$

where ρ is the unperturbed plasma density and C_1 is exp (-0.5) which is approximately 0.6. The ion current density at the sheath edge therefore becomes

$$j_i = C_1\ \rho \sqrt{\frac{kT_e}{m_i}} \quad .$$

A third quantity required is the ionization mean free path for neutrals λ_N. To obtain λ_N we compute first the ionization frequency for the neutrals ν_N which is

$$\nu_N = \overline{\nu}_i \quad \frac{\rho/e}{N}$$

where $\overline{\nu}_i$ is the ionization frequency of the electrons, ρ is the plasma density, and N is the neutral density. The mean free path then becomes

$$\lambda_N = \frac{v_N}{\rho/e\ \overline{\nu}_{io}}$$

where $\overline{\nu}_{io}$ is the electron ionization frequency at unit neutral density and ν_N is the thermal gas velocity.

For the purpose of obtaining scaling laws it should be sufficient to convert the above derived expressions for j_e, j_i, and λ_N into proportionalities and consider the various variables as representative averages (indicated by an asterisk). Along the same lines we replace the derivative $\partial\rho/\partial r$ by ρ^*/r^*. This leads to

$$j_e^* \sim (kT^*)^{-1/2}\ B^*\ r^{*-1}\ \rho^{*2}$$

$$j_i^* \sim \rho^*\ (kT^*)^{1/2}$$

$$\lambda_N \sim \rho^{*-1}\ \overline{\nu}_{io}^{-1}$$

where ν_N was eliminated because, in first order, it should be independent of thruster size and geometry. We need one more relation, expressing the proportionality between the total electron current I_e and radial electron current density j_e^*:

$$I_e \sim r^* \ell^* j_e^* \quad .$$

To obtain specific scaling laws we must impose conditions which assure certain desirable scaling features:

1. The electron temperature cannot be permitted to change with thruster size because single and double ionization energies of the propellant gas provide a relatively narrow usable energy range. We set therefore $kT^* = \text{constant}$.

2. For ion-optical reasons the extracted ion current density should remain constant: $j_i^* = \text{constant}$.

3. The propellant utilization should not change with thruster size. This requires that $\lambda_N^*/\ell^* = \text{constant}$.

4. The energy losses per ejected ion also should be independent of thruster size. Because the total extracted ion current is proportional to r^{*2} (as long as $j^* = \text{constant}$), and because the discharge voltage cannot change (to assure that $kT^* = \text{constant}$) the electron current must vary as $I_e \sim r^{*2}$.

These four conditions in conjunction with the above derived four proportionalities immediately yield the following scaling relations:

$$\begin{aligned} \ell^* &= \text{constant} \\ B^* &\sim r^{*-1} \\ (\rho^* &= \text{constant}) \\ (j_e^* &\sim r^*) \end{aligned}$$

Accordingly, if the discharge plasma length is kept constant and if the magnetic field is decreased by the same ratio by which the thuster diameter is increased, the scaled-up thruster should have over-all properties which equal those of the original version. In particular, the plasma density distribution should remain unchanged. Furthermore, since the electron current density is proportionally increased, the lifetime of the average electron remains unchanged and hence will undergo the same number of ionizing collisions. Therefore, the energetic relationships in the discharge should remain preserved; in particular, the energy losses per ejected ion should not change. Finally, with constant plasma density, constant electron energy and constant length of the plasma, the ionization mean force path and hence the propellant utilization should remain unchanged.

A basic shortcoming of these scaling laws is that they cannot take into account more subtle changes in the discharge properties which may result, for example, from changes in the magnetic field geometry as the thruster length-to-diameter ratio is varied. Indeed, this is the very reason why the earlier evolved physical requirements for good performance are so essential. If these requirements are satisfied the detailed mechanisms of the discharge are likely to change little, and the scaling laws should have validity.

The above scaling rules pertain to the discharge plasma. A separate set of rules applies to the hollow cathode plasma and the interface between hollow cathode plasma and discharge plasma. Because little is known about the discharge mechanism in hollow cathode plasmas, a scaling relation cannot be given at this time. To optimize the hollow cathode configuration (including size and shape of cathode housing and baffle) for a scaled thruster, it would appear best to perform suitable parameter studies.

IV. CONCLUSIONS

The work performed under this contract has led to significant advances in the understanding and performance optimization of Kaufman thruster discharges. In this section we summarize the most significant conclusions and make several recommendations.

Equally efficient thruster operation can be obtained in a number of different thruster geometries. All have in common the following important features:

1. The magnetic field must spread from the cathode to the screen electrode so that primary electrons can reach almost the entire screen surface. This results in a plasma with relatively uniform density and electron temperature distributions. A plasma of this type serves as an effective barrier across the screen electrode against escape of the neutral propellant gas.

2. The anode and all electrodes at cathode potential must be arranged with respect to the magnetic field so that a Penning discharge-type confinement results. In particular, those field lines which guide primary electrons must not intercept or come too close to the anode. As a consequence, all primaries remain trapped sufficiently long to expend their kinetic energy in ionizing, exciting and energy sharing collisions.

3. With a hollow cathode, the outflow of electrons into the discharge region must be limited by geometrical obstructions and magnetic fields to prevent excessive electron flow rates through the discharge. The discharge voltage can then be raised to a level where the ionization efficiency is high.

4. A high ion-optical transmission must be used. With a transmission on the order of 70%, the discharge adopts a particularly favorable potential distribution which confines ions radially. This significantly improves discharge performance.

Thruster chambers built in accordance with these general rules are found to be similarly good in performance. Several hollow cathode thrusters (SERT-II, Hughes - experimental No. 2; J.P.L.-20 cm; and Hughes - radial field thruster) consume on the order of 190 to 230 eV/ion at 85% propellant utilization. Several oxide cathode thrusters (SERT-II, Hughes - experimental No. 1; and the J.P.L. 20 cm thruster) require about 130 to 170 eV/ion at 85% propellant utilization. The difference between hollow cathode and oxide cathode thrusters is well accounted for by the additional power consumed in the hollow cathode plasma, which amounts to about 50 to 70 eV/ion (and which is not completely lost because it heats the cathode).

Although different thrusters may be similar in performance, they still produce significantly different ion beam profiles. Thrusters with a radial magnetic field eject a much flatter ion beam than those with a gradually diverging magnetic field. Under otherwise comparable conditions a radial field thruster thus can be operated at nearly twice the ion beam current and, accordingly, at nearly twice the thrust level.

Several other interesting facts and features have come to light under this contract.

1. According to the discharge theory developed here, scaling of thrusters is governed by the following basic requirements:

   a. the effective plasma length must remain constant
   b. the magnetic field strength must decrease inversely with the scaling factor.

2. Discharge operation at voltages as high as 50 V is desirable in hollow cathode thrusters because primary electrons are injected with about 12 to 13 eV less energy than corresponds to full discharge potential.

3. Operation at high discharge voltages may be safe if the plasma interface between hollow cathode and discharge plasmas is oriented so that ions cannot reach and erode the cathode tip.

V. TABLES OF PERFORMANCE DATA

The tables in this section provide the thruster parameters for the performance mappings and plasma diagnostics shown in this report.

LIST OF TABLES

TABLE I

Critical Dimensions of Ion Extraction Optics

Optic	Number of Holes	Screen			Hexagonal Array Center to Center Hole Space cm	Accelerator		Screen Open Area, %
		Nominal Diameter, cm	Thickness, cm	Hole Diameter, cm		Thickness, cm	Hole Diameter, cm	
Type A	499	15.0	0.160	0.470[a]	0.650	0.160	0.470	47.5
Type B	847	13.9	0.076	0.399	0.450	0.152	0.326	71.0

[a]Screen grid holes with 30° chamber to a depth of 0.160 cm on the upstream.

TABLE II

Thruster Parameters for Performance Mapping of NASA-LeRC SERT II Model Thruster Operated with Spiral and Magazine Type Oxide Cathodes and a Hollow (Discharge) Cathode, shown in Fig. 11

Cathode Heater			Arc Discharge			Ion Beam Performance			
V_K, V	I_K, A	P_K, W	V_D, V	I_D, A	P_D, W	I_{beam}, mA	I_{drain}, mA	η_m, %	eV/Ion
● Spiral Oxide Cathode, Equivalent Neutral Current = 290 mA, Vacuum Chamber Pressure = 3 x 10^{-7} Torr									
3.6	36	130	40	2.4	96	265	0.9	91.6	362
			35	2.35	82.4	255	1.1	88	323
			30	2.35	70.5	245	1.2	84.5	287
			25	1.95	48.7	175	1.4	60.5	278
3.2	33	106	40	1.5	60	240	1.0	83	240
			35	1.5	52.5	221	1.1	82.3	221
			30	1.45	43.5	193	1.3	77.8	193
			25	1.4	35	171	1.5	71.0	171
3.0	30	90	45	1.0	45	228	1.0	78.8	197
			40	1.0	40	220	1.2	76	182
			35	0.95	33.2	205	1.4	71	162
			30	0.92	27.6	190	1.7	65.6	145
■ Magazine Oxide Cathode, Equivalent Neutral Current = 306 mA									
4.2	37	156	49	2.3	113	263	0.7	85.8	430
			45	2.25	101.5	257	0.75	83.8	395
			40	2.3	92	247	0.8	80.6	372
			35	2.4	85.8	235	0.9	76.6	365
			30	2.8	84	210	1.05	68.6	400
3.9	35	136	50	1.25	62.5	229	0.8	74.2	273
			45	1.27	57.2	222	0.8	72.5	258
			40	1.2	51.2	215	0.85	70.2	238
			35	1.37	48	208	0.9	67.8	231
			30	1.5	45	198	0.9	64.6	227
3.5	33	116	50	0.75	37.5	187	1.0	61.1	200
			45	0.75	33.7	182	1.0	59.4	185
			40	0.75	30	175	1.0	57	172
			36	0.75	27	165	1.05	53.9	163
▲ Hollow Cathode, Equivalent Neutral Current = 308 mA, 272 mA through Main Feed System, 36 mA through Hollow Cathode, Cathode Heater = 5.2 V, 8 A, 41.6 W. July (1967)									
12.3	0.42	5.2	32.4	3.2	103.8	270	2.0	87.7	384
13.1	0.43	5.6	32	2.4	76.8	256	2.2	83.2	300
13.6	0.43	5.9	32	2.1	67.2	249	2.3	81	269
14	0.43	6.0	31.8	1.58	50	220	2.4	71.5	227
▼ Hollow Cathode, Equivalent Neutral Current 299 mA, 251 mA through Main Feed System, 48 mA through Hollow Cathode, Cathode Heater 3 V, 7A, 21 W, Recent LeRC Baffle Design									
11	0.2	2.2	37.5	3.15	118	254	0.9	85	465
11.2	0.2	2.2	37.2	2.74	102	254	0.9	85	402
11.4	0.2	2.3	36.3	2.31	84	249	0.9	83.2	338
11.8	0.2	2.4	36.9	2.02	74.5	248	1.0	83	300
12.0	0.2	2.4	37	1.7	62.9	242	1.0	81	260
12.3	0.2	2.5	37.7	1.31	49.4	229	1.1	76.5	216
12.4	0.2	2.5	37.3	1.0	37.3	205	1.3	68.5	182
12.4	0.2	2.5	36.8	0.8	29.4	182	1.4	60.8	164

TABLE III

Thruster Parameters and Langmuir Probe Data for SERT-II Thruster Discharge Properties Shown in Fig. 14

Thruster Parameters

Discharge Voltage	37 V
Discharge Current	1.7 A
Beam Voltage	3 kV
Decelerating Voltage	2 kV
Beam Current	242 mA
Drain Current	1 mA
Neutral Current (equivalent)	299 mA total (48 mA through Hollow Cathode)

2 ft Vacuum Chamber Facility, 4×10^{-7} Torr Pressure,
Z ≡ Axial Distance from the Probe to the Upstream Boundary of the Discharge Chamber
n_{pe} ≡ Density of Primary Electrons with Average Energy ≡ eV_o,
n_{me} ≡ Density of "Maxwellian" Electrons with Equivalent Temperate T_e.
n_p ≡ Total Plasma Density
V_p/V_D ≡ Ratio of Plasma Potential to Anode Voltage

Z, cm	R, cm	V_p/V_D	n_{pe} 10^{10} cm^{-3}	eV_o, eV	n_{me} 10^{10} cm^{-3}	T_e, eV	n_p 10^{10} cm^{-3}
1.8	3	0.99	0.05	21	1.6	3.7	1.6
	4	1.0	0.05	15	1.1	2.3	1.1
	5	1.01	0.02	10	1.0	1.6	1.0
	6	1.03	0.01	6	0.7	0.8	0.7
2.8	3	0.99	0.2	14	2.8	4.4	3.0
	4	1.02	0.04	16	1.8	2.9	1.8
	5	1.03	0.02	10	1.2	1.3	1.2
	6	1.03	0.01	5	0.8	0.8	0.8
3.5	0.5	0.35	—	–	16.1	0.8	16.1
	1.0	0.40	—	–	5.8	1.6	5.8
	1.5	0.90	1.1	21	1.8	2.8	2.9
	2.0	0.98	1.2	22	3.4	3.9	5.6
	2.5	1.01	2.3	29	5.1	6.5	5.4
	3.0	1.03	0.2	27	4.6	5.3	4.8
	4	1.04	0.1	21	2.4	3.5	2.4
	6	1.04	—	–	1.0	0.7	1.0
4.0	0.3	1.06	—	–	9.4	10.5	9.4
	1.0	1.0	0.6	31	8.9	9.4	9.4
	2.0	1.07	0.4	32	9.8	8.0	10.2
	3	1.05	0.2	32	10.7	6.3	10.7
	4	1.03	0.1	22	3.0	3.5	3.0
	5	1.03	0.1	10	1.5	1.3	1.6
	6	1.01	—	–	1.0	0.7	1.0
5.8	1	1.09	4.6	28	10.7	4.7	15.2
	3	1.08	1.6	26	7.3	5.5	8.9
	5	1.05	0.02	17	2.1	2.2	2.1
	7	1.02	—	–	0.1	0.4	0.1
7.8	1	1.08	0.1	34	12.4	8.4	12.5
	3	1.06	0.3	33	8.5	7.9	8.8
	5	1.05	0.1	26	2.3	3.7	2.4
	7	1.04	—	–	0.4	0.4	0.4
9.8	1	1.02	0.8	31	9.6	7.5	10.4
	3	1.01	0.4	30	7.8	7.7	8.2
	5	0.99	0.2	18	2.9	5.9	3.1
	7	1.03	0.1	8	0.6	0.9	0.6
11.8	1	0.97	0.8	28	6.6	7.3	7.4
	3	0.96	0.6	29	6.1	8.2	6.7
	5	0.94	0.7	26	3.5	7.0	4.2
	7	1.11	1.3	23	—	—	1.3
12.7	1	0.92	0.4	25	6.1	7.3	6.5
	3	0.95	0.8	26	5.0	7.0	5.8
	5	0.98	4.2	20	—	—	4.2
	7	1.01	1.8	22	—	—	1.8

TABLE IV

Thruster Parmeters for Data Shown in Fig. 15

O Magnetic configuration of Fig. 16(a)
Magnet current = 2.5 A each coil
Cathode heater voltage = 4.75 V
Cathode heater current = 29 A
Equivalent neutral current = 282 mA

Arc Discharge			Ion Beam Performance					
V_D, V	I_D, A	P_D, W	V_{acc}, kV	V_{dec}, -kV	I_{beam}, mA	I_{drain}, mA	η_m, %	eV/Ion
45	1.45	65.2	4	1	258	0.65	91.5	253
40	1.43	57.2	4	1	242	0.7	85.8	236
35	1.43	50	4	1	226	0.7	80.2	221
30	1.43	42.9	4	1	198	0.8	70.2	216
25	1.25	31.2	4	1	141	0.85	50	221

□ Magnetic configuration of Fig. 16(b)
Magnet coil currents = 6, 6, 6, 3, 3, 2, 2, 2 A
Cathode heater voltage = 4.75 V
Cathode heater current = 29 A
Equivalent neutral current = 282 mA

Arc Discharge			Ion Beam Performance					
V_D, V	I_D, A	P_D, W	V_{acc}, kV	V_{dec}, -kV	I_{beam}, mA	I_{drain}, mA	η_m, %	eV/Ion
45	1.1	49.4	4	1	242	0.8	85.8	204
40	1.05	42	4	1	224	0.8	79.5	188
35	1.05	36.8	4	1	205	0.8	72.7	174
30	1.04	31.2	4	1	181	0.85	64.2	172
26	0.95	24.8	4	1	145	0.9	51.4	171

∇ Magnetic configuration of Fig. 16(c)
Magnet coil currents = 8, 8, 4, 4, 2, 2, 2, 2 A
Cathode heater voltage = 4.75 V
Cathode heater current = 29 A
Equivalent neutral current = 282 mA

Arc Discharge			Ion Beam Performance					
V_D, V	I_D, A	P_D, W	V_{acc}, kV	V_{dec}, -kV	I_{beam}, mA	I_{drain}, mA	η_m, %	eV/Ion
45	1.2	54	4	1	250	0.8	88.7	216
40	1.13	45.2	4	1	231	0.8	81.9	196
35	1.12	39.2	4	1	212	0.8	75.2	185
30	1.12	33.6	4	1	188	0.85	66.7	179
25	0.98	24.4	4	1	142	0.9	50.4	172

Δ Magnetic configuration of Fig. 16(d)
Magnet coil currents = 6, 6, 6, 6, 1.5, 1.5, 1.5, 1.5, A
Cathode heater voltage = 4.75 V
Cathode heater current = 29 A
Equivalent neutral current = 282 mA

Arc Discharge			Ion Beam Performance					
V_D, V	I_D, A	P_D, W	V_{acc}, kV	V_{dec}, -kV	I_{beam}, mA	I_{drain}, mA	η_m, %	eV/Ion
45	1.15	35	4	1	240	0.8	85.2	216
40	1.05	28.5	4	1	224	0.8	78.3	190
35	1.0	24.8	4	1	200	0.8	71	175
30	0.95	49.4	4	1	175	0.9	62.1	163
27.5	0.9	42	4	1	155	0.95	55	160

TABLE V

Thruster Parameters for Performance Mappings shown in Fig. 17

Facility - 2 ft Chamber, Pressure 2.5 x 10^{-7} Torr
Cathode - Spiral Oxide, 104 W Heater Power
Magnetic Field - Uniform Configuration 2.5 A All Windings
Beam Voltage - 3 kV
Decelerating Voltage - 2 kV
Optics - Type A (48% Open Area)
Neutral Flow - 268 mA Equivalent (Standard Reverse Injection)
Parameter - Discharge Chamber Length-to-Diameter Ratio (L/D)

	L/D	V_D, V	I_D, A	P_D, W	I_B, mA	I_A, mA	η_m, %	E_I, eV/Ion
O	1.14	48.5	1.75	84.9	265	0.9	99	321
		45	1.76	79.1	258	0.9	96	306
		40	1.78	71.2	242	1.0	90	294
		35	1.78	62.3	225	1.0	84	277
		30	1.78	53.5	200	1.1	74.5	267
		25	1.65	41.3	160	1.1	59.6	258
		22	1.22	26.8	100	1.2	41	268
Δ	0.97	48.5	1.65	80	263	0.9	98.2	304
		45	1.62	72.8	255	0.9	95.2	285
		40	1.64	65.6	241	1.0	90	272
		35	1.62	56.7	225	1.0	84	252
		30	1.59	47.7	198	1.1	73.8	241
		25	1.56	39	154	1.2	57.5	253
		22.7	1.07	24.3	91	1.3	34	267
▽	0.80	48.5	1.55	75.2	264	0.9	98.5	284
		45	1.52	68.4	255	1.0	95.2	268
		40	1.54	61.6	242	1.0	90.3	254
		35	1.52	53.2	225	1.1	84	237
		30	1.53	45.9	200	1.1	74.6	230
		25	1.35	33.8	145	1.2	54.1	233
		24	1.0	24	91	1.2	34	264
□	0.63	48.5	1.43	69.4	255	0.9	95.2	272
		45	1.39	62.5	245	1.0	91.4	255
		40	1.38	55.2	232	1.0	86.5	238
		35	1.4	49	218	1.1	81.3	225
		30	1.4	42	190	1.1	70.8	221
		27.5	0.95	26.1	95	1.2	35.4	275
◇	0.45	48.5	1.31	63.5	242	0.9	90.3	262
		45	1.31	59	235	1.0	87.6	251
		40	1.3	52	225	1.0	83.9	231
		35	1.32	46.2	205	1.1	76.9	225
		32.5	1.09	35.4	126	1.2	47	281
+	0.28	48.5	1.3	63.1	205	1.0	76.5	308
		45	1.23	55.3	197	1.0	73.5	281
		40	0.78	31.2	83	1.1	31	375
		36	0.55	19.8	53	1.2	20	375

● The Data for the SERT-II Thruster are given in Table IV; Cathode Heater Power = 106 W.

TABLE VI

Thruster Parameters for Performance Mappings shown in Fig. 18

Facility - 2 ft Chamber, Pressure 2 x 10^{-7} Torr
Cathode - Spiral Oxide, 103 W Heater Power
Magnetic Field - Divergent Configuration,
Windings 1-4, 1.5 A
Windings 5-8, 6 A
Beam Voltage - 3 kV
Decelerating Voltage - 2 kV
Optics - Type A (48% Open Area)
Neutral Flow - 265 mA Equivalent (Standard Reverse Injection)
Parameter - Discharge Chamber Length to Diameter Ratio (L/D)

	L/D	V_D, V	I_D, A	P_D, W	I_B, mA	I_A, mA	η_m, %	ϵ_L, eV/Ion
○	1.14	48.5	1.09	52.8	240	0.9	90.5	220
		45	1.07	48.2	230	1.0	86.8	209
		40	1.03	41.2	213	1.0	80.4	194
		35	0.98	34.3	193	1.1	72.8	178
		30	0.93	27.9	168	1.1	63.4	166
		27	0.9	24.3	145	1.2	54.7	168
△	0.97	49	1.04	51	240	0.9	90.5	212
		45	1.02	45.8	230	1.0	86.8	200
		40	1.0	40	218	1.0	82.3	184
		35	1.0	35	199	1.0	75.0	176
		30	0.96	28.8	172	1.1	64.9	168
		27.5	0.88	24.2	150	1.2	56.6	162
▽	0.80	49	1.08	53	243	0.9	91.6	218
		45	1.04	46.8	232	1.0	87.5	202
		40	1.03	41.2	222	1.0	83.8	186
		35	1.01	35.4	202	1.1	76.3	175
		30	1.0	30	179	1.1	67.5	168
		26.8	0.9	24.2	151	1.2	57.0	160
□	0.63	48.9	1.08	52.8	241	0.9	91	219
		45	1.07	48.2	233	1.0	88	207
		40	1.08	43.2	221	1.0	83.4	196
		35	1.06	37.1	205	1.0	77.4	181
		30	0.99	29.7	178	1.1	67.2	167
		26.2	0.93	24.4	148	1.2	55.8	165
◇	0.45	48.2	1.09	52.5	232	1.0	87.5	228
		45	1.07	48.2	227	1.0	85.7	212
		40	1.06	42.4	214	1.1	80.7	198
		35	1.04	36.4	198	1.1	74.7	184
		30	1.0	30	171	1.2	64.5	176
		27.5	0.88	24.2	129	1.3	48.7	188
+	0.28	48.9	1.5	73.8	228	1.0	86	322
		45	1.5	67.4	221	1.0	83.4	305
		40	1.52	60.8	212	1.1	80	287
		35	1.25	43.8	153	1.1	57.7	286
		33.8	0.63	20.3	63	1.3	24.2	322

●SERT-II Thruster Parameters are given in Table IV; Cathode Heater Power = 106 W

TABLE VII

Beam Current (in Milliamperes) as a Function of Cathode Position for Constant Neutral Flow Rate (300 mA Equivalent) and Constant Discharge Power (Z is the Distance of the Cathode from the Screen in cm and R is the Distance of the Cathode from the Discharge Chamber Axis in cm)

Discharge Power Constant at 72 W					
R \ Z	0.3	2.5	4.7	7.3	9.8
0	180	175	185	190	210
1.3	170	185	170	185	205
2.6	155	175	160	165	175
3.8	135	145	130	135	130
5.0	105	75	85	85	75
Discharge Power Constant at 90 W					
R \ Z	0.3	2.5	4.7	7.3	9.8
0	210	215	210	225	240
1.3	205	215	215	215	240
2.6	190	200	205	210	220
3.8	160	165	170	165	165
5.0		110	90		

TABLE VIII

Thruster Parameters for Performance Mapping with Cathode Position Varied along the Discharge Axis Shown in Fig. 19

Z is the distance from cathode to screen
Equivalent neutral flow = 290 mA
Acceleration voltage = 3 kV
Deceleration voltage = 2 kV
Cathode heater voltage = 1.9 V
Cathode heater current = 24.8 A
Optics - Type A (48% open area)

	Z, cm	Arc Discharge			Ion Beam Performance			
		V_D, V	I_D, A	P_D, W	I_{beam}, mA	I_{drain}, mA	η_m, %	eV/Ion
○	9.8	45	2.5	112	255	1.8	88	441
		38	2.35	90	225	1.8	78	396
		28	2.3	65	180	2.0	62	358
		23.5	2.0	47	140	2.0	48.4	335
		21	1.7	36	100	1.8	34.5	355
□	7.3	44	2.35	104	240	1.9	82.7	432
		36.5	2.3	82	220	1.9	76	381
		34	2.1	71	200	2.0	69	357
		28	2.2	62	170	2.0	58.6	364
		22	1.95	43	120	2.0	41.5	358
△	4.7	46	2.2	102	220	2.0	74	460
		41.5	2.0	83	200	2.0	69	415
		32	2.2	70	180	2.0	62	392
		27.5	2.15	59	160	2.0	58.2	370
		23	2.09	48	130	2.0	45	369
		20.5	1.95	40	100	2.0	34.5	400
▽	2.5	48	1.9	91.2	195	2.0	67	468
		43	1.85	79.5	180	2.0	62	442
		35	1.6	56	150	2.0	52	373
		28	1.7	47.6	135	2.0	46.6	353
		22.5	1.65	37.1	100	1.9	34.5	391
◇	0.3	47	1.7	80	190	2.0	65.5	420
		37	1.9	70.4	180	2.0	62	390
		31.5	1.95	61.4	160	2.0	55.2	384
		28	1.9	53.3	140	2.0	47.2	380
		26	1.75	45.6	120	2.0	41.5	380
		23.5	1.45	34	95	1.8	32.8	360

TABLE IX

Thruster Parameters for Performance
Mappings Shown in Fig. 21

Facility - 2 ft Chamber, 2×10^{-7} Torr Pressure
Cathode - Spiral Oxide
Magnetic Field - Uniform, see Fig. 20(a)
Beam Voltage - 3 kV
Deceleration Voltage - 2 kV
Optics - Type A (48% Open Area)
Parameter - Propellant Injection

	Propellant Injection Method	P_K, W	V_D, V	I_D, A	P_D, W	I_B, mA	I_A, mA	I_N, mA (equiv.)	η_m, %	ϵ_I, eV/Ion
O	Standard Reverse	89	48.6	1.52	73.9	271	1.1	300	90.5	273
			45	1.52	68.3	267	1.0		89	256
			40	1.5	60	253	1.1		84.4	237
			35	1.43	50.1	229	1.2		76.4	218
			30	1.24	37.2	179	1.3		59.7	208
Δ	Forward	80	48.6	1.23	59.8	199	0.8	251	79.3	300
			45	1.2	54	196	0.6		78.1	275
			40	1.1	44	185	0.6		73.7	238
			35	0.98	34.3	168	0.6		66.9	204
			32.5	0.95	30.9	157	0.6		62.6	197
			30	0.85	25.5	138	0.6		55	185
□	Distributed Reverse	111	48.6	1.44	70	250	1.0	300	83.4	280
			45	1.4	63	245	1.0		81.7	257
			40	1.35	54	228	1.0		76	237
			35	1.25	43.7	205	1.1		68.4	214
			30	1.1	33	155	1.2		51.7	213
			28.5	0.82	23.4	120	1.1		40	195

TABLE X

Thruster Parameters for Performance Mappings
Shown in Fig. 22

Facility - 2 ft Chamber, 2×10^{-7} Torr Pressure
Cathode - Spiral Oxide
Magnetic Field - Divergent, see Fig. 20(b)
Beam Voltage - 3 kV
Decelerating Voltage - 2 kV
Optics - Type A (48% Open Area)
Parameter - Propellant Injection

	Propellant Injection Method	P_K, W	V_D, V	I_D, A	P_D, W	I_B, mA	I_A, mA	I_N, mA (equiv.)	η_m, %	ϵ_I, eV/Ion
O	Standard Reverse	141	48.9	1.34	65.6	241	0.7	285	84.5	272
			45.1	1.28	57.8	232	0.8		81.5	249
			40	1.27	50.8	218	0.8		76.5	233
			35	1.28	44.8	203	0.9		71.2	221
			30	1.17	35.1	170	1.0		59.7	206
			27.9	0.87	24.3	118	1.0		41.4	203
Δ	Distributed Reverse A	111	48.9	1.1	53.8	252	0.9	310	81.3	214
			45.0	1.05	47.3	240	1.0		77.5	197
			40	1.05	42	222	1.0		71.6	189
			35	1.01	35.4	197	1.1		63.6	179
			30	0.9	27	149	1.1		48	181
□	Distributed Reverse B	104	49	1.02	50	228	0.9	255	89.5	219
			45	1.0	45	220	1.0		86.4	204
			40	0.99	39.6	207	1.0		81.3	191
			35	0.98	34.3	188	1.0		73.8	182
			30	0.88	26.4	142	1.1		55.8	186

TABLE XI

Thruster Parameters for Performance Mappings
Shown in Fig. 23

Facility - 2 ft Chamber, 2×10^{-7} Torr Pressure
Cathode - Spiral Oxide
Magnetic Field, Uniform Configuration of Fig. 16(a)
Divergent Configuration of Fig. 16(d)
Beam Voltage, 3 kV
Decelerating Voltage, 2 kV
Optics - Type A (48% Open Area)
Type B (71% Open Area)
Propellant Injection - Standard Reverse
Parameter - Magnetic Configuration and Optic Open Area

	Magnetic Configuration	Optics	P_K, W	V_D, V	I_D, A	I_B, mA	I_A, mA	I_N, mA (equiv.)	η_m, %	ϵ_I eV/Ion
●	2A	A	104	48.5	1.55	264	0.9	268	98.5	284
				45	1.52	255	1.0		95.2	268
				40	1.54	242	1.0		90.3	254
				35	1.52	225	1.1		84	237
				30	1.53	200	1.1		74.6	230
				25	1.35	145	1.2		54.1	233
▲	2B	A	103	49	1.08	243	0.9	265	91.6	218
				45	1.04	232	1.0		87.5	202
				40	1.03	222	1.0		83.8	186
				35	1.01	202	1.1		76.3	175
				30	1.0	179	1.1		67.5	168
				26.8	0.9	151	1.2		57	160
○	2A	B	102	48	1.25	312	0.9	320	97.5	192
				45	1.22	301	1.0		94	182
				42.5	1.22	291	1.0		91	178
				40	1.22	281	1.1		87.8	173
				37.5	1.24	269	1.2		84	173
				35	1.24	256	1.3		80	170
				32.5	1.22	235	1.5		73.5	169
				30	1.18	210	1.7		65.6	169
				27.5	1.05	168	2.2		52.5	177
△	2B	B	101	48.3	1.01	297	1.2	330	90	164
				45	0.99	282	1.3		85.5	158
				42.5	0.98	271	1.3		82	154
				40	0.98	260	1.4		78.8	150
				37.5	0.99	252	1.4		76.4	148
				35	0.97	238	1.5		72.1	143
				32.2	0.95	218	1.7		66	140
				30	0.9	196	1.9		59.4	138

TABLE XII

Langmuir Probe Data shown in Figs. 24 through 26

Discharge Parameters are given in Fig. 24
Distance from Probe Position to Cathode Plane - Z
Distance from Probe Position to Discharge Axis - R
Plasma Potential - V_p
Plasma Density - n_p
Plasma Electron Temperature - T_e (Maxwellian Velocity Distribution)
Parameter - Magnetic Field Configuration

Magnetic Configuration	Z, cm	R, cm	V_p, V	T_e, eV	10^{11} n_p cm^{-3}
16A	3	0	53.5	9.0	6.2
		2.5	50.5	7.0	4.4
		5	55	3.5	4.0
		7	52.4	5.0	2.7
	6	0	54.5	16.9	7.9
		2.5	54	10.5	3.6
		5	53.2	7.6	2.9
		7	48.2	3.3	2.7
	9	0	46.5	13.8	6.6
		2.5	48.6	11.7	3.3
		5	46.3	8.4	2.7
		7	48.3	4.4	2.7
	12	0	46	16.4	2.9
		2.5	45.8	12.8	2.0
		5	44.8	11.1	1.5
		7	43.1	8.4	1.6
16D	3	0	53.8	10.3	5.0
		2.5	52.8	6.2	4.2
		5	51	3.2	4.0
		7	50.2	3.0	3.9
	6	0	52.5	10.2	4.6
		2.5	52.5	8.7	3.9
		5	54.5	8.5	3.4
		7	53.9	3.8	3.1
	9	0	51.3	13.4	4.6
		2.5	51	11.3	4.8
		5	49.8	9.4	4.6
		7	51.2	8.6	4.1
	12	0	46.8	12.8	3.0
		2.5	48.7	12.8	3.3
		5	50.2	12.2	3.7
		7	50.8	10.8	3.0

TABLE XIII

Langmuir Probe Data Shown in Figs. 27 through 29

Discharge Parameters are given in Fig. 27
Distance from Probe Position to Cathode Plane Z
Distance from Probe Position to Discharge Axis R
Plasma Potential V_p
Plasma Density n_p
Primary Electron Density n_1
Primary Electron Energy eV_o
Maxwellian Electron Density n_2
Maxwellian Electron Temperature T_e
Parameter - Magnetic Field Configuration

Magnetic Configuration	Z, cm	R, cm	V_p, V	n_p, 10^{11} cm^{-3}	n_1, 10^{10} cm^{-3}	eV_o, eV	n_2, 10^{10} cm^{-3}	T_e, eV
16A	0.46	1	40.6	1.5	2.7	36	12	9.1
		3	38.1	0.5	0.9	27	3.8	4.2
		5	42.2	0.1	0.06	32	1.0	4.3
		7	41.6	0.008	0.02	11	0.06	1.3
	2	1	41.7	2.2	2.1	39	20	7.3
		3	40.8	1.0	0.4	35	9.5	5.5
		5	40.4	0.2	0.1	23	1.6	3.0
		7	40.5	0.03	0.004	8	0.3	0.5
	4	1	42	2.4	2.1	38	22.3	6.8
		3	41.5	1.3	0.6	36	11.9	4.8
		5	40.5	0.3	0.2	25	2.9	2.5
		7	41.9	0.08	0.01	8	0.8	0.6
	6	1	42.2	2.5	2	37	23	7
		3	41.8	1.4	0.6	34	13.1	5.3
		5	40.8	0.43	0.2	27	4.1	3.4
		7	41.5	0.08	0.08	6	0.76	0.5
	8	1	40.9	2.2	2	37	20	6.7
		3	41	1.3	0.7	36	12	5.5
		5	40.8	0.5	0.2	36	4.6	4.0
		7	41.9	0.09	0.02	17	0.9	1.2
	10	1	39.6	1.8	1.7	36	16.1	7.1
		3	38.9	1.0	0.7	34	9.1	6.0
		5	39.1	0.4	0.2	30	3.8	4.4
		7	41.5	0.09	0.02	22	0.9	2.0
	11.2	1	38	1.2	1.5	36	10.4	9
		3	37	0.7	0.5	33	6.6	6.7
		5	37.7	0.4	0.3	32	3.3	4.6
		7	38.2	0.08	0.03	29	0.8	4.6
16D	0.46	1	42.4	1.7	1.27	38	16	4.6
		3	41.8	0.4	0.17	38	3.7	3.7
		5	40.8	0.05	0.03	13	0.5	0.9
		7	43.8	0.01	0.01	9	0.1	1.3
	2	1	42.7	2.1	1.4	35	20	4.9
		3	42.3	0.7	0.2	31	7.3	3.1
		5	42.9	0.1	0.01	17	1.0	0.8
		7	42.6	0.02	0.001	7	0.02	0.7
	4	1	42.6	2.2	1.5	35	20.8	4.6
		3	43	0.6	0.2	29	5.9	3.5
		5	41.9	0.1	0.03	8	1.3	0.7
		7	43.2	0.04	0.02	3	0.4	0.7
	6	1	43	2.5	1.7	37	23	5.3
		3	42.5	1.2	0.6	30	11	3.2
		5	43.3	0.3	0.06	16	3.3	1.7
		7	42.4	0.06	—	—	0.6	0.6
	8	1	42.9	2.3	1.8	37	21.4	5.3
		3	42.5	1.3	0.6	34	11.7	4.2
		5	42.3	0.4	0.1	28	4.1	3.1
		7	42.7	0.08	0.01	8	0.8	0.6
	10	1	42.1	1.6	1.5	35	14.5	5.3
		3	42.1	0.9	0.7	36	8.2	5.1
		5	42.3	0.4	0.3	34	4.0	4.0
		7	43.2	0.1	0.05	9	1.0	1.5
	11.2	1	38.9	1.1	1.1	37	9.6	6.8
		3	39	0.6	0.7	34	5.8	6.6
		5	39	0.3	0.3	34	3.1	6.4
		7	41.5	0.09	0.09	30	0.8	4.1

TABLE XIV

Thruster Parameters for Performance Mappings Shown in Fig. 33

Facility - 5 ft Vacuum Chamber Facility, 5×10^{-7} Torr
Cathode - Hollow (NASA LeRC)
Magnetic Field - Configurations 34, 35 and 36
Beam Voltage - 3 kV
Decelerating Voltage - 2 kV
Optics Type A
Propellant Injection - Standard Reverse

	Magnetic Configuration	V_D, V	I_D, A	I_B, mA	I_N (total) mA (equiv.)	I_N (Hollow Cathode), mA (equiv.)	η_m, %	ϵ_I, eV/Ion
△	34	33	1.4	120	300	50	40	384
		33.5	1.8	152			50.6	397
		34.2	2.2	185			61.5	406
		35	2.6	210			70	434
		35	3.0	230			76	457
		35	3.4	255			84.9	466
		35	3.6	270			90	470
▽	35	34	1.4	140	300	50	46.6	330
		34	1.8	170			56.6	361
		34	2.3	200			66	391
		34	2.8	235			78.2	404
		34	3.4	263			87.5	434
		34	3.8	280			93	460
○	36	32.5	1.0	110	302	19	36.4	295
		34	1.4	160			53	298
		34.2	1.8	197			65.3	313
		35	2.2	228			75.6	338
		35	2.6	249			82.5	366
		36	3.0	260			86.2	415
		37.5	3.4	275			91.2	466

TABLE XV

Thruster Parameters for Performance Mappings
Shown in Fig. 41

Facility - 9 ft Vacuum Chamber, 10^{-7} Torr Press
Cathode - Hollow
Magnetic Field - Configurations 36 and 42
Beam Voltage - 3 kV
Decelerating Voltage - 2 kV
Optics Type A for Configuration 36 and 42, Type B for 42

	Magnetic Configuration	Optics	$V_{D'}$ V	$I_{D'}$ A	$I_{B'}$ mA	I_N (total) mA (equiv.)	I_N (Hollow Cathode), mA (equiv.)	$\eta_{m'}$ %	$\epsilon_{I'}$ eV/Ion
□	36	A	32.5	1.0	110	302	19	36.4	295
			34	1.4	160			53	298
			34.2	1.8	197			65.3	313
			35	2.2	228			75.6	338
			35	2.6	249			82.5	366
			36	3.0	260			86.2	415
○	42	A	34	1.2	135	272	61	49.7	302
			35	1.8	190			70	331
			36	2.2	220			81.5	360
			37	2.6	240			88	401
			38	3.0	260			96	438
△	42	B	31	1.4	170	258	32	67	255
			35	1.6	208			80.6	269
			40	1.8	239			92.5	301
			45	2.2	250			97	395

TABLE XVI

Langmuir Probe Data used in Fig. 44

Discharge Parameters are given in Fig. 44
Distance from Probe Position to Cathode Plane Z
Distance from Probe Position to Discharge Axis R
Plasma Potential V_p
Plasma Density n_p
Primary (Monoenergetic) Electron Density n_1
Primary Electron Energy eV_o
Maxwellian Electron Density n_2
Maxwellian Electron Temperature T_e

Z, cm	R, cm	V_p, V	n_p x 10^{10}	n_1 10^{10}	eV_o, eV	n_2 10^{10}	T_e, eV
0.37	0.5	14	2.9	0.2	31	2.8	2.1
	1.0	14	2.3	0.2	34	2.2	2.2
	1.8	13.5	1.7	0.2	32	1.5	2.1
1.5	0	14.3	16.7	0.1	33	16.6	1.2
	0.5	14.2	15.2	0.1	40	15.1	1.2
	1.0	13.9	8.7	0.1	38	8.6	1.3
	1.8	13.8	3.0	0.1	46	2.9	1.6
2.5	0	13.2	14.5	0.1	45	14.4	1.0
	0.5	14.0	10.8	0.2	26	10.6	1.3
	1.0	14.2	4.2	0.2	32	4.1	1.9
	1.8	14.8	1.9	0.1	36	1.8	2.7
3.4	0	12.7	2.6	0.3	19	2.3	1.9
	1	15.1	2.1	0.7	12	1.4	1.4
	2	35	6	1.0	29	5.2	5.5
	3	36.8	5.9	0.3	39	5.6	5.7
	4	37.1	4.2	0.2	40	4.0	4.3
	5	37.2	2.9	0.2	55	2.7	3.6
	6	37	1.4	0.1	67	1.3	2.6
5.0	0	37.7	14.2	0.2	32	14.0	9.3
	2	37.3	9.9	0.1	33	9.8	7.2
	4	37.2	5.4	0.2	41	5.2	4.9
	6	36.6	1.5	0.1	60	1.4	3.0
6.9	0	37	12.5	0.3	31	12.4	9.3
	2	36	7.0	0.3	26	6.8	5.0
	4	36.5	4.9	0.5	30	4.4	4.3
	6	39.5	2.0	0.1	69	1.9	3.5
8.8	0	38.6	9.0	0.6	27	8.4	7.5
	2	35.5	6.5	0.3	25	6.2	4.9
	4	34.9	4.1	0.5	32	3.7	4.1
	6	39.3	2.2	0.1	52	2.1	2.7

TABLE XVII

Thruster Parameters for Performance Mappings Shown in Fig. 47

The Radial Field Thruster Configuration is shown in Fig. 46
Facility - 9 ft Chamber 1 x 10^{-7} Torr Pressure
Cathode - Hollow
Beam Voltage - 3 kV
Decelerating Voltage - 2 kV
Optics - Type B
Propellant Injection - Standard Reverse Using 40 Injection Orifices

	V_D, V	I_D, A	I_B, mA	I_A, mA	I_N, mA (equiv.)	η_m, %	ϵ_I, eV/Ion
O	35.7	0.8	159	1.8	334	47.6	180
	37	0.83	180	1.8		53.9	170
	39	0.9	200	1.75		60	175
	43	0.98	235	1.8		70.5	179
	45	1.05	260	2.3		78	182
	50	1.3	290	2.6		87	224
Δ	36	1	200	2.6	426	47	181
	35	1.2	220	2.6		51.7	190
	36	1.4	280	2.5		65.8	180
	38	1.6	330	2.1		77.5	185
	40	1.8	360	2.0		84.6	200
	45	2.2	400	2.8		94	257

TABLE XVIII

Hourly Readings of Radial Field Thruster Parameters Taken During the 24 Hour Test

Hour	V_D, V	I_D, A	I_B, mA	I_A, mA	I_n (Feed System) mA	I_n (Hollow Cathode), mA
0	44	1.2	270	1.3		
1	43	1.05	265	1.6	262	29
2	46	1.05	280	1.6	296	45
3	48	1.05	280	1.5		
4	48	1.05	270	1.6	330	47
5	48	1.1	255	1.7	280	50
6	48	1.1	255	1.5	270	43
7	48	1.05	255	1.7	262	40
8	47	1.19	270	1.6	287	32.4
9	45	1.2	275	1.4	287	41.4
10	45.5	1.1	270	1.4	254	39.6
11	46	1.1	265	1.4	262	41.2
12	46.1	1.09	265	1.4	254	37.0
13	46.5	1.0	262	1.4	254	36.0
14	46	1.0	250	1.5	339	37.0
15	48	0.9	245	1.4	339	41.4
16	48	1.1	250	1.8	271	27
17	47	1.2	250	1.6	284	25.2
18	46	1.2	250	1.4	266	28.8
19	46	1.0	250	1.4	266	33.2
20	48	1.0	250	1.4	258	35.4
21	47	1.1	250	1.8	259	32.4
22	47	1.0	250	1.6	270	21.6
23	48	1.0	250	1.8	312	20
24	46	1.05	250	1.4	270	34

TABLE XIX

Four Hour Averages of Radial Field Thruster Parameters
Monitored During 24 Hour Test

Hours	V_D, V	I_D, A	I_B, mA	I_A, mA	I_N (total) mA (equiv.)	I_N (Hollow Cathode) mA (equiv.)	η_m, %	ϵ_I, eV/Ion
1-4	46.2	1.05	274	1.6	344	36.2	80.2	177
5-8	47.2	1.13	259	1.6	316	41.6	82	205
9-12	45.7	1.12	269	1.4	304	39.6	88.6	190
13-16	47.1	1.02	252	1.5	336	35.6	75.1	192
17-20	46.7	1.09	252	1.4	294	30.2	85.6	201
21-24	47.0	1.07	250	1.6	315	32	79.4	195
24 Hour Average	46.6	1.08	260	1.5	318	35.8	81.6	193

TABLE XX

Approximate Collision Data for a Thruster Discharge with Uniform B-Field and Low Transmission Optics

Collision Partners	Mean Free Path, cm		Collision Frequency, sec^{-1}	
	Discharge		Discharge	
	Center	Edge	Center	Edge
Atom-atom[a]	200		150	
Ion-atom[b]	200		150	5×10^2
Electron-atom[c]	400	200	4×10^5	5×10^5
Ion-ion	1	30	10^5	8×10^3
Electron-ion	140	20	1.2×10^6	5×10^6

[a] See Ref. 12
[b] See Ref. 13
[c] See Ref. 14

TABLE XXI

Diffusion Coefficients and Ionization Rates for Different Distribution Functions

Location	Distribution Function		Diffusion Coefficient[a] $cm^2\ sec^{-1}$	Ionization Frequency, $sec^{-1}\ Torr^{-1}$
	Type	Energy, eV		
Discharge Center	Pure Maxwellian	17.5	1.8×10^5	3.4×10^9
	1:9 Mixture Mono/Maxw	40/15	1.86×10^5	3.2×10^9
Near Anode	Pure Maxwellian	6.7	9.7×10^4	1.0×10^9
	1:9 Mixture Mono/Maxw	40/3	1.27×10^5	0.95×10^9

[a] for B = 20 gauss.

TABLE XXII

Estimate of the Dependence of Propellant Utilization on Neutral Mean Free Path (l = length of chamber)

ℓ/λ	η_m, %
2	40
1	63
0.83	70
0.67	78
0.5	86

VI. FIGURES

The figures referenced in the text appear in this section.

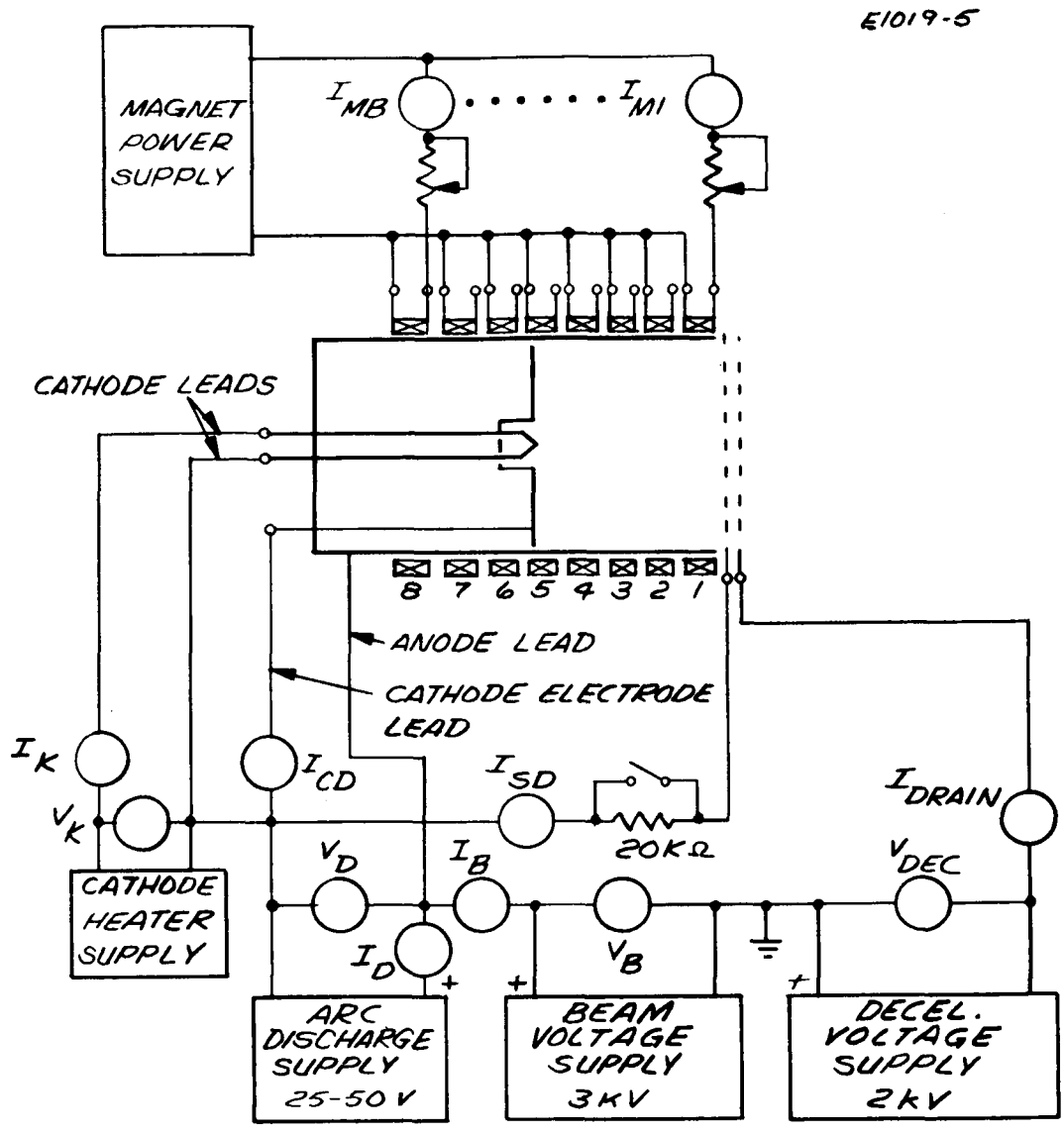

I_K - CATHODE HEATER CURRENT (A)
V_K - CATHODE HEATER VOLTAGE (V)
I_{CD} - CATHODE ELECTRODE CURRENT (A) +INDICATES IONS COLLECTED
I_{SD} - SCREEN ELECTRODE CURRENT (A) +INDICATES IONS COLLECTED
I_D - DISCHARGE CURRENT (A)
V_D - DISCHARGE VOLTAGE (V)
I_B - ION BEAM CURRENT (mA)
I_{DRAIN} - ACCEL ELECTRODE INTERCEPTION CURRENT (mA)
V_B - ION BEAM VOLTAGE
V_{DEC} - DECELERATION VOLTAGE

Fig. 1. Schematic circuit diagram of power conditioning and thruster electrodes.

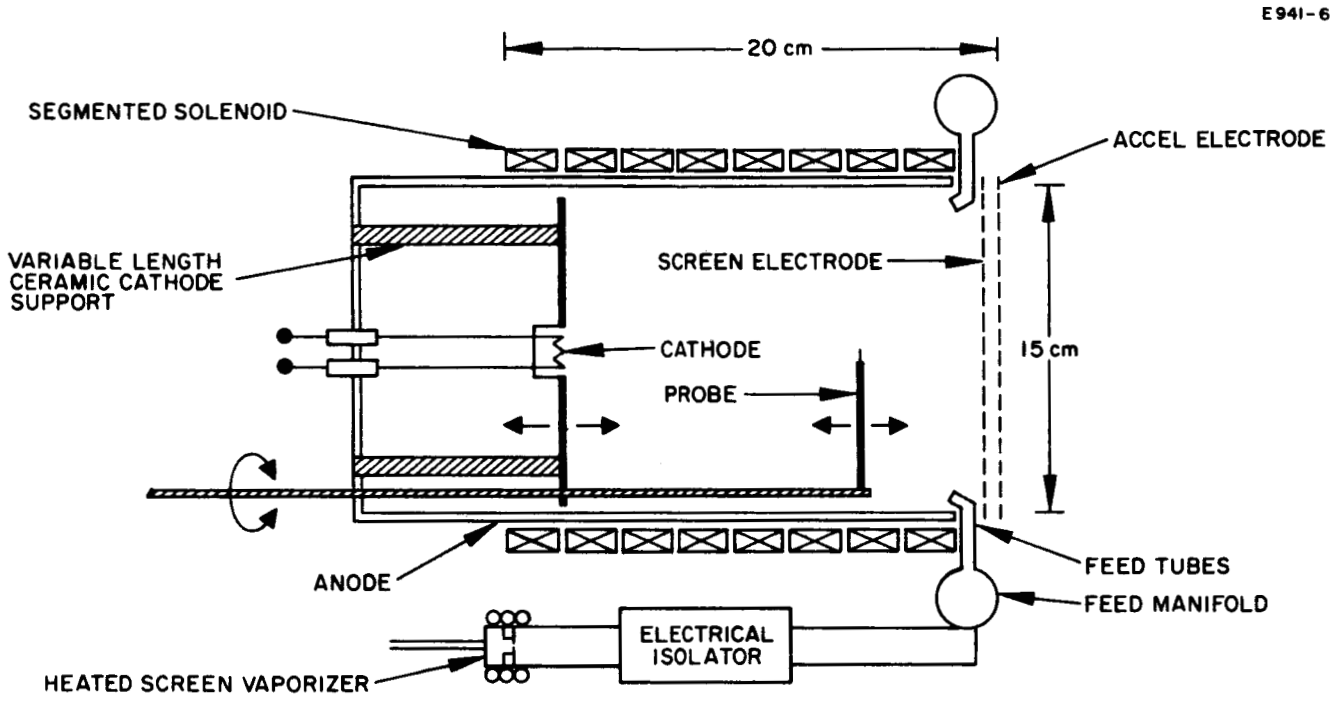

Fig. 2. Schematic drawing of the versatile experimental thruster used in diagnostic and optimization experiments.

M 4830

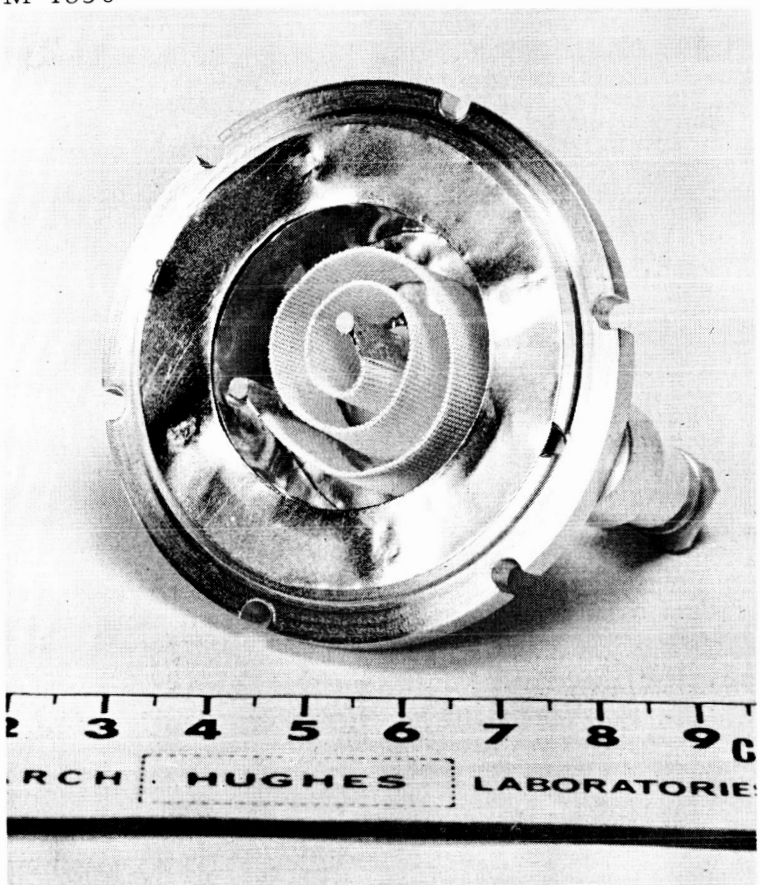

Fig. 3. Spiral oxide cathode (design 4A) before test.

M 6111

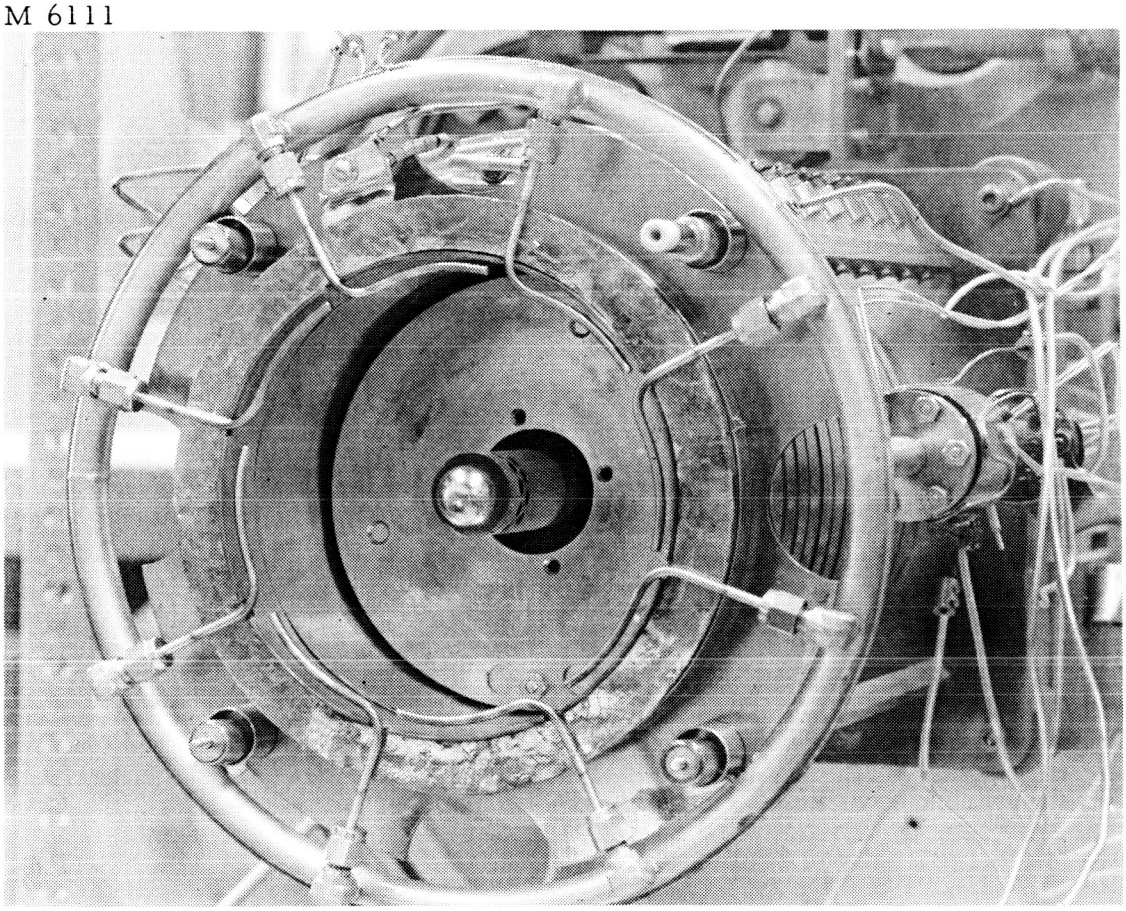

(a) View with ion optics removed.

Fig. 4. Radial field thruster.

M 6112

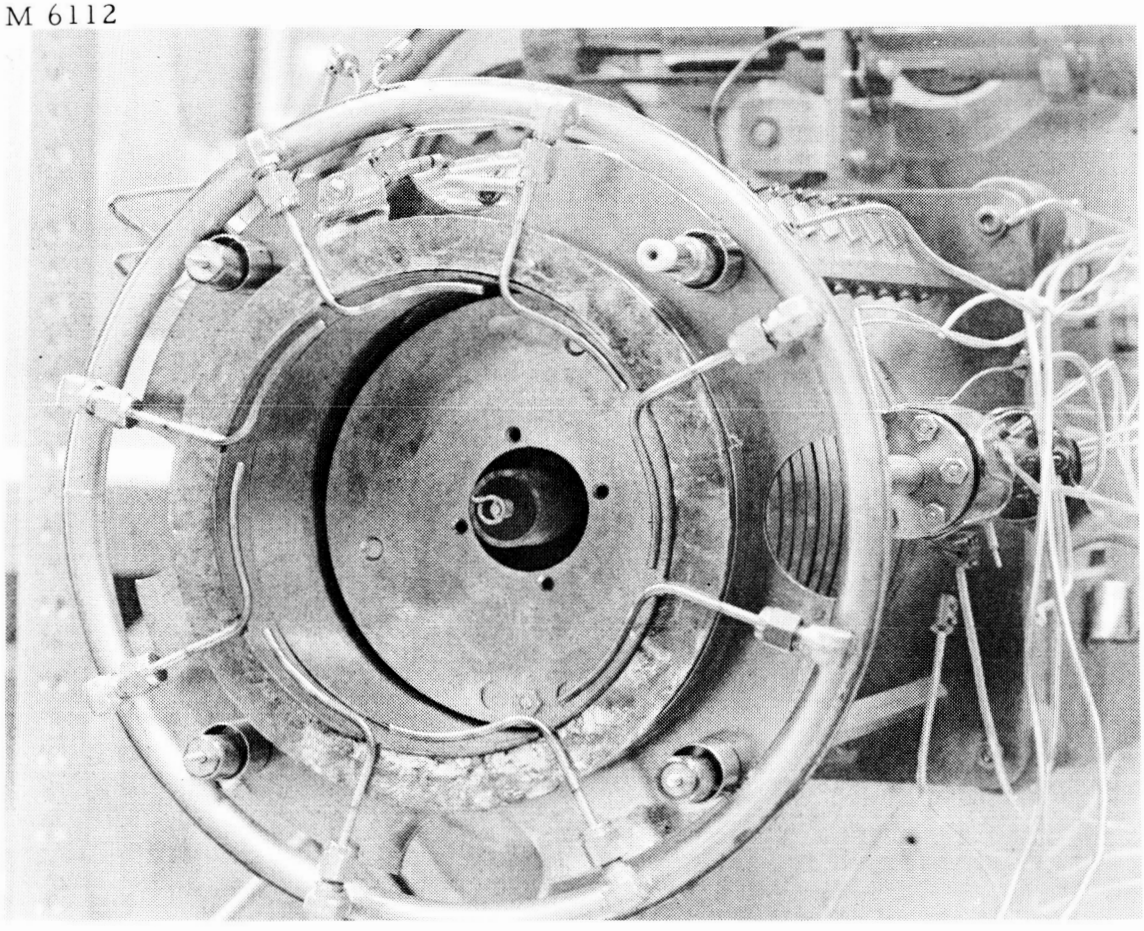

(b) View with ion optics and cathode baffle-pole piece removed.

Fig. 4. (Cont'd).

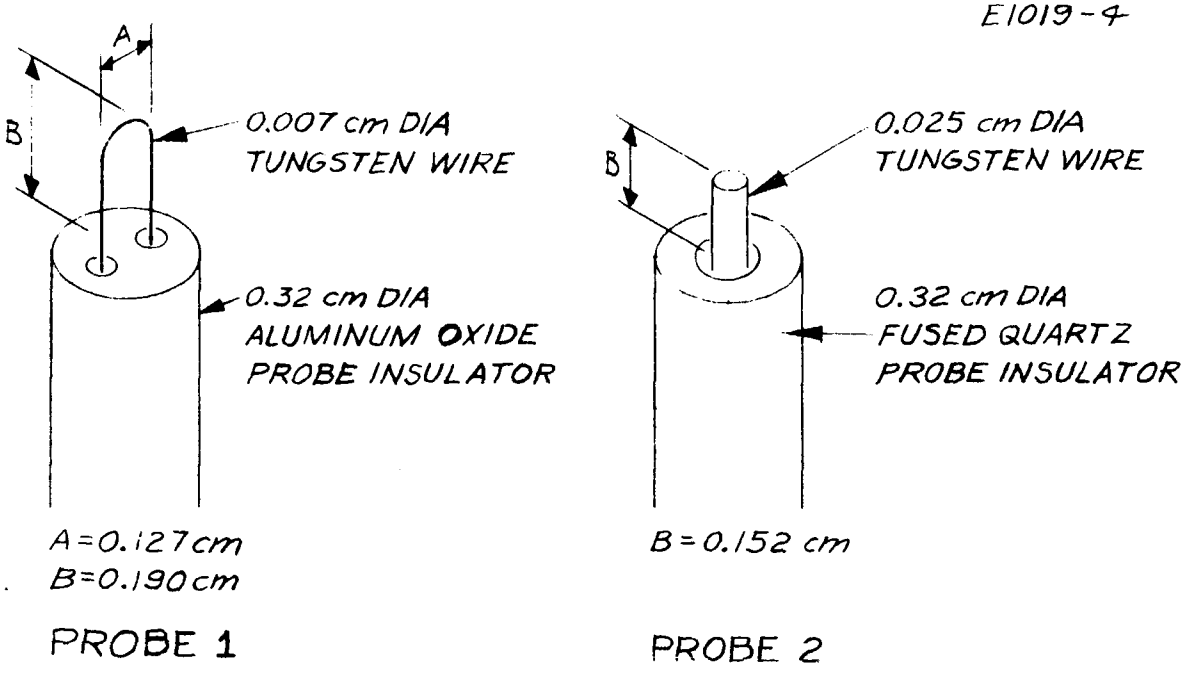

Fig. 5. Drawing of Langmuir probes used in this investigation.

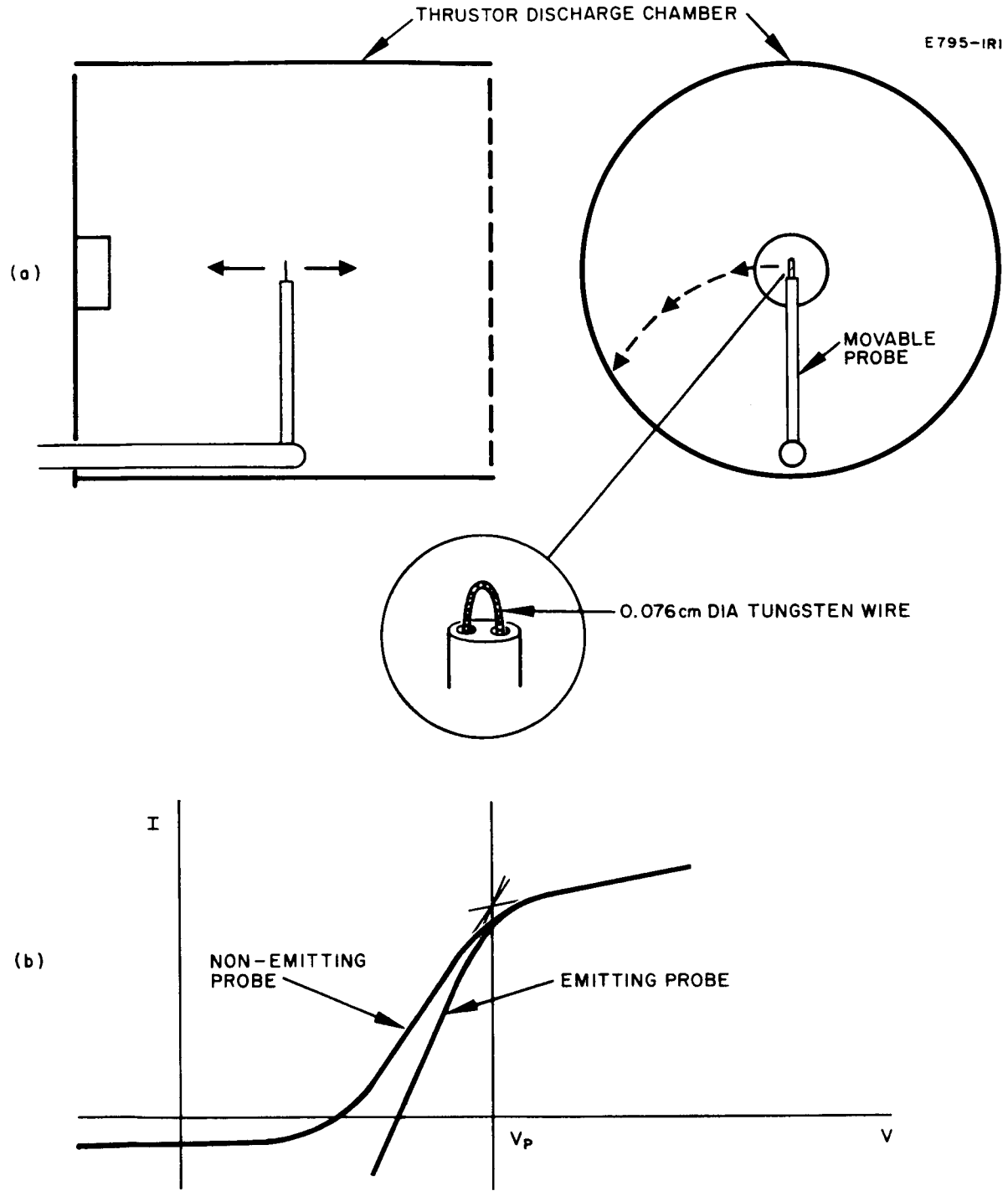

Fig. 6. Langmuir probe technique. (a) Geometry and positioning. (b) Superimposed emitting and nonemitting probe characteristics.

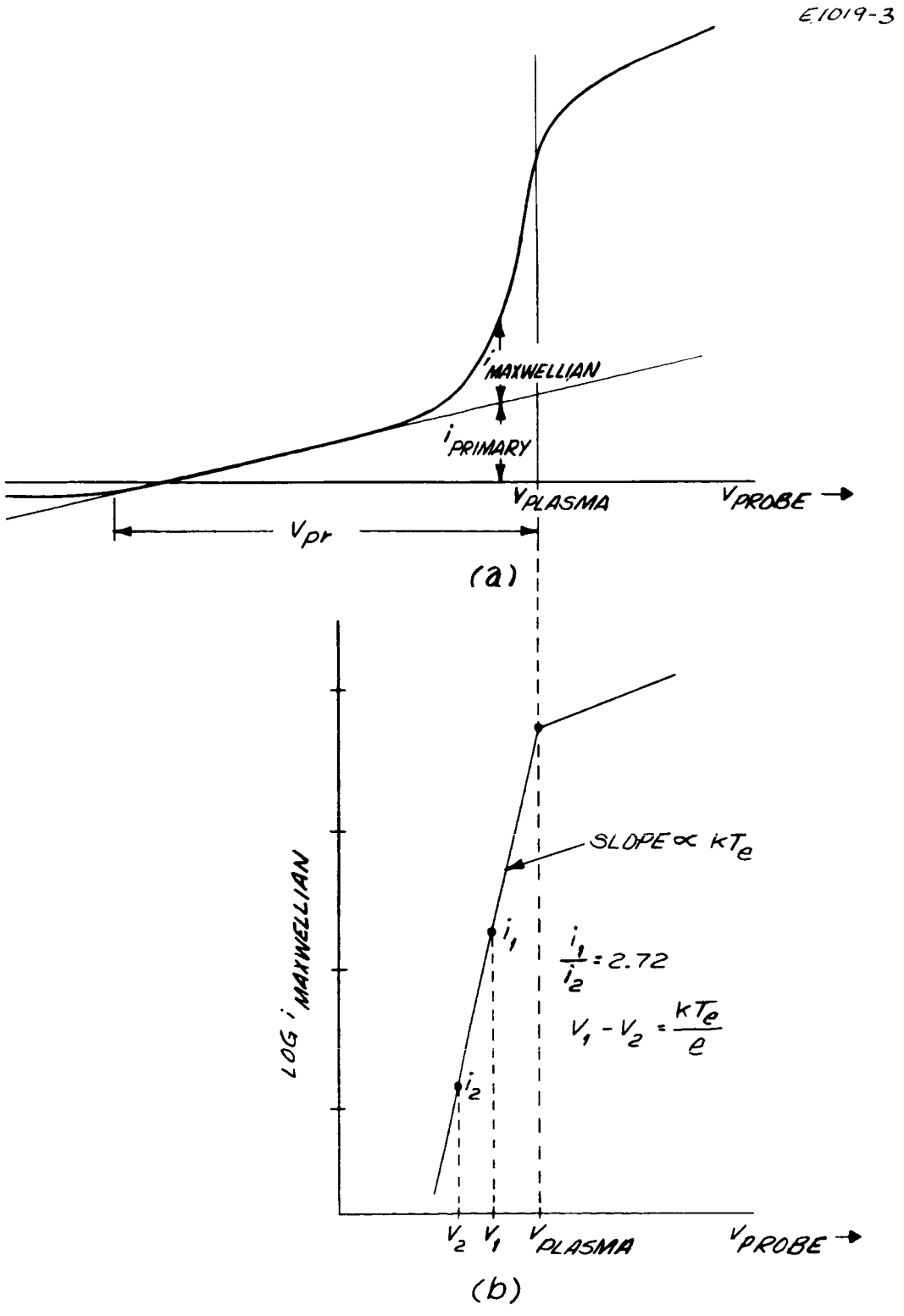

Fig. 7. Idealized Langmuir probe characteristics.

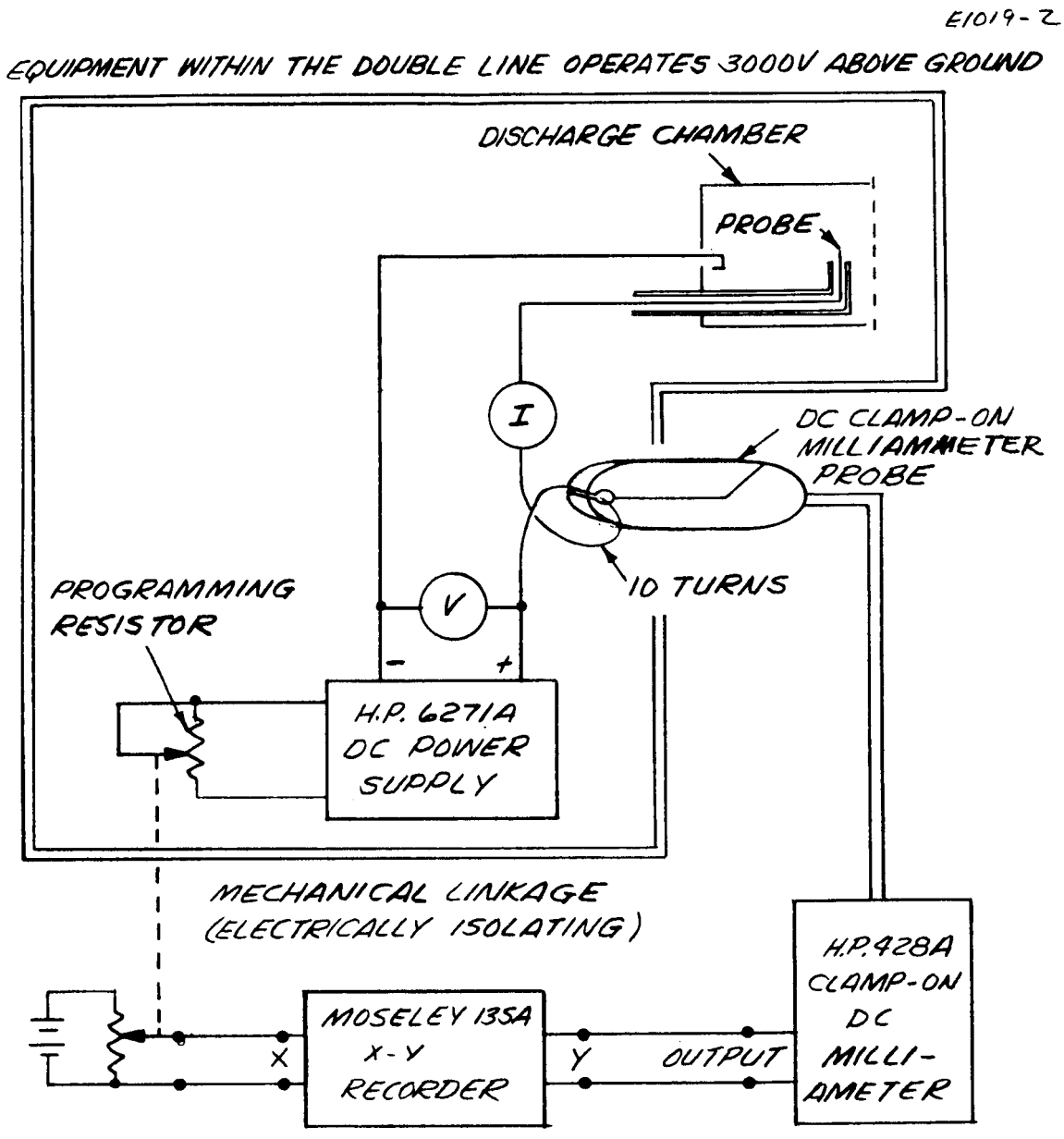

Fig. 8. Block diagram of Langmuir probe voltage sweeping, data recording equipment.

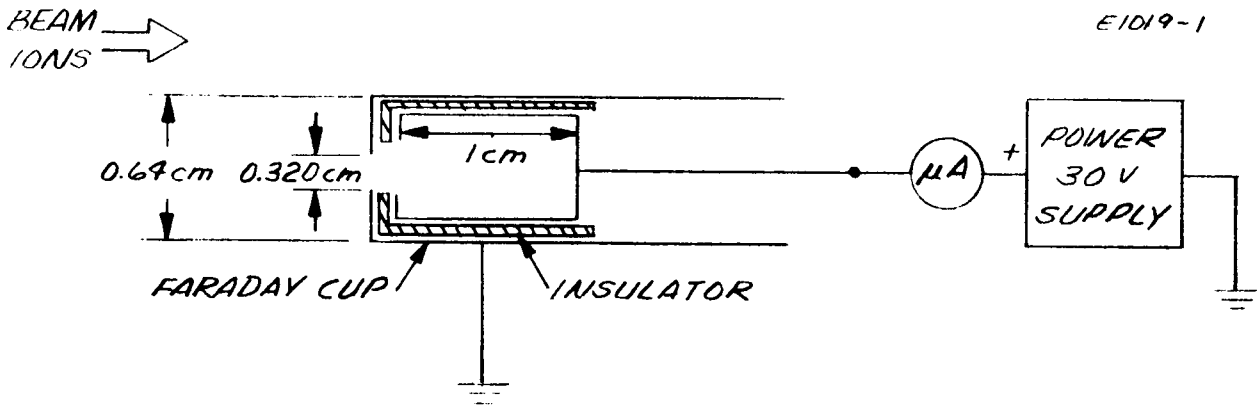

Fig. 9. Faraday cup beam probe.

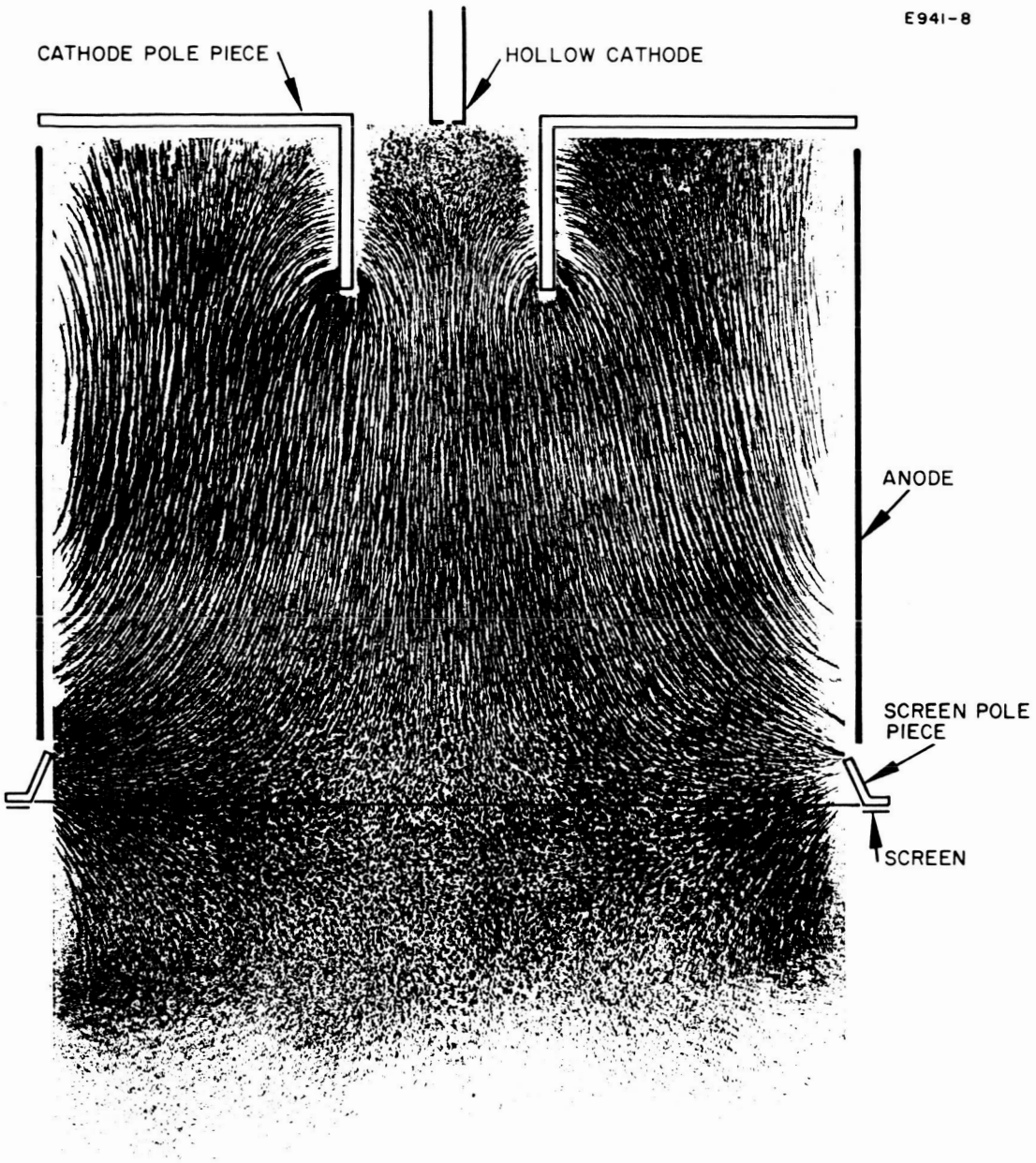

Fig. 10. Photograph of powdered iron field map of magnetic field configuration in a thruster discharge chamber. This map was made in the SERT-II model, permanent thruster. (Discharge chamber electrodes are sketched.)

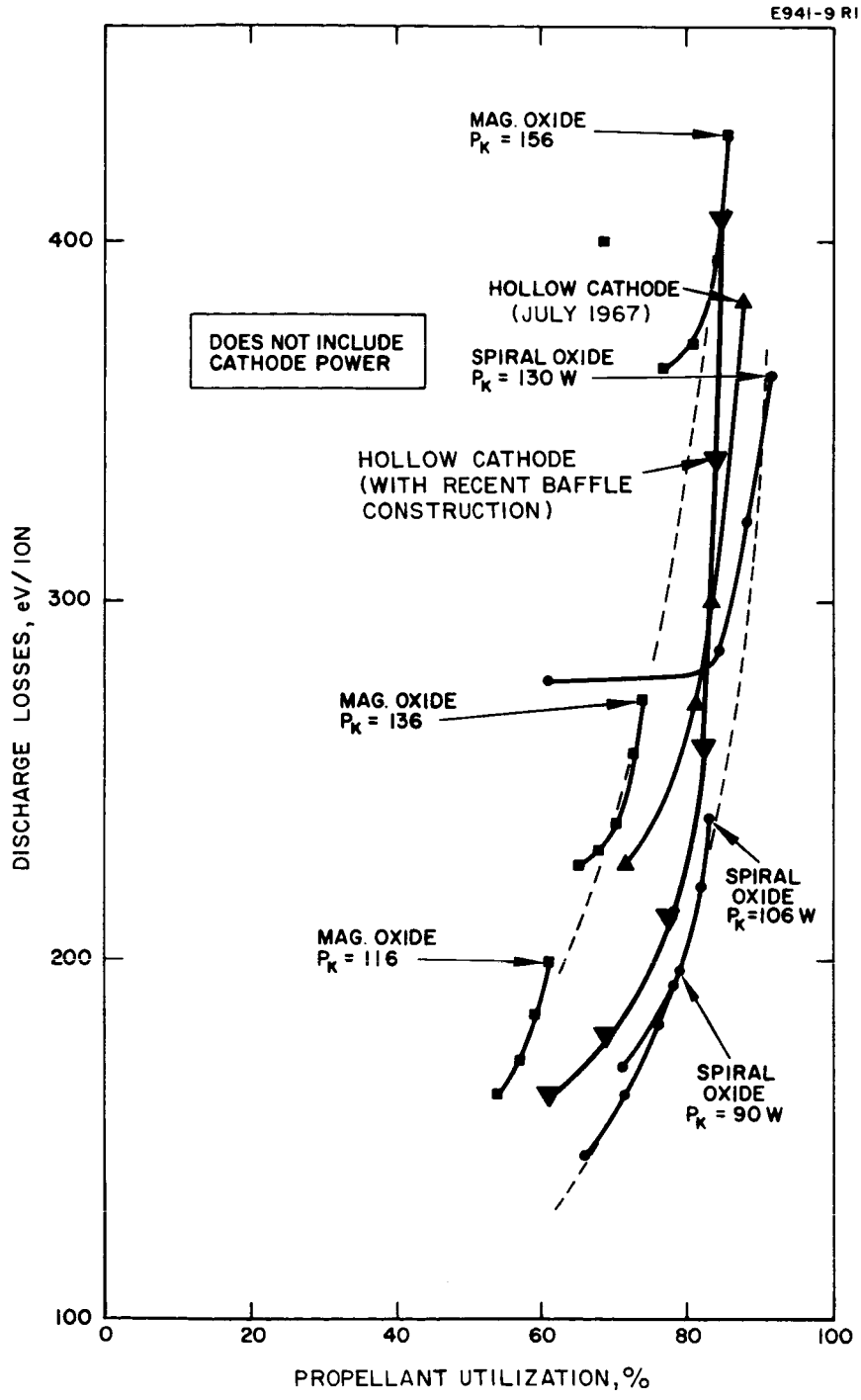

Fig. 11. Performance mapping of NASA-LeRC SERT II model permanent magnet thruster for three cathode types. (See Table II for thruster parameters.)

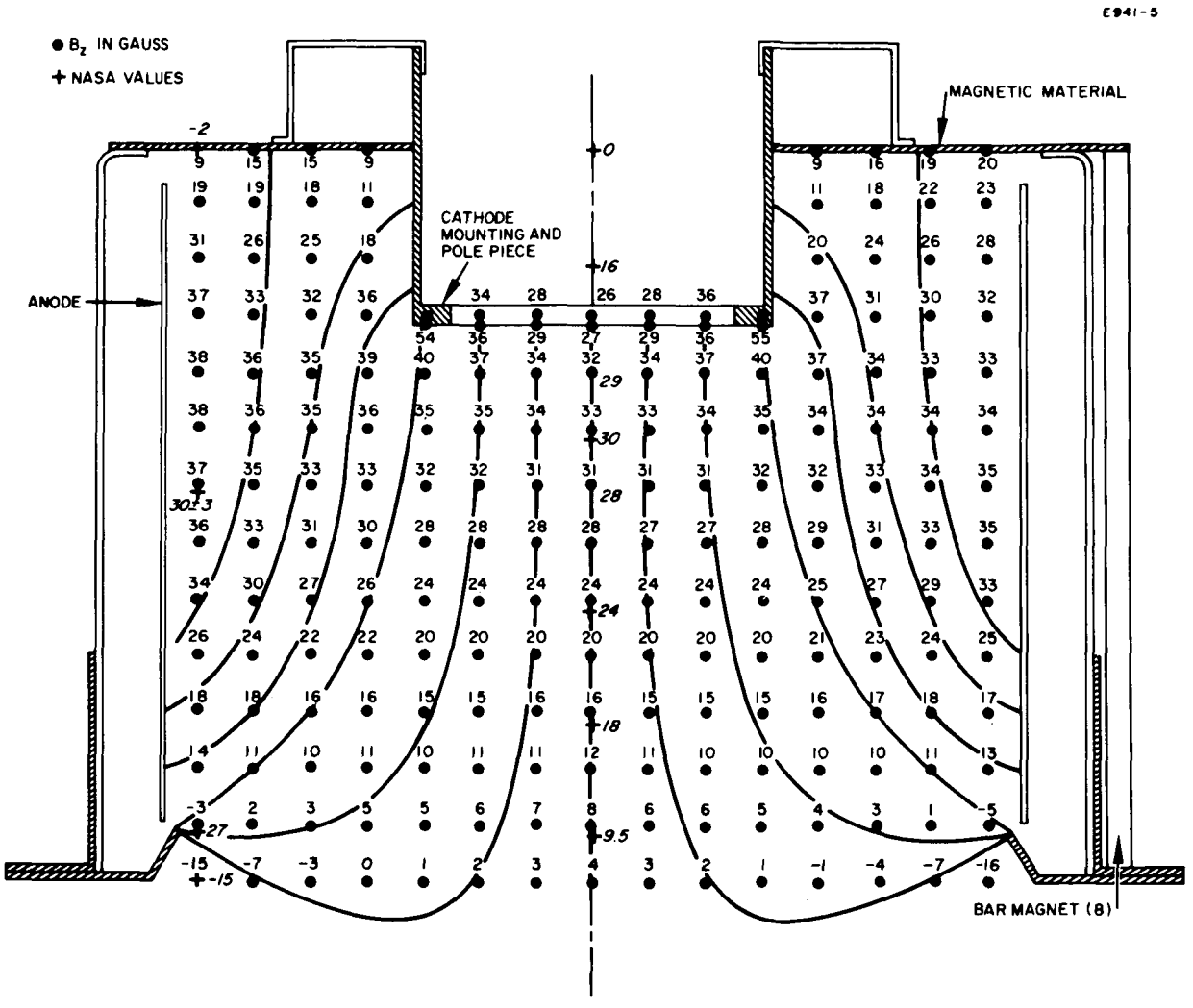

Fig. 12. Schematic drawing of NASA-LeRC II model discharge chamber showing magnetic field shape and axial field strength.

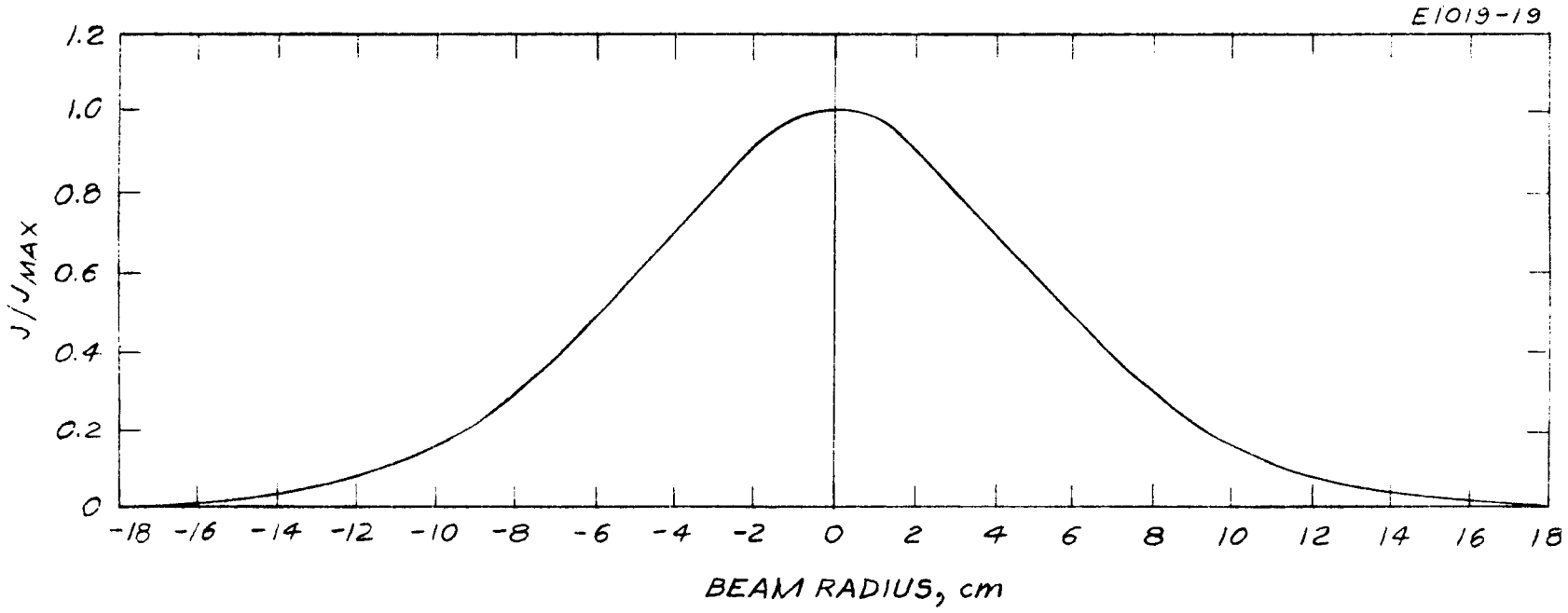

Fig. 13. Normalized ion beam profile for NASA LeRC SERT-II thruster measured at a plane 18 cm downstream from the accel electrode.

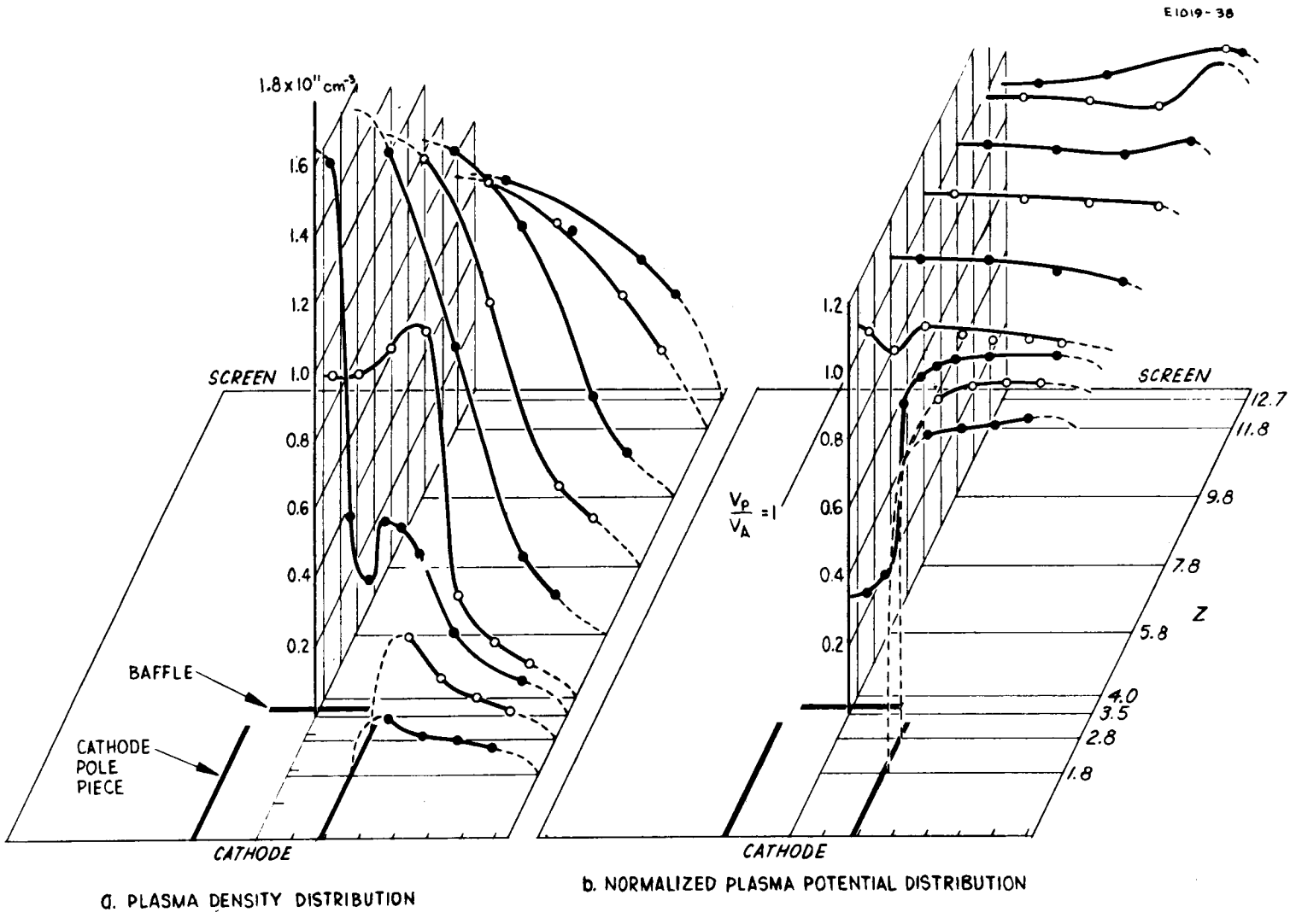

Fig. 14. Probe data obtained with type 2, shown in Fig. 5. See Table III for thruster parameters and data. (a) Plasma density. (b) Normalized plasma potential.

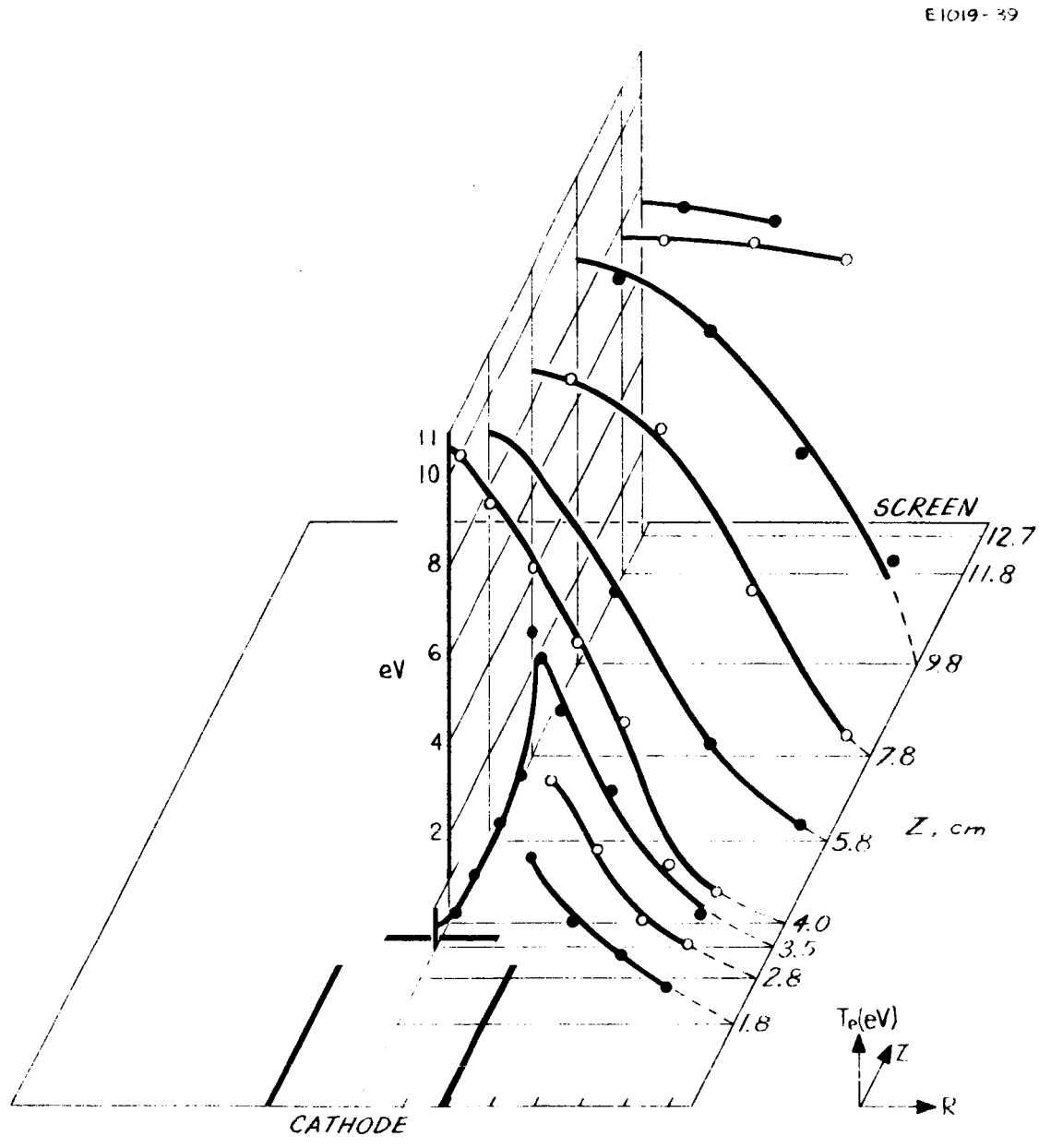

(c) Maxwellian electron temperature in the SERT-II thruster.

Fig. 14. (Cont'd).

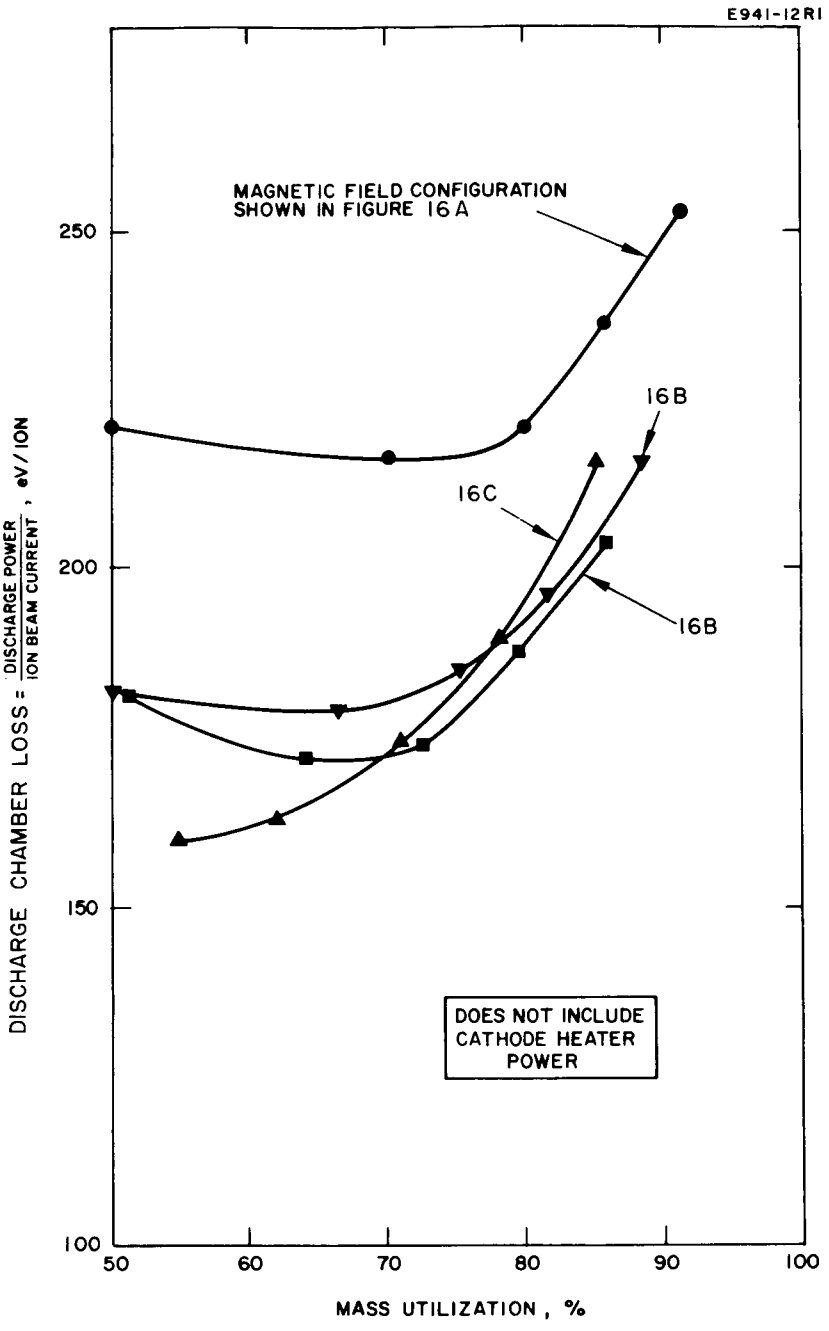

Fig. 15. Performance mapping of discharge efficiency versus mass utilization for several magnetic field configurations. Thruster parameters given in Table IV.

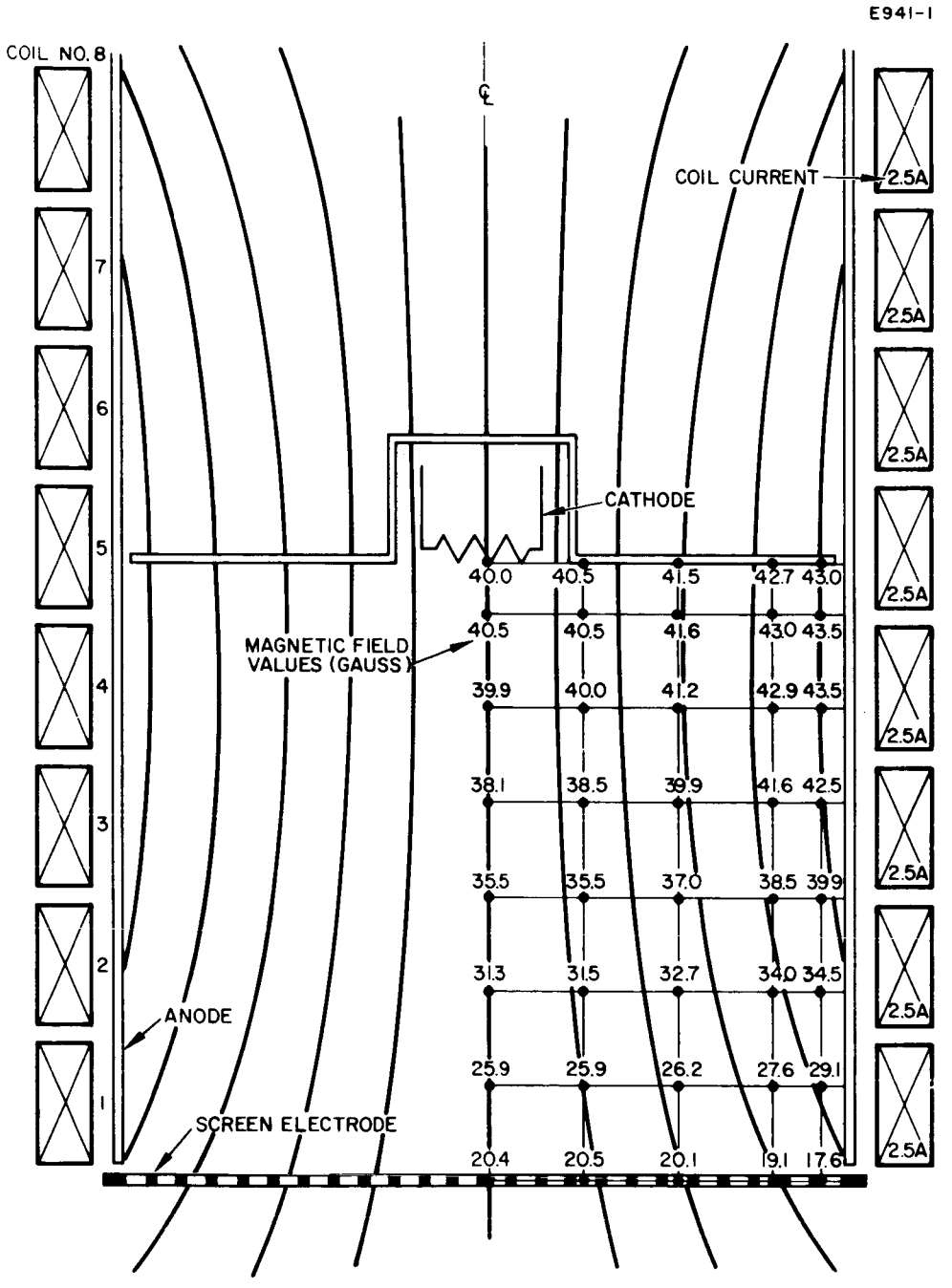

(a) Referred to as 16(a).

Fig. 16. Magnetic field configuration generated in ETI by the magnetic coil currents shown. The field lines are tracings of a powdered iron field map such as that shown in Fig. 10. The magnetic field values shown are the axial component (measured with an axial Hall-effect probe gaussmeter).

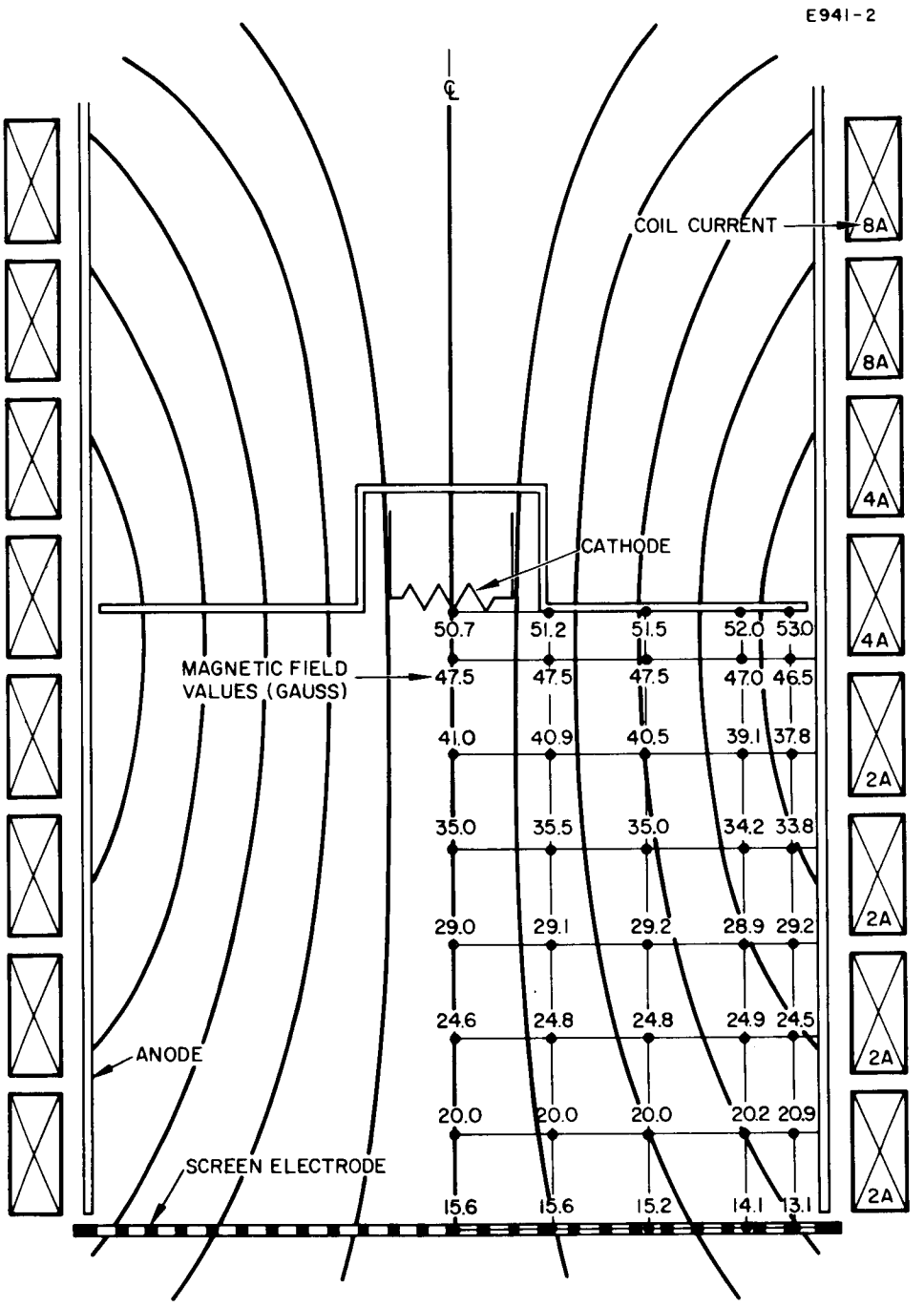

(b) Referred to as 16(b).

Fig. 16. (Cont'd).

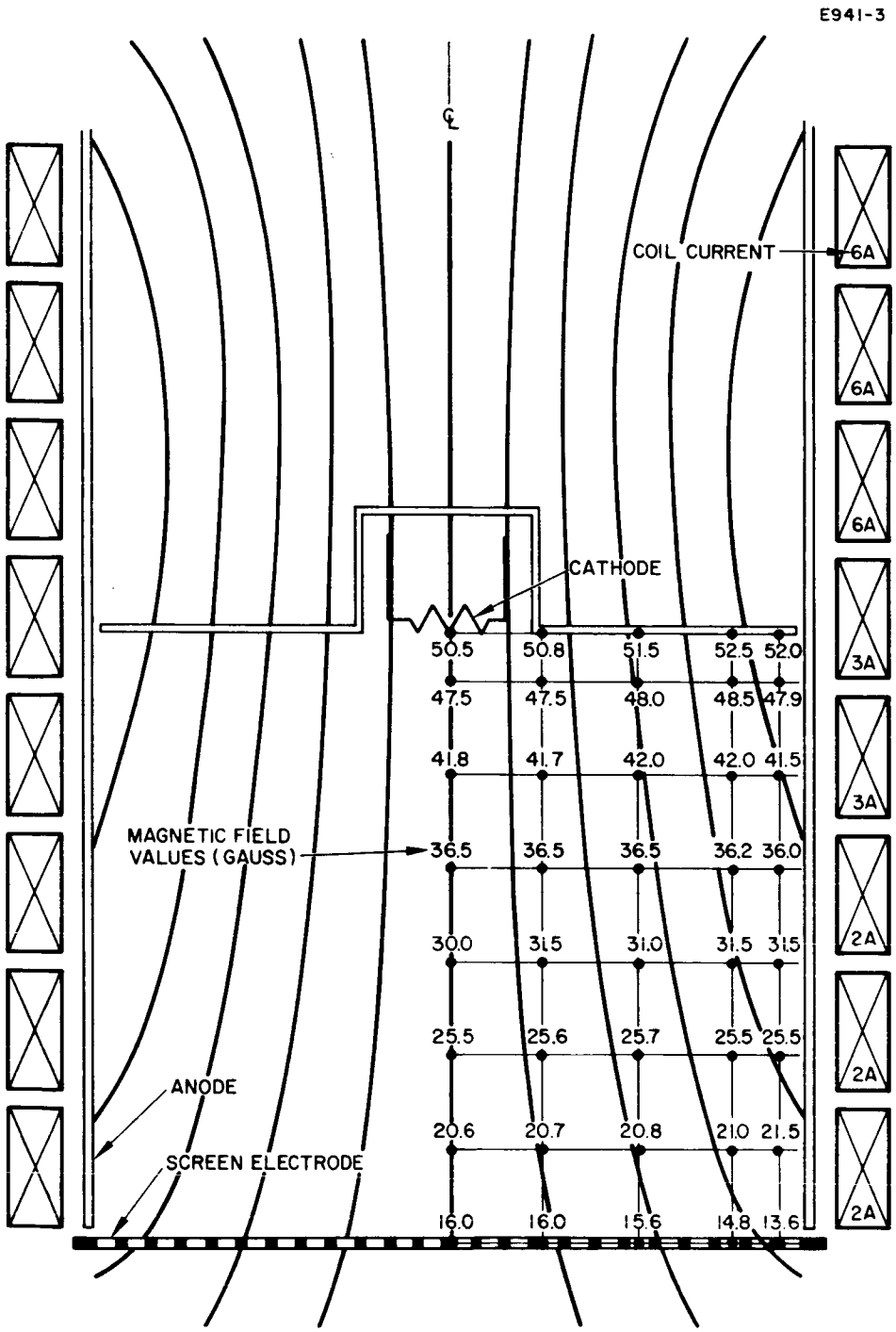

(c) Referred to as 16(c).

Fig. 16. (Cont'd).

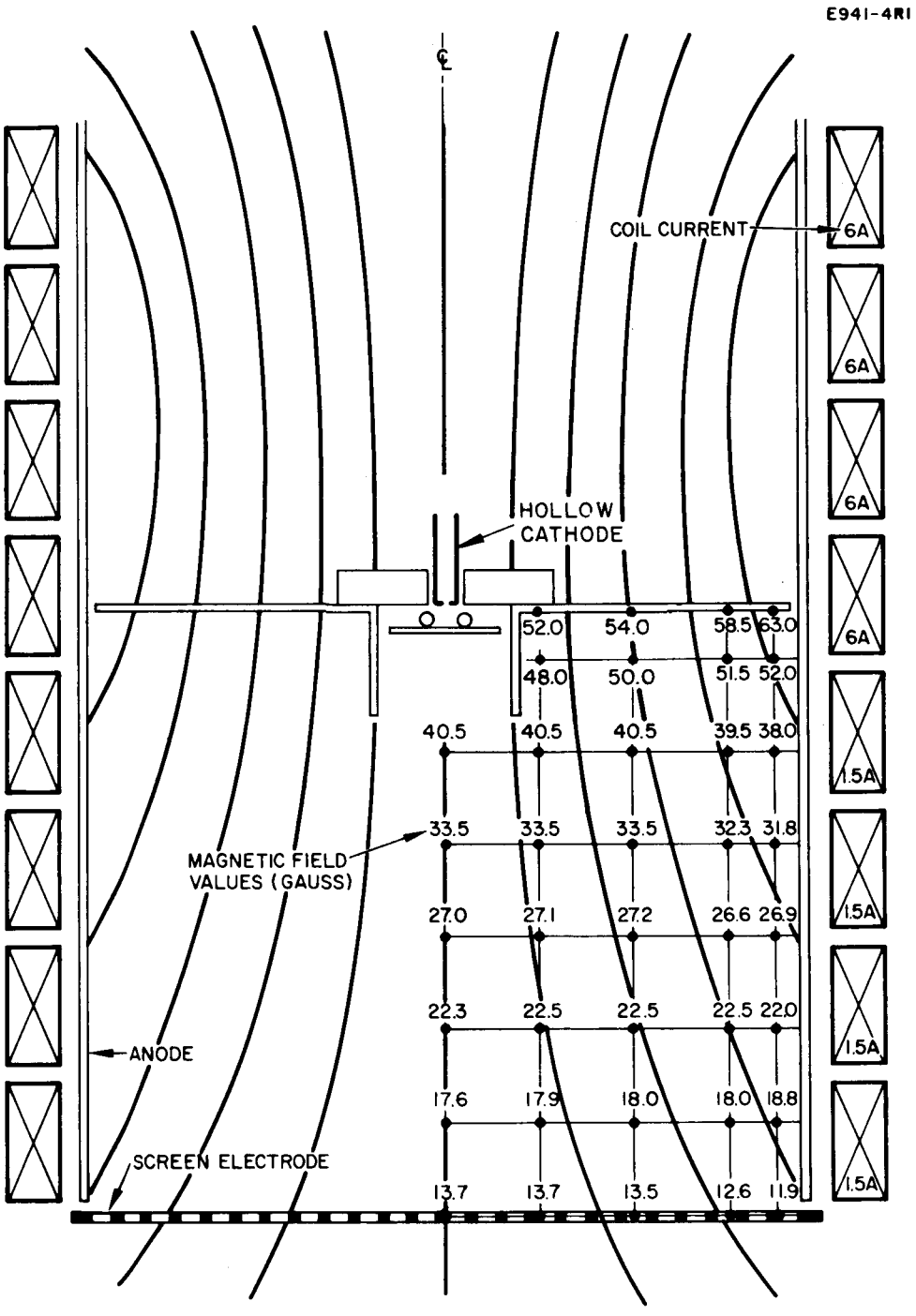

(d) Referred to as 16(d).

Fig. 16. (Cont'd).

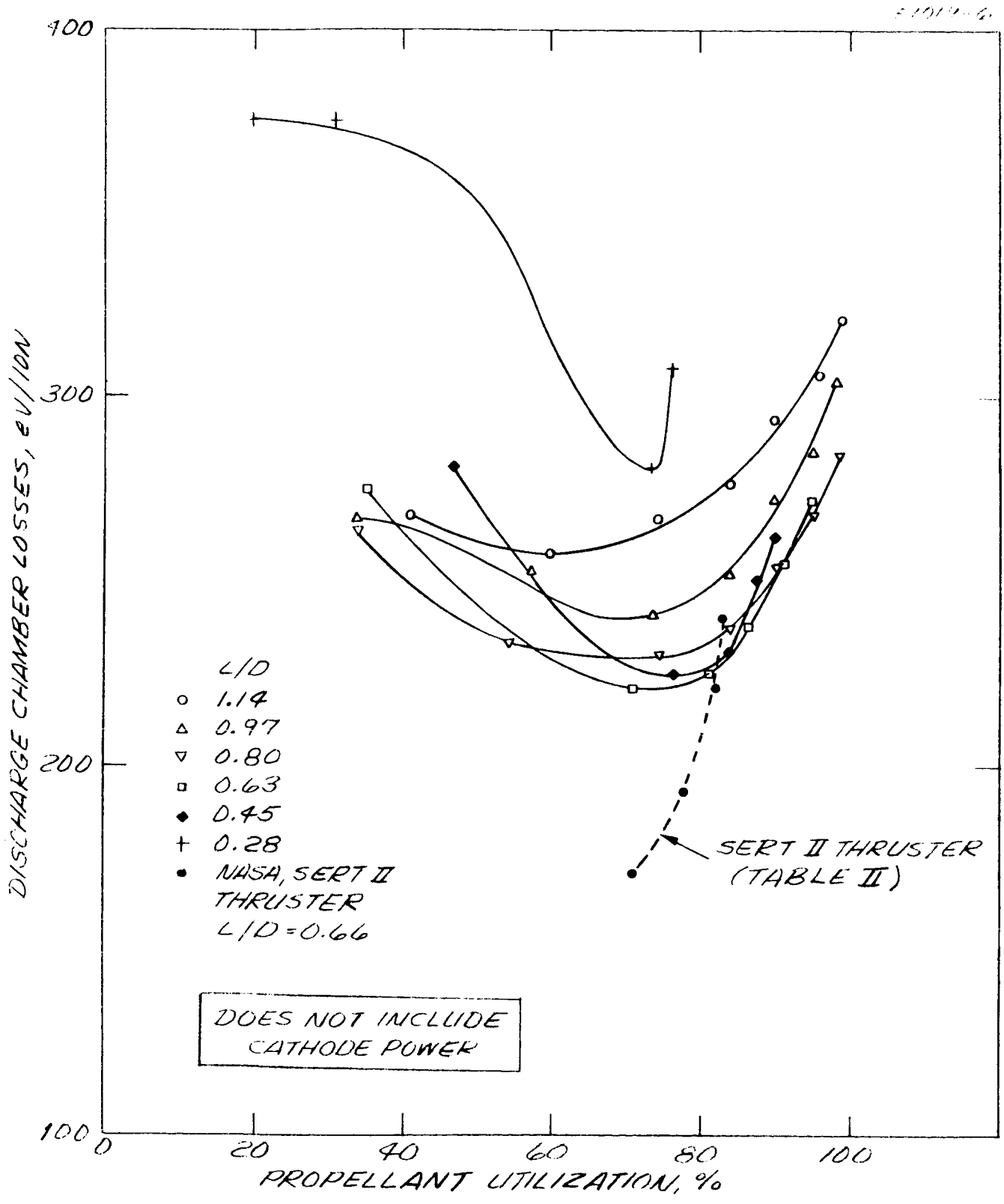

Fig. 17. Performance mappings for a uniform magnetic field configuration (16(a)) for several length-to-diameter ratios. See Table V for thruster parameters.

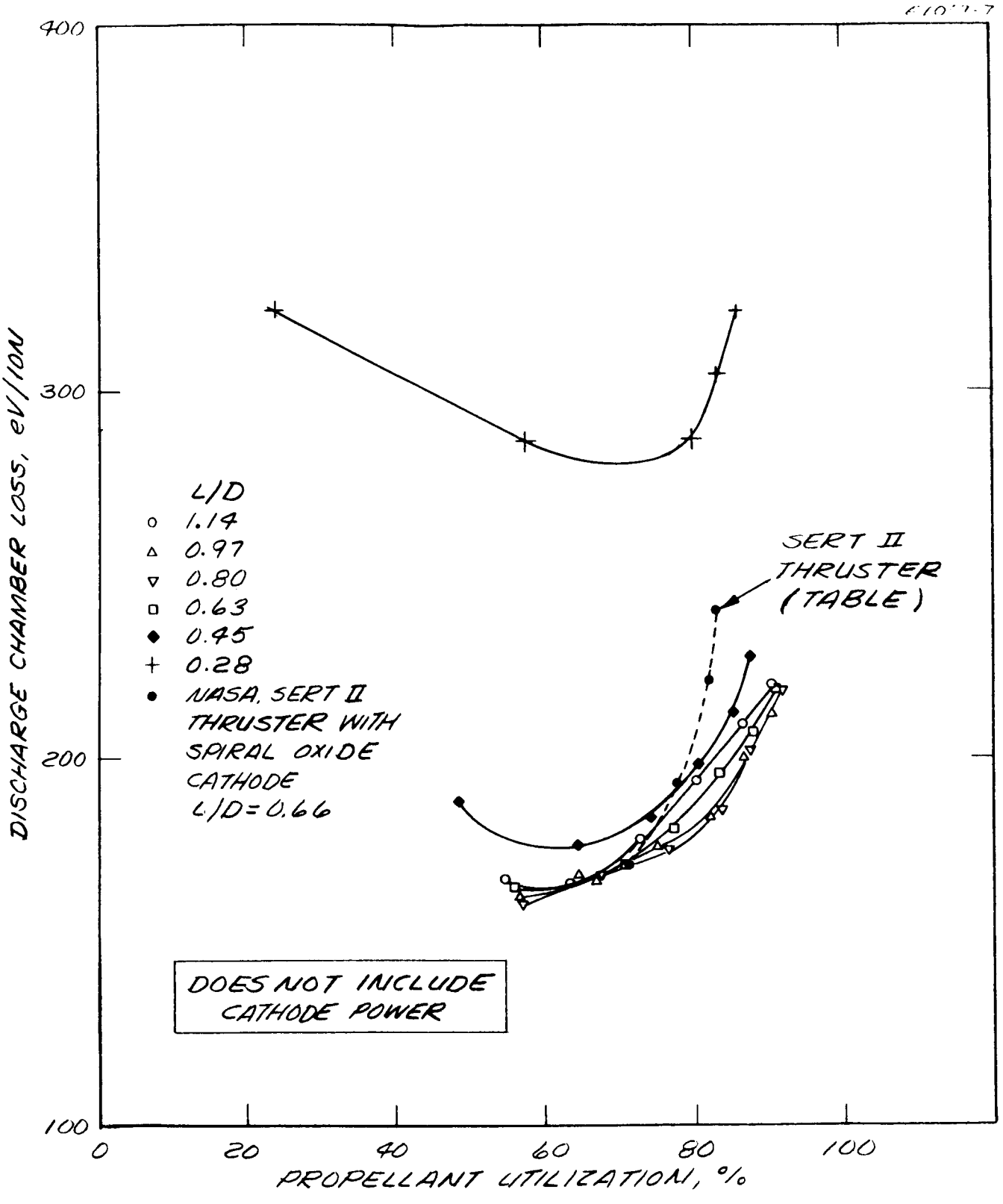

Fig. 18. Performance mappings for a divergent magnetic field configuration (16(d)) for several length-to-diameter ratios. See Table VI for thruster parameters.

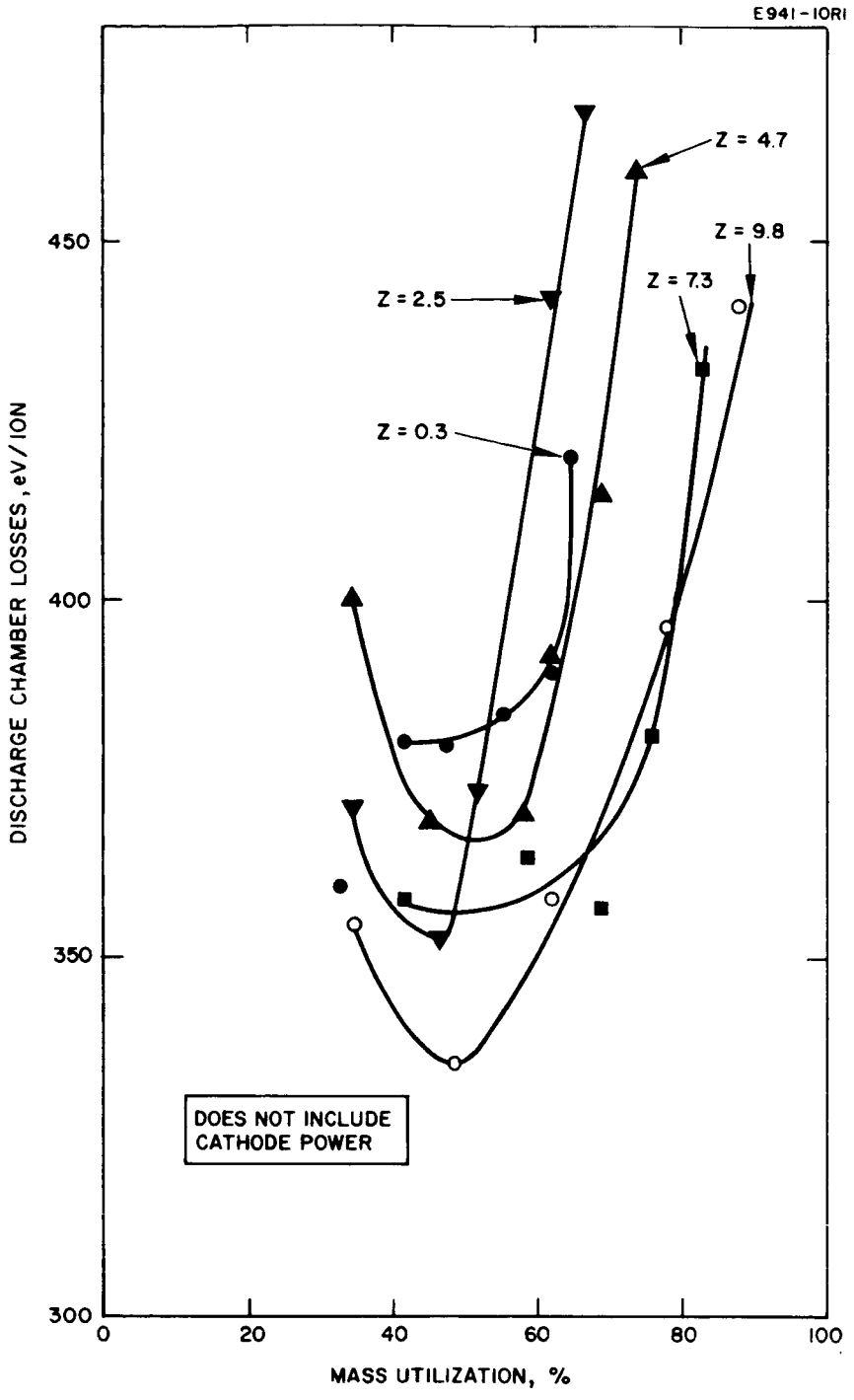

Fig. 19. Performance mapping of discharge efficiency versus mass utilization for variation of cathode position on discharge axis. Z is distance from cathode to screen in centimeters. Thruster parameters are given in Table VIII.

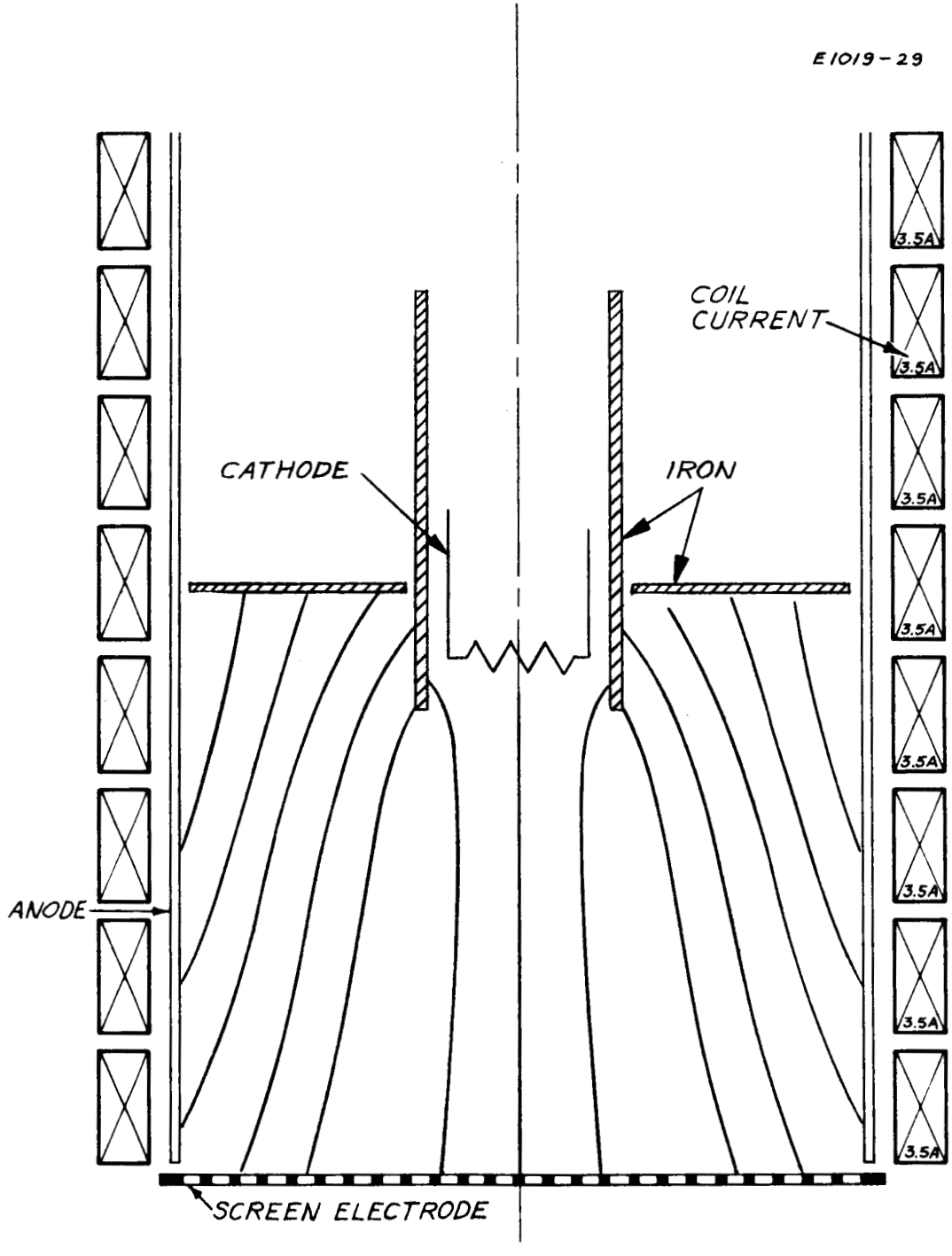

(a) Referred to as 20(a).

Fig. 20. Magnetic field configuration generated in ETI by the coil currents shown. The field lines are tracings of a powdered iron field map such as that shown in Fig. 10. The magnetic field values shown are the axial component (measured with an axial Hall effect probe gaussmeter).

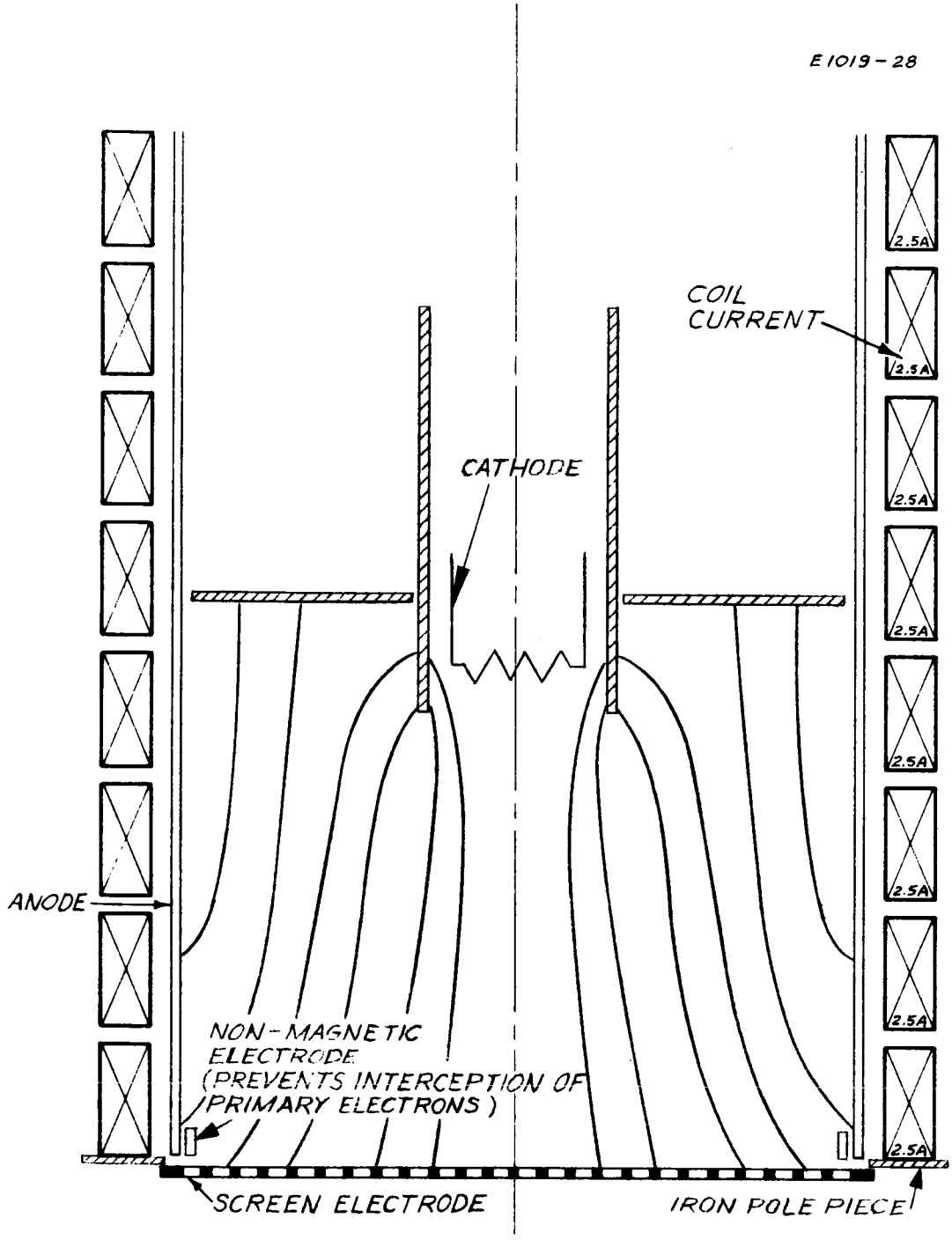

(b) Referred to as 20(b).

Fig. 20. (Cont'd).

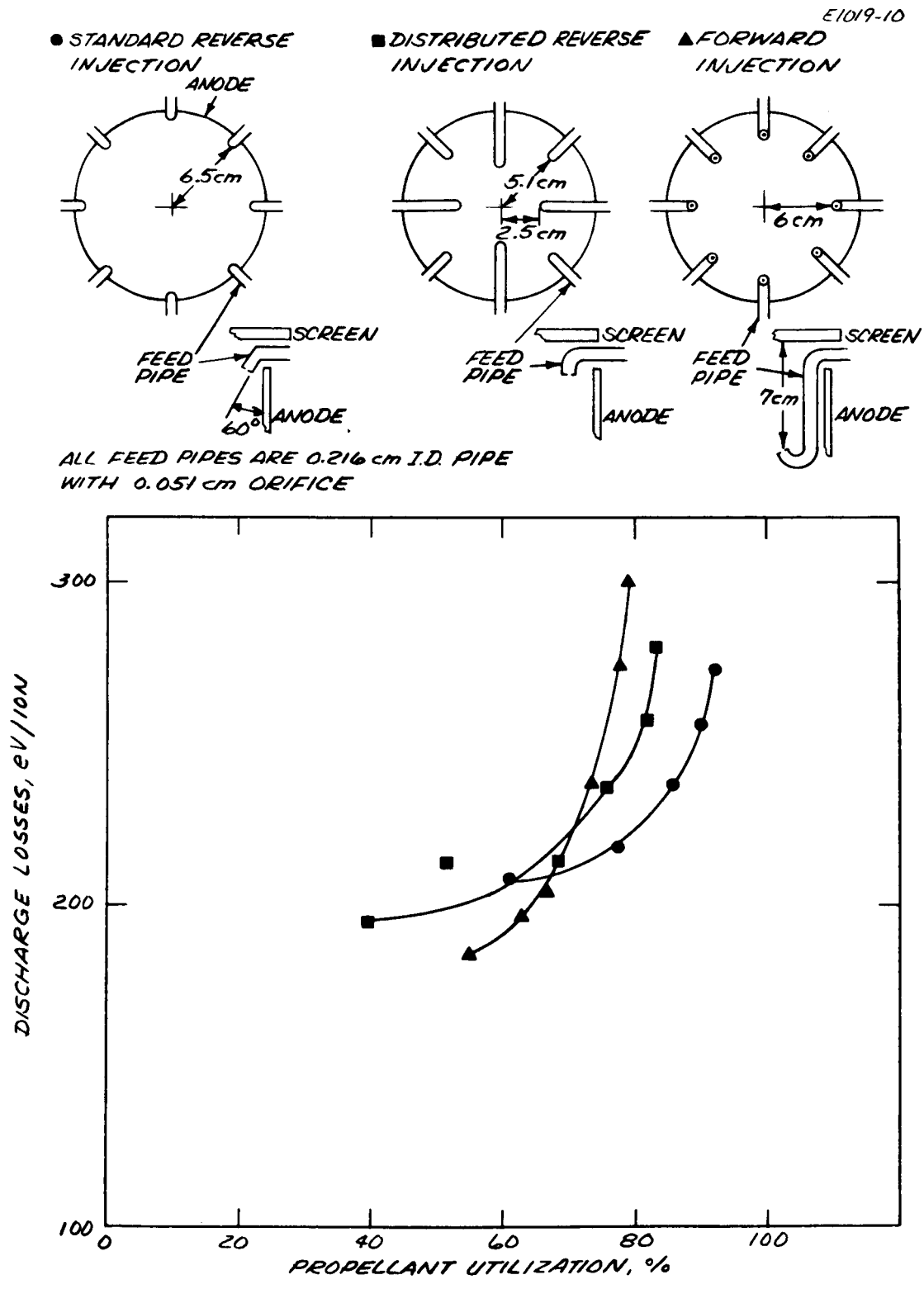

Fig. 21. Performance mappings for several methods of propellant injection in a relatively uniform magnetic configuration. All mappings for magnetic configuration 20A. See Table IX for thruster parameters.

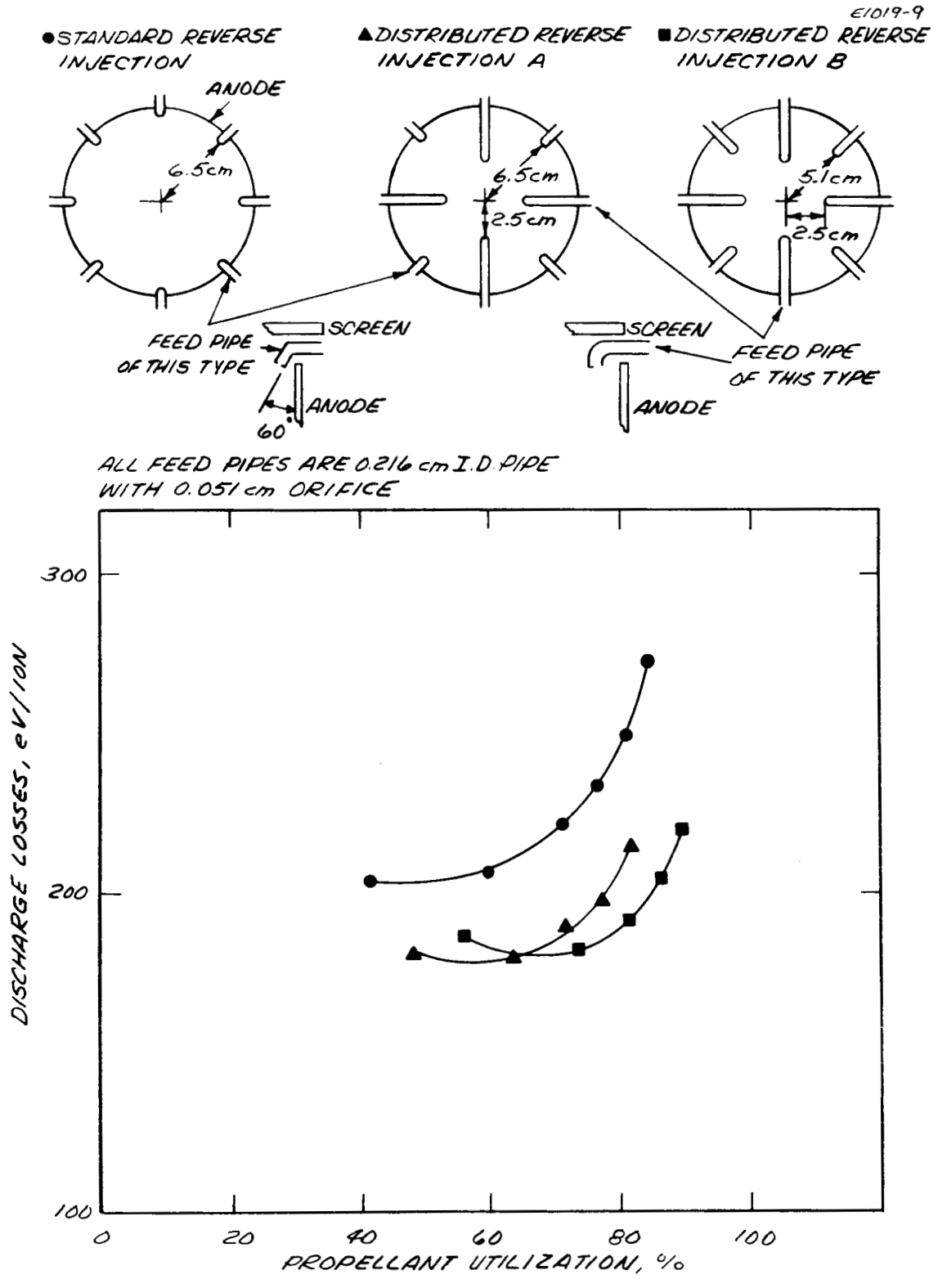

Fig. 22. Performance mappings for several methods of propellant injection in a relatively divergent magnetic configuration. All mappings for magnetic configuration 20B. See Table X for thruster parameters.

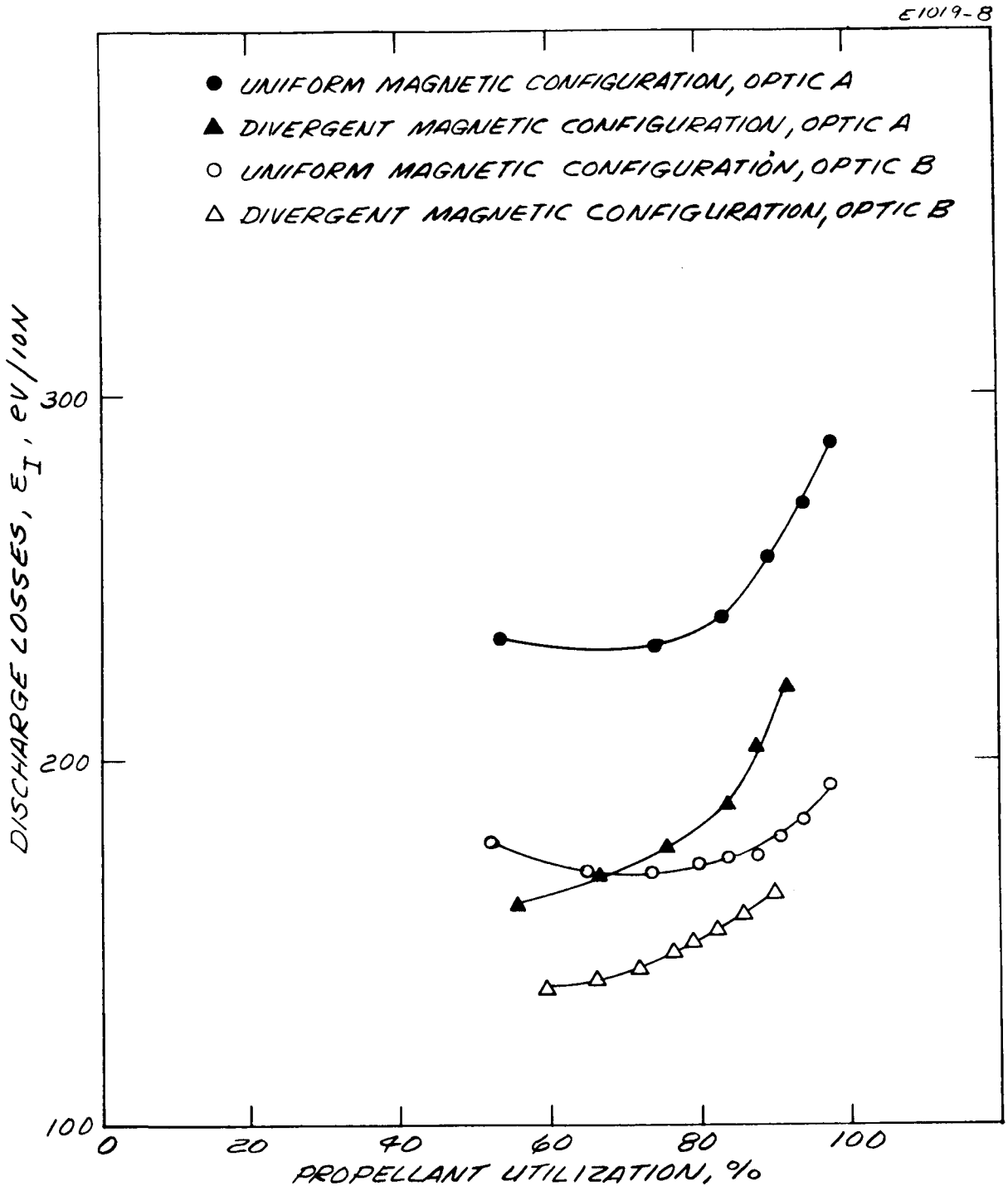

Fig. 23. Comparison of performance mappings for uniform and divergent magnetic configurations with extraction optics A (48% transparency) and optics B (71% transparency). See Table XI for thruster parameters.

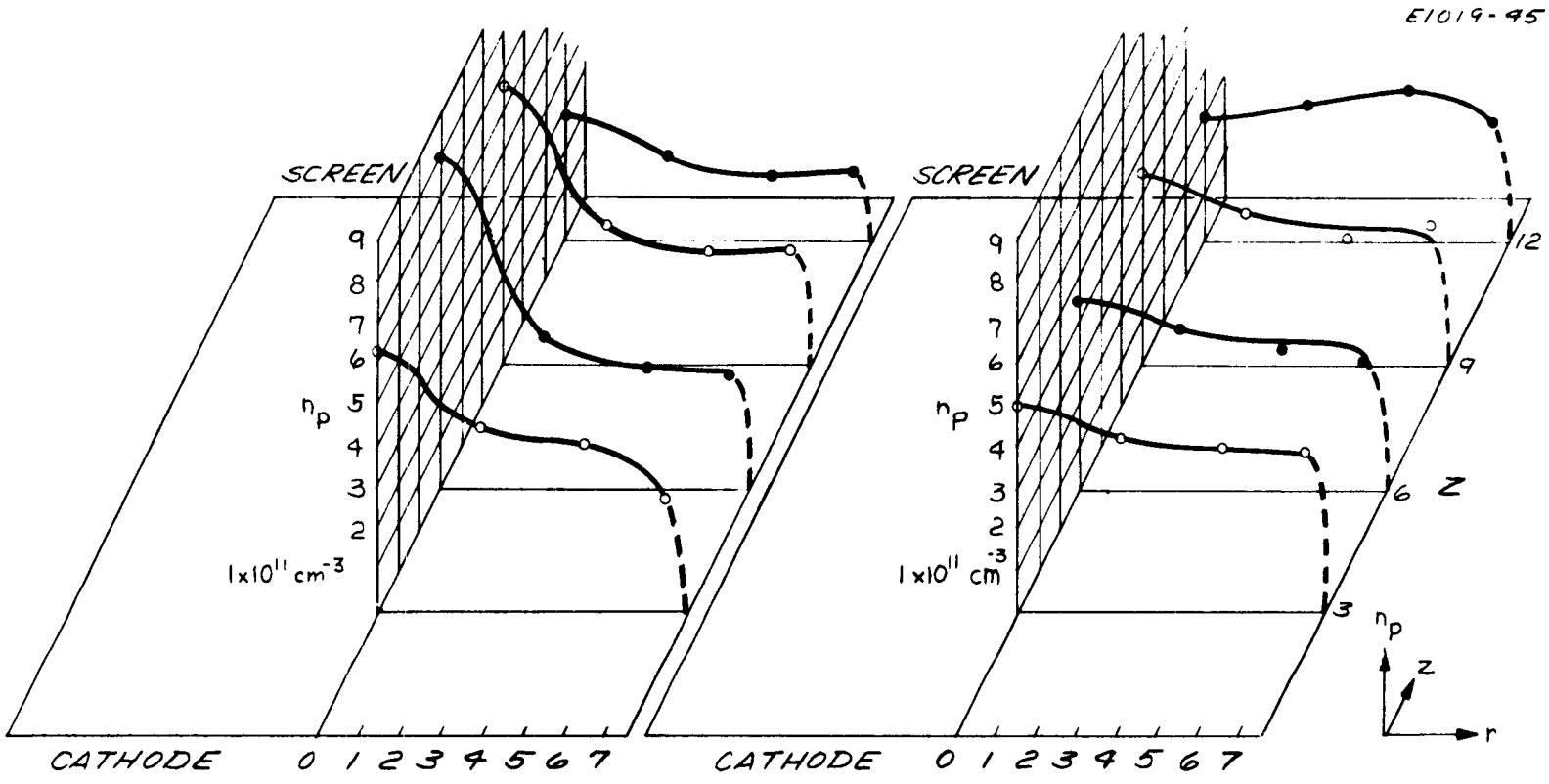

(2A) UNIFORM MAGNETIC CONFIGURATION

DISCHARGE VOLTAGE	40.2 V
DISCHARGE CURRENT	1.15 A
ION BEAM CURRENT	203 mA
DRAIN CURRENT	0.9 mA
EQUIVALENT NEUTRAL CURRENT	265 mA
PROPELLANT UTILIZATION	76 %
DISCHARGE LOSS	228 eV/ION

(2D) DIVERGENT MAGNETIC CONFIGURATION

DISCHARGE VOLTAGE	41.2 V
DISCHARGE CURRENT	1.03 A
ION BEAM CURRENT	240 mA
DRAIN CURRENT	0.8 mA
EQUIVALENT NEUTRAL CURRENT	265 mA
PROPELLANT UTILIZATION	77 %
DISCHARGE LOSS	208 eV/ION

Fig. 24. Plasma density distributions in uniform and divergent magnetic configurations (optics A, 48% transparency). Probe data obtained with Probe 1 shown in Fig. 5. Data given in Table XII.

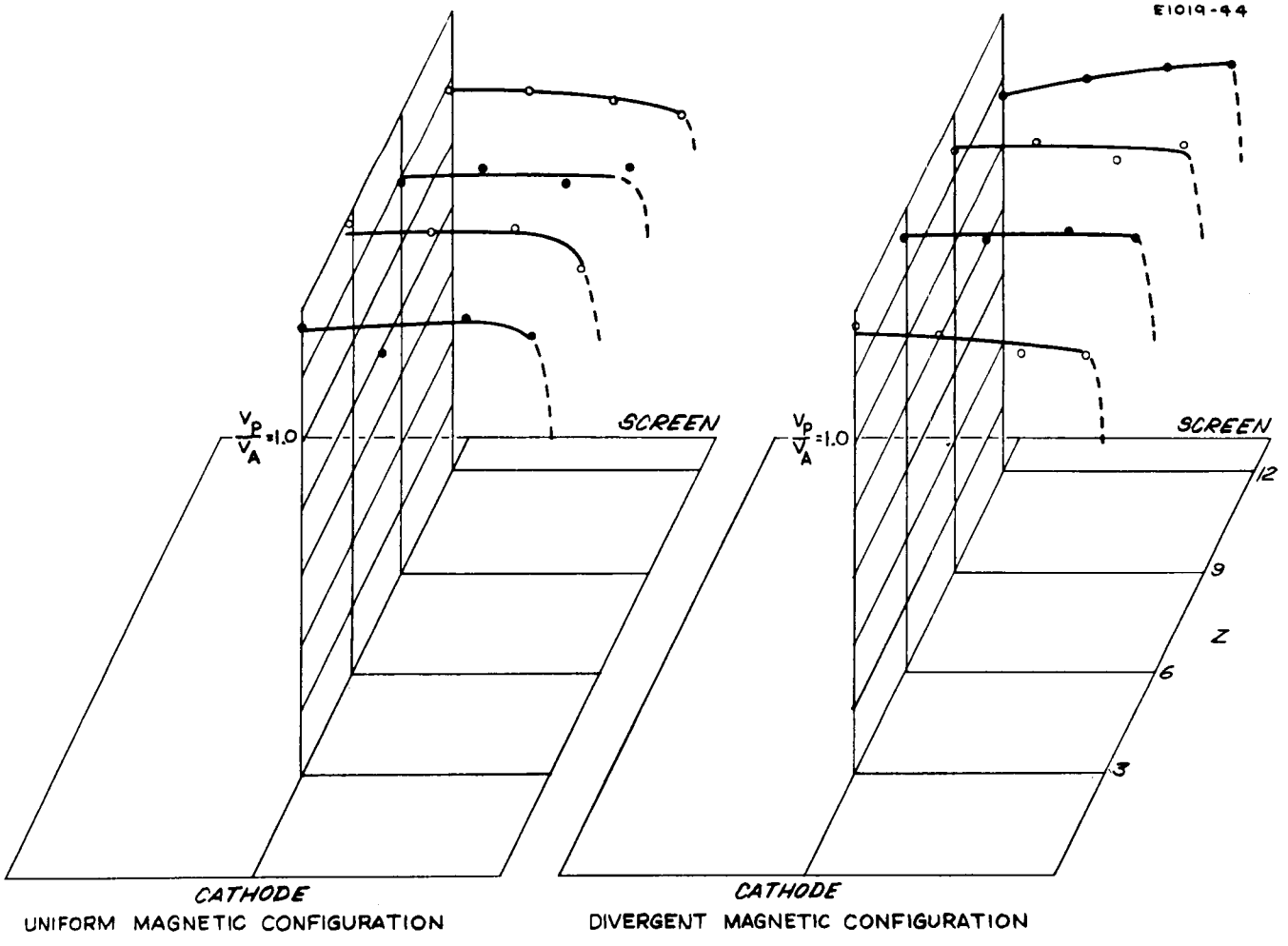

Fig. 25. Normalized plasma potential distribution for a uniform and a divergent magnetic configuration. (Same operating conditions as given in Fig. 24.)

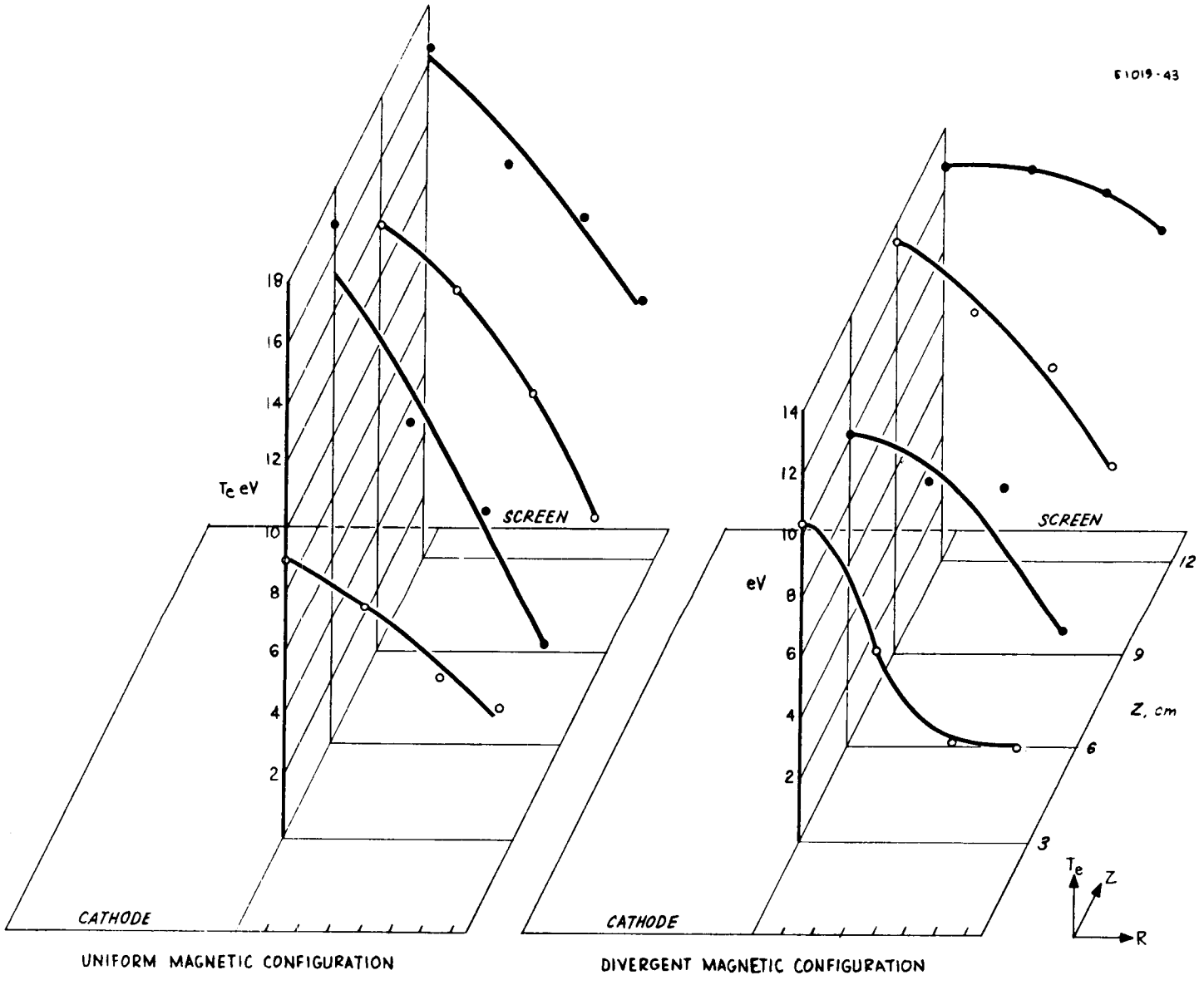

Fig. 26. Spatial distribution of "Maxwellian" plasma electron temperature for a uniform and a divergent magnetic configuration with optics A (48% transparency).

E1019-12

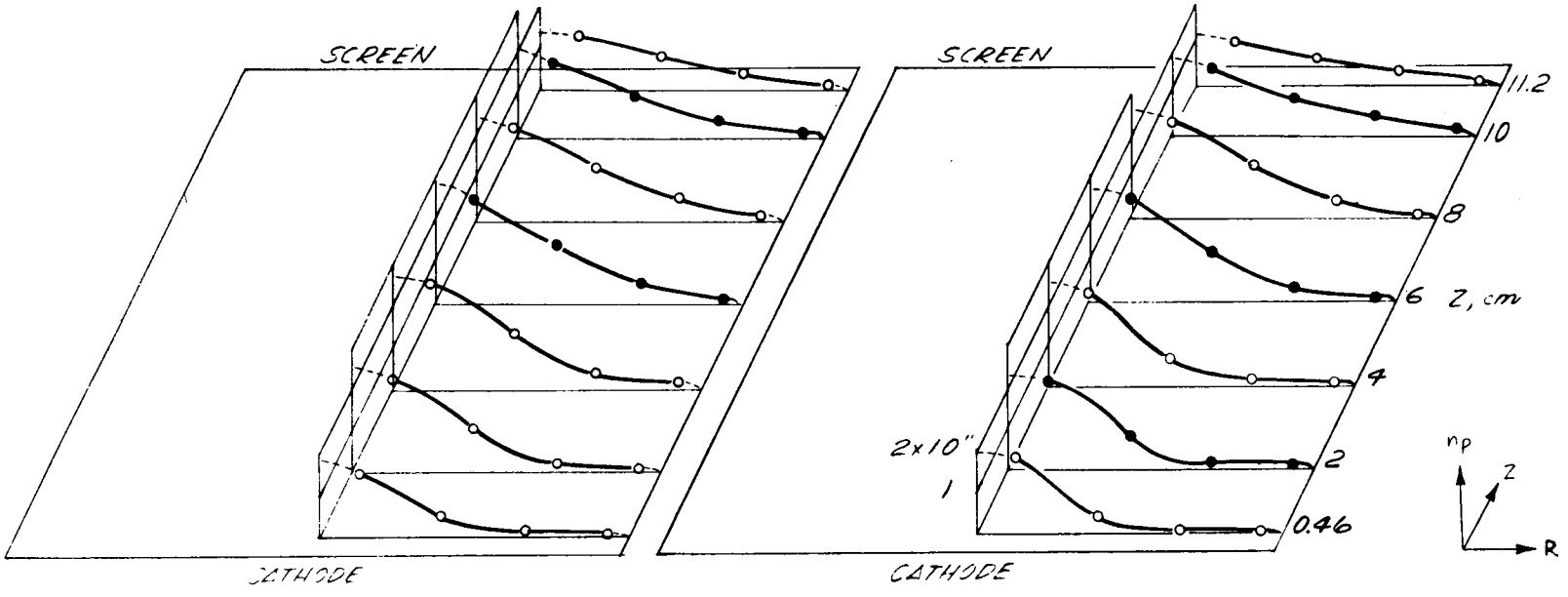

UNIFORM MAGNETIC CONFIGURATION (16A)

DISCHARGE VOLTAGE	40.4 V
DISCHARGE CURRENT	1.03 A
ION BEAM CURRENT	268 mA
DRAIN CURRENT	1.3 mA
EQUIVALENT NEUTRAL CURRENT	330 mA
PROPELLANT UTILIZATION	81 %
DISCHARGE LOSS	155 eV/ION

DIVERGENT MAGNETIC CONFIGURATION (16D)

DISCHARGE VOLTAGE	40 V
DISCHARGE CURRENT	1.22 A
ION BEAM CURRENT	281 mA
DRAIN CURRENT	1.1 mA
EQUIVALENT NEUTRAL CURRENT	330 mA
PROPELLANT UTILIZATION	88 %
DISCHARGE LOSS	173 eV/ION

Fig. 27. Plasma density distributions in a uniform and a divergent magnetic configuration for optics B (71% transparency). Probe data obtained with probe 2 shown in Fig. 5. These data are given in Table XIII.

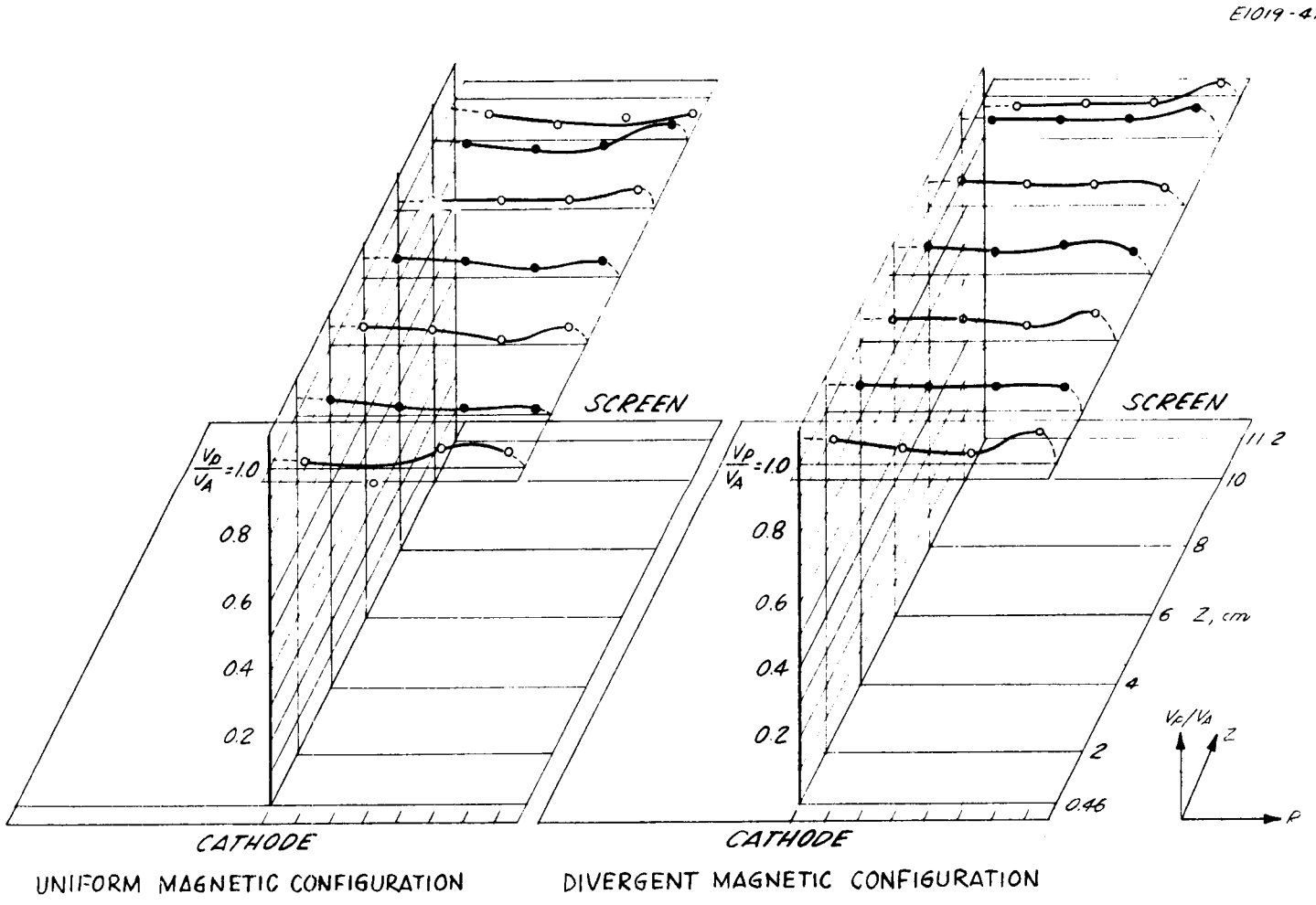

Fig. 28. Normalized plasma potential distribution for a uniform and a divergent magnetic configuration with optics B (71% transparency).

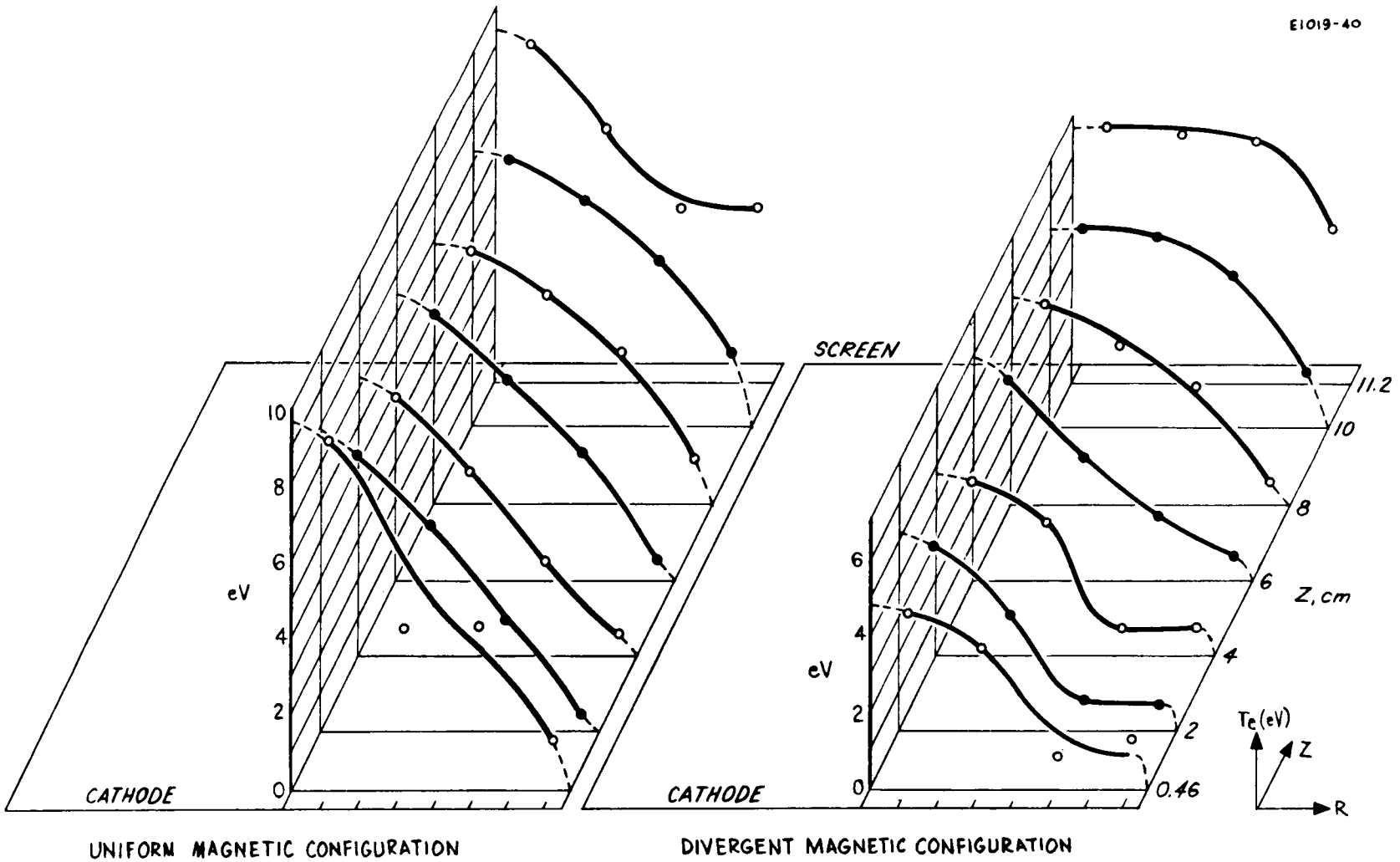

Fig. 29. Spatial distribution of Maxwellian plasma electron temperature for a uniform and a divergent magnetic configuration with optics B (71% transparency).

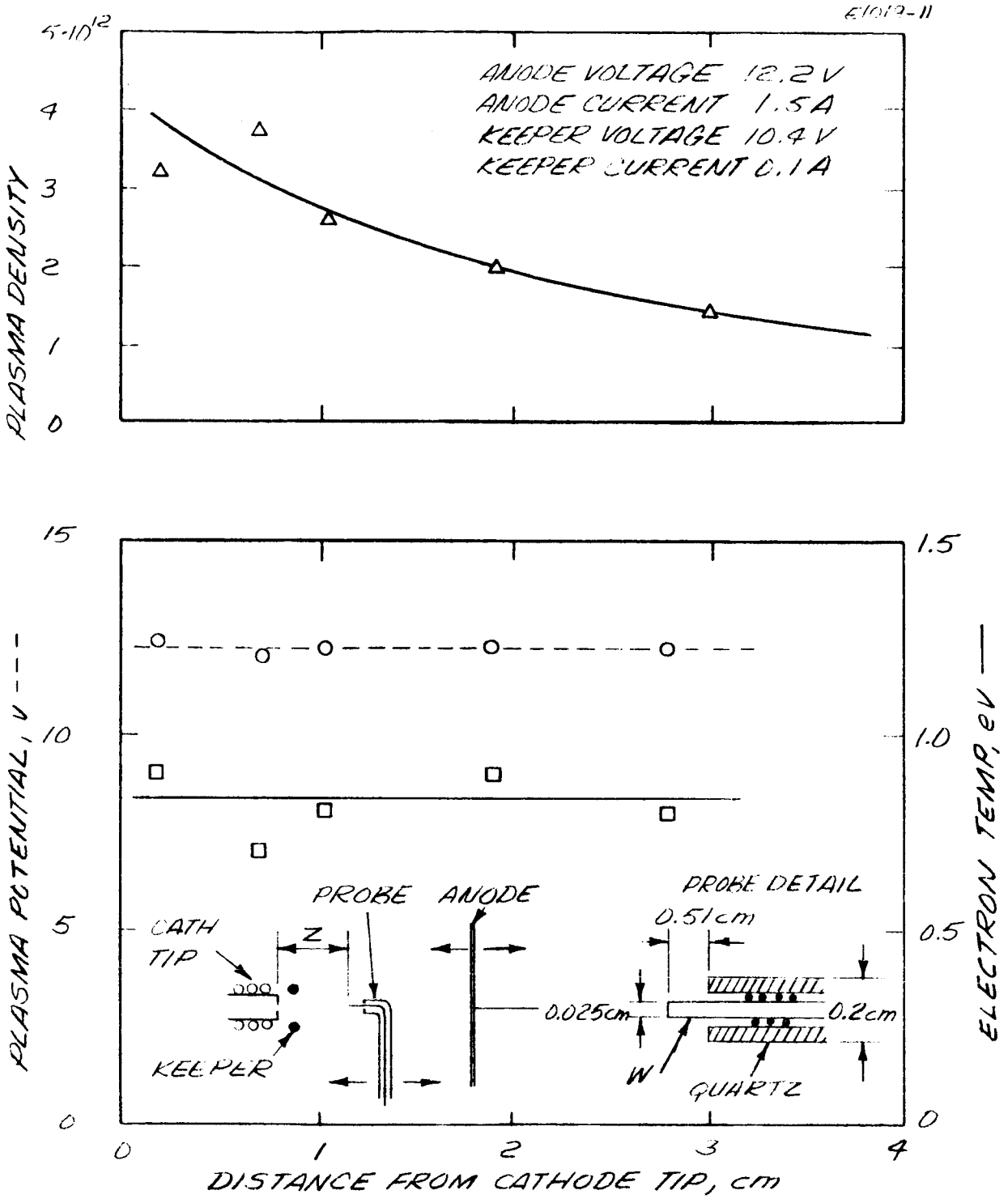

Fig. 30. Hollow cathode plasma properties (in the spot mode) as a function of distance from the cathode tip.

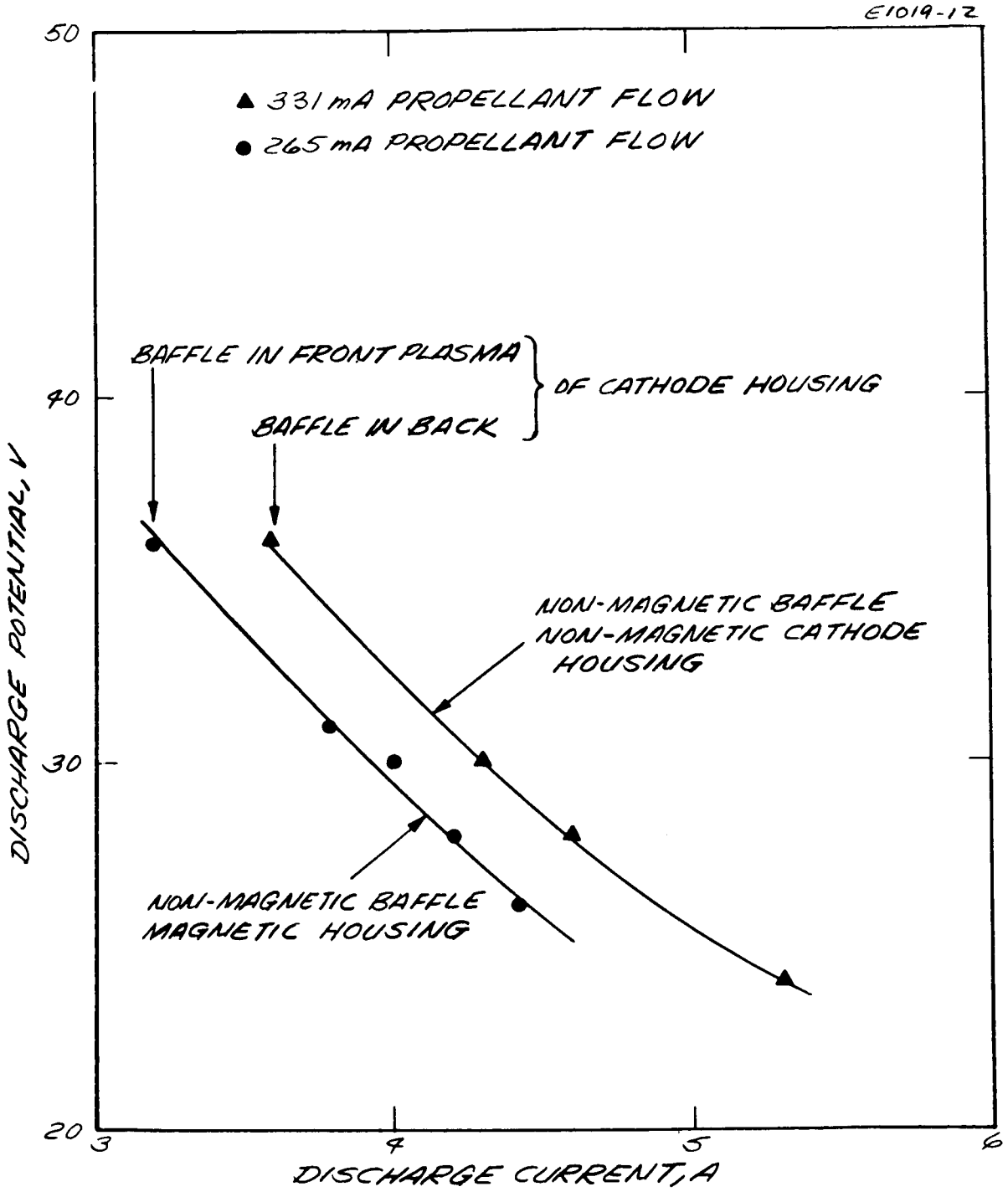

Fig. 31. Discharge potential of the experimental hollow cathode thruster as a function of discharge current for constant discharge power. The discharge current is varied through changes in baffle position.

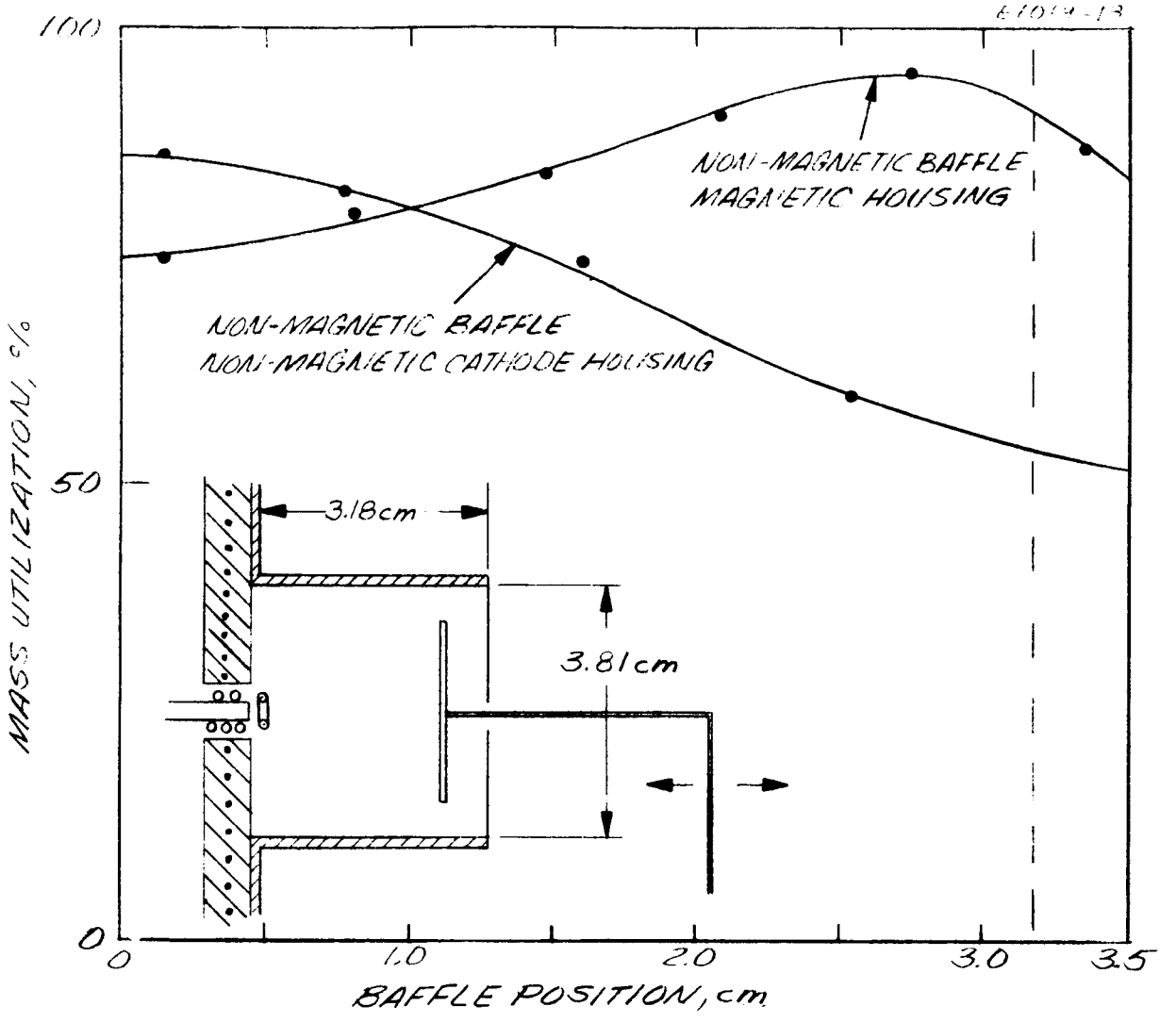

Fig. 32. Mass utilization (or "normalized" ion beam current) as a function of baffle position, obtained with the experimental hollow cathode thruster.

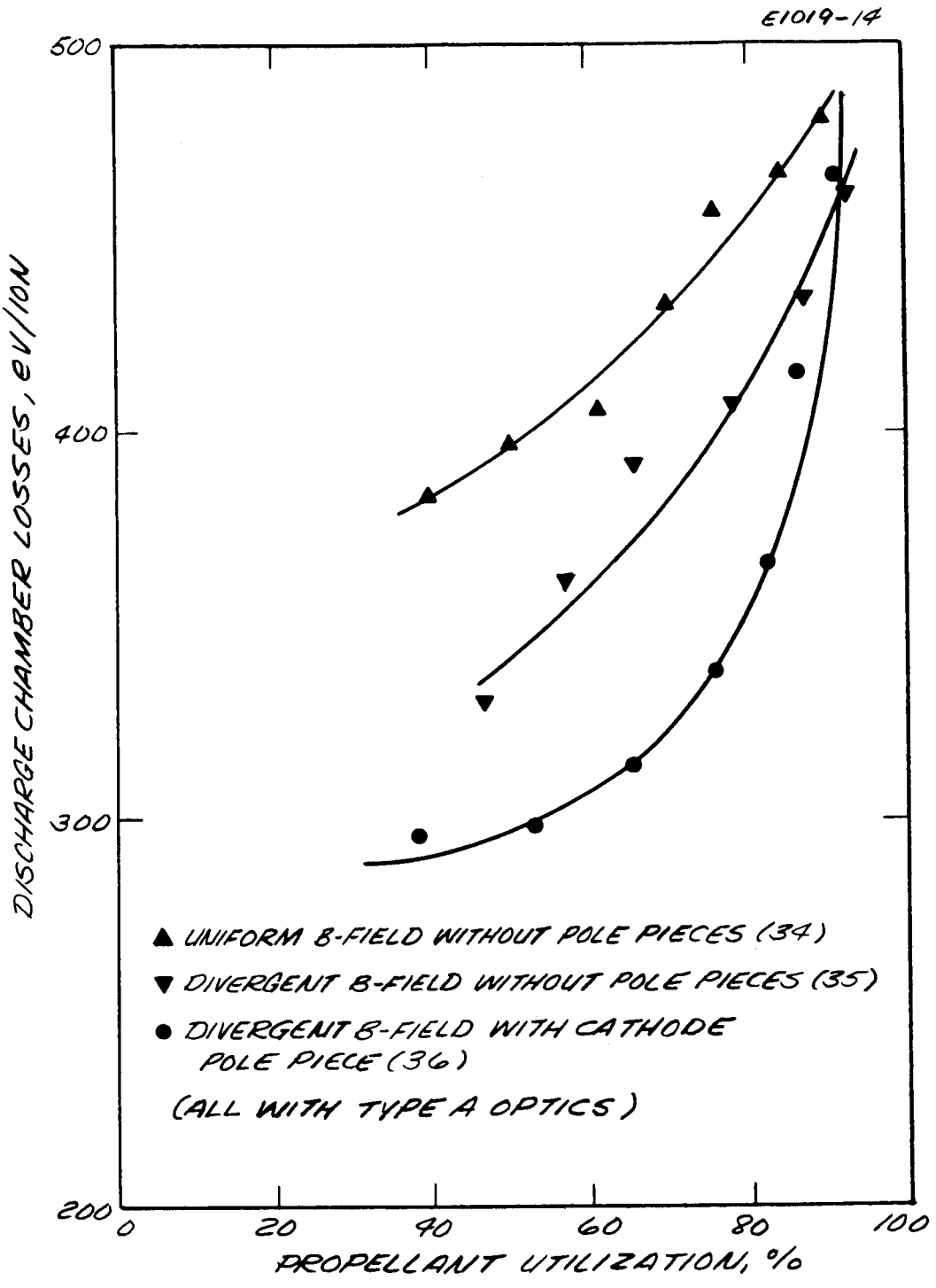

Fig. 33. Performance data of the experimental hollow cathode thruster for different magnetic configurations. (Magnetic field tracings are shown in Figs. 34, 35, and 36. Thruster parameters are given in Table XIV.)

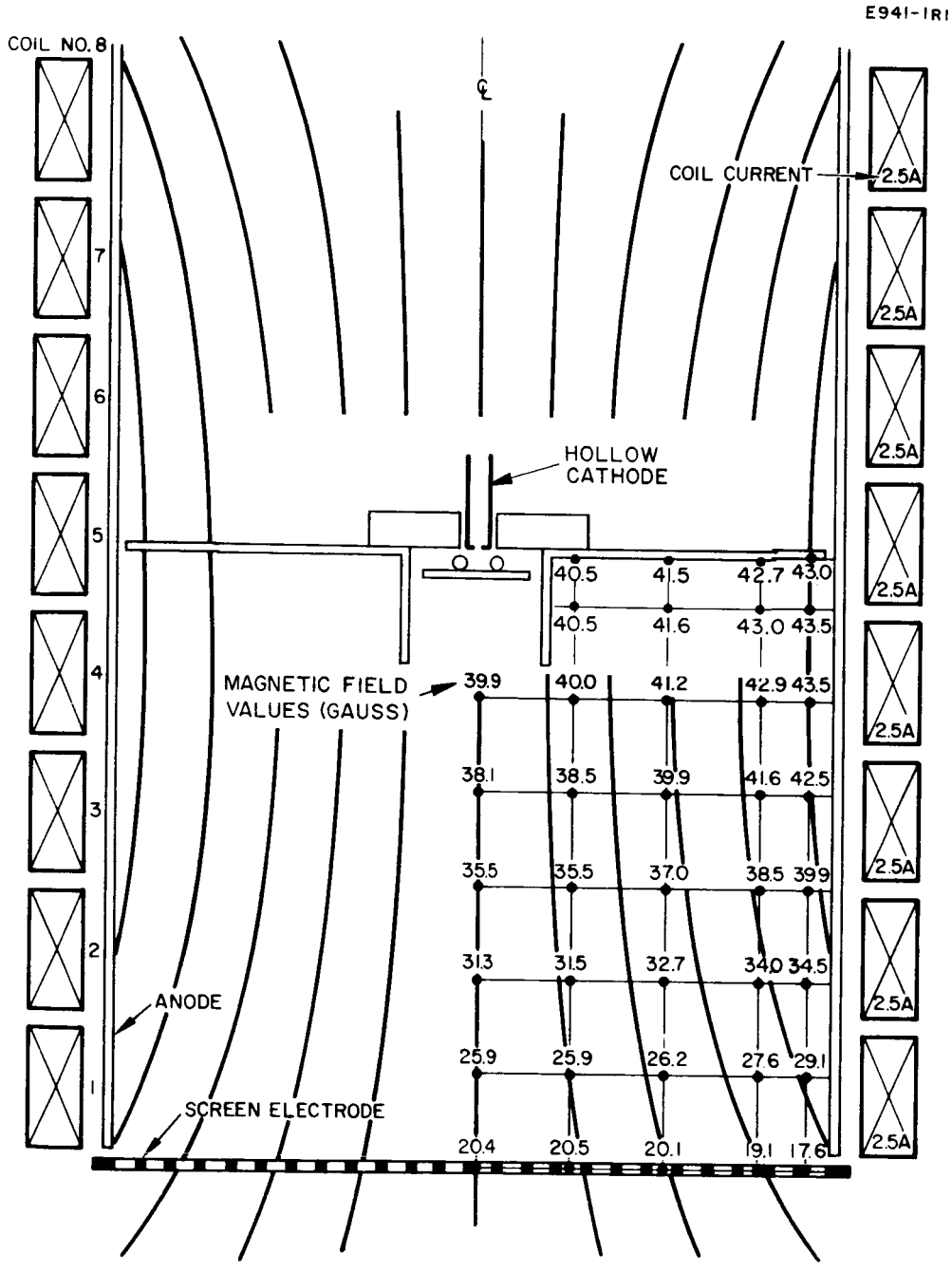

Fig. 34. Magnetic field configuration 34.

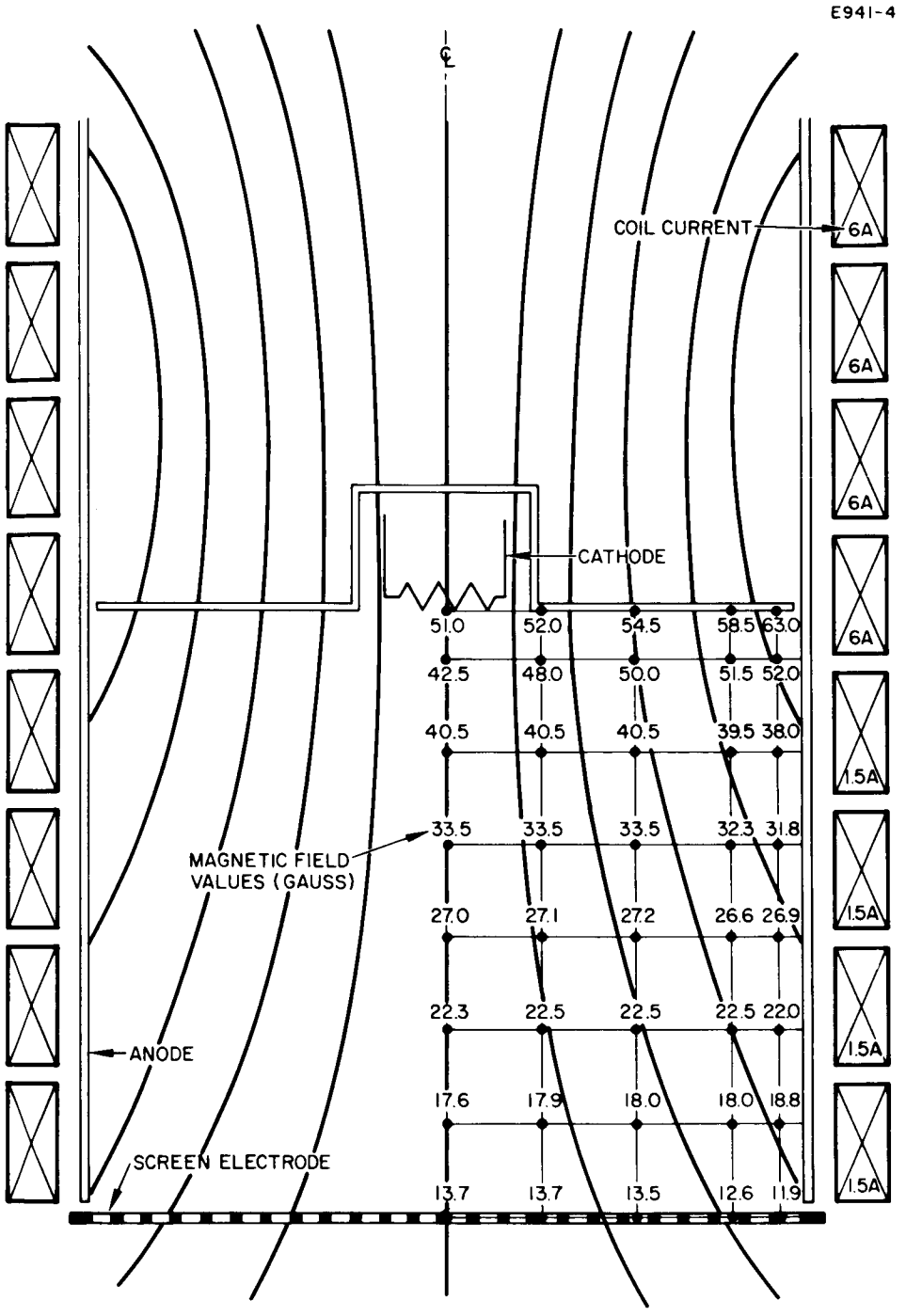

Fig. 35. Magnetic field configuration 35.

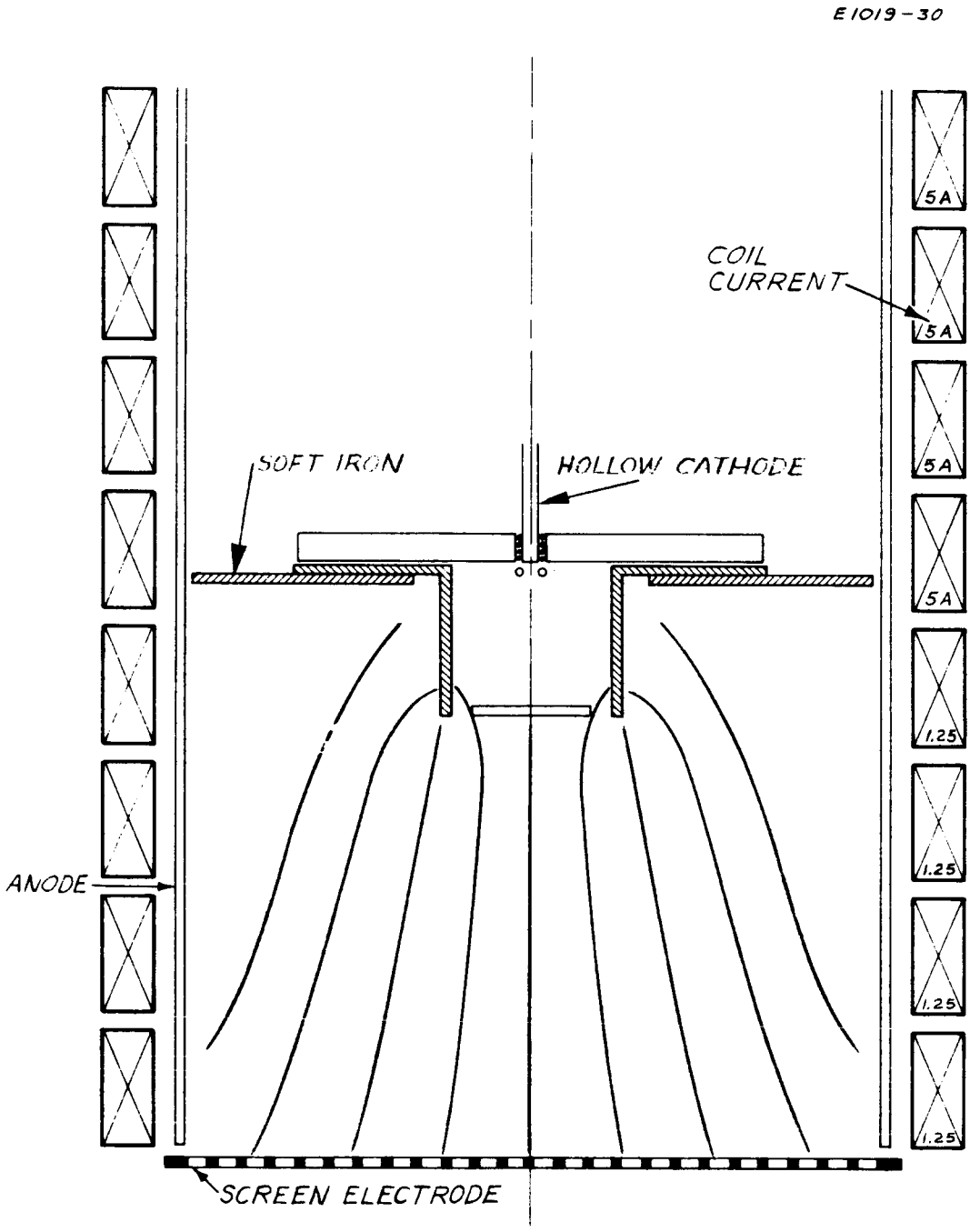

Fig. 36. Magnetic field configuration 36.

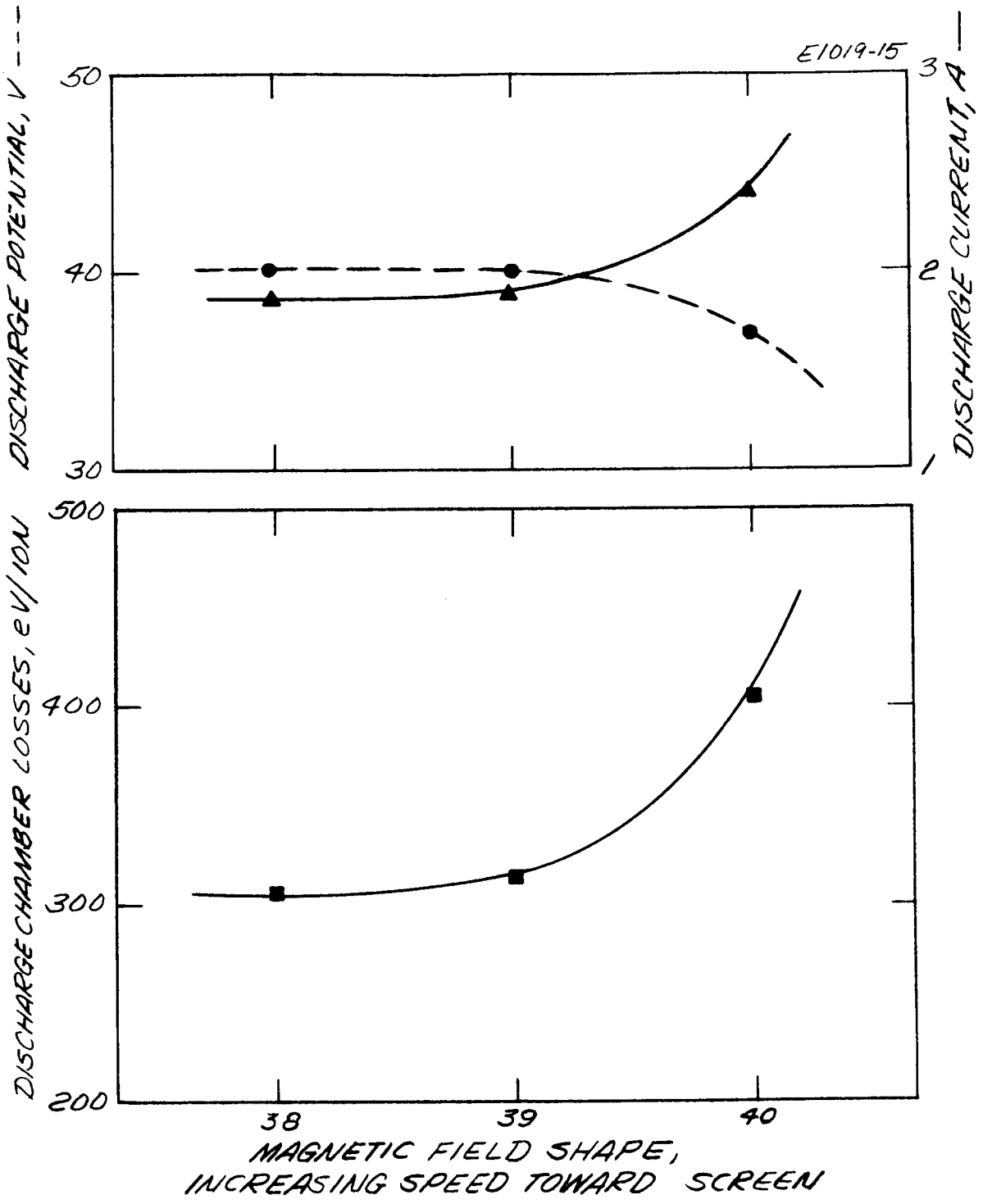

Fig. 37. Performance data of the experimental hollow cathode thruster as a function of the magnetic field spread toward the screen electrode. (The different magnetic configurations are shown in Figs. 38, 39, and 40.)

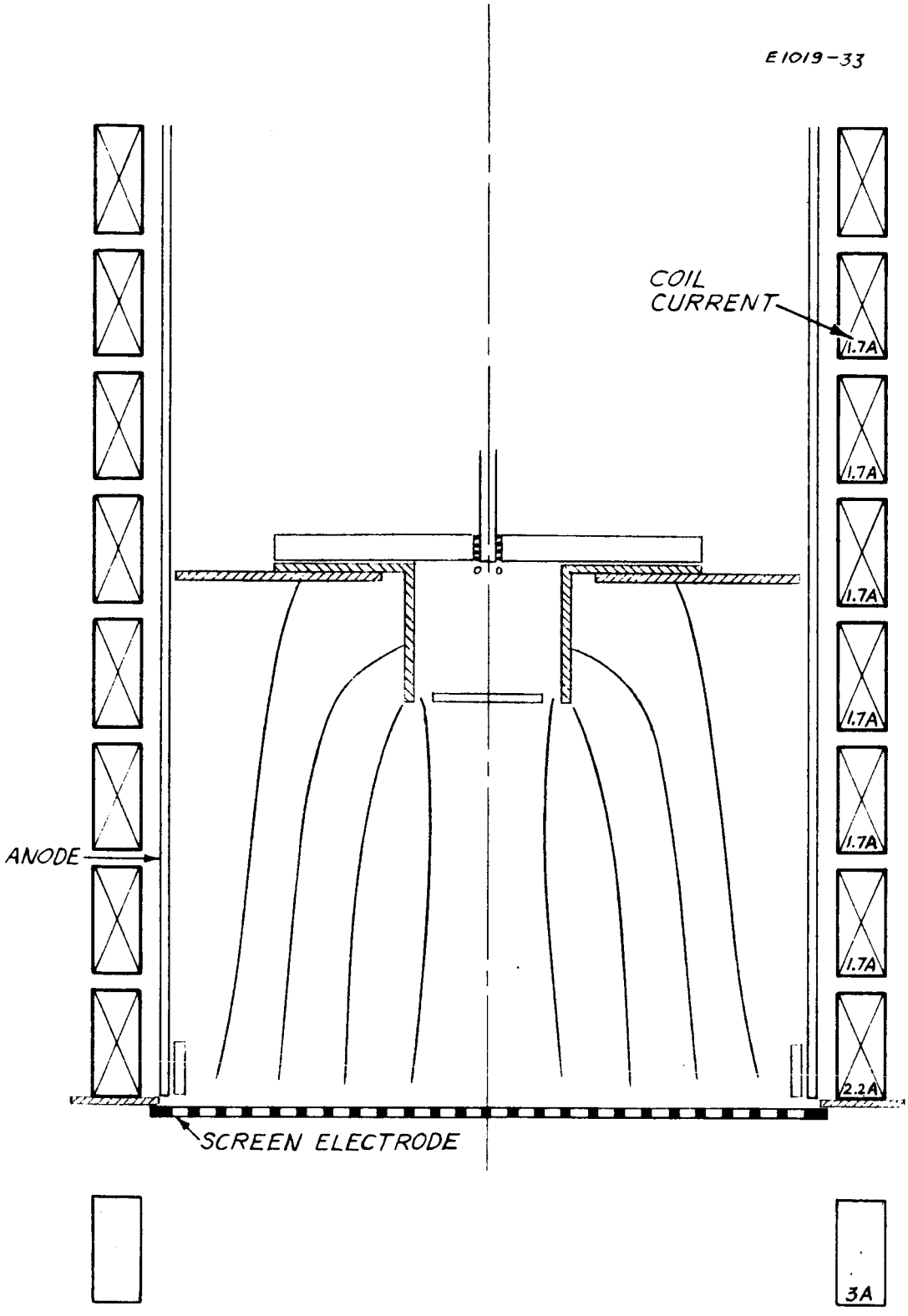

Fig. 38. Magnetic field configuration 38.

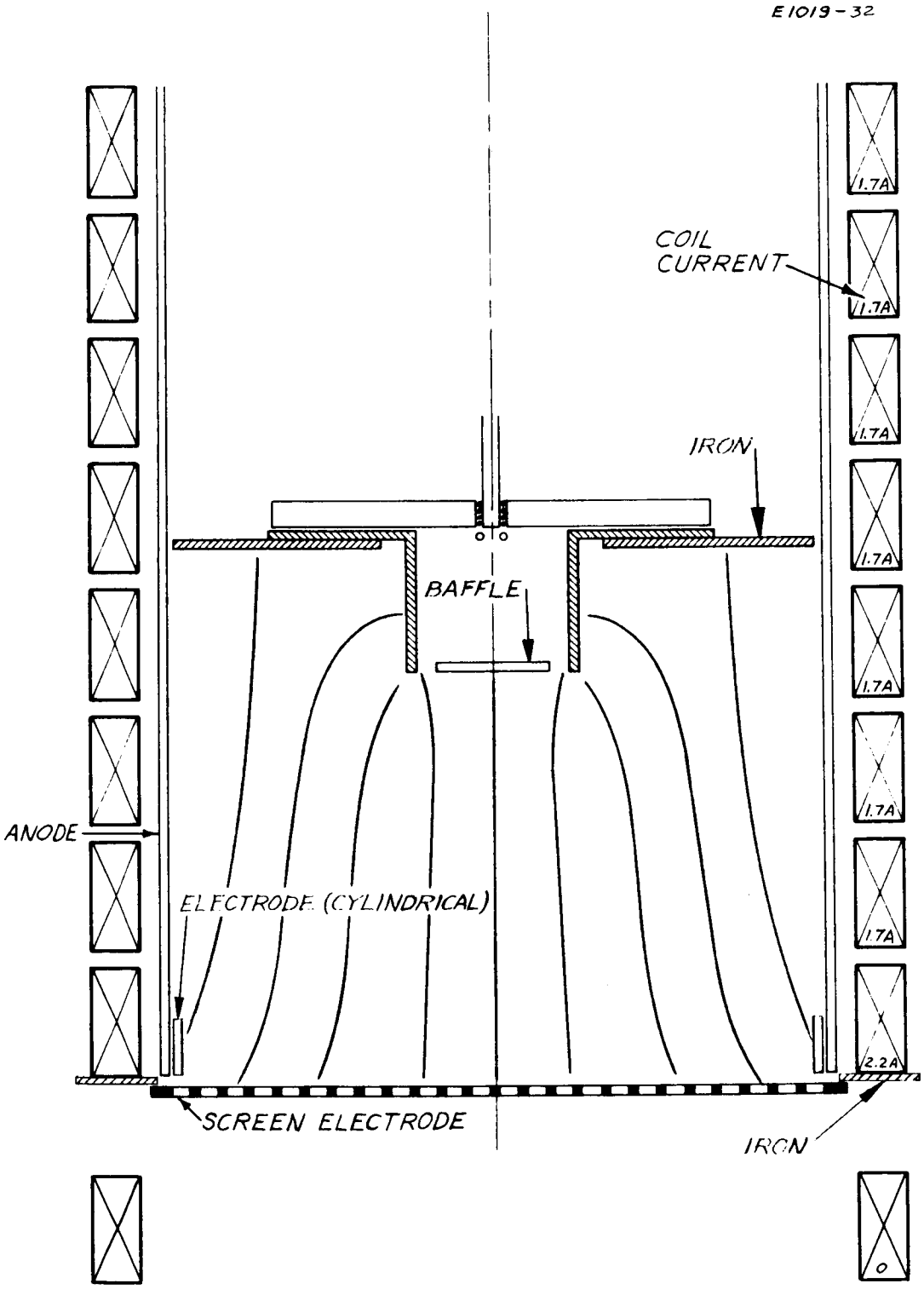

Fig. 39. Magnetic field configuration 39.

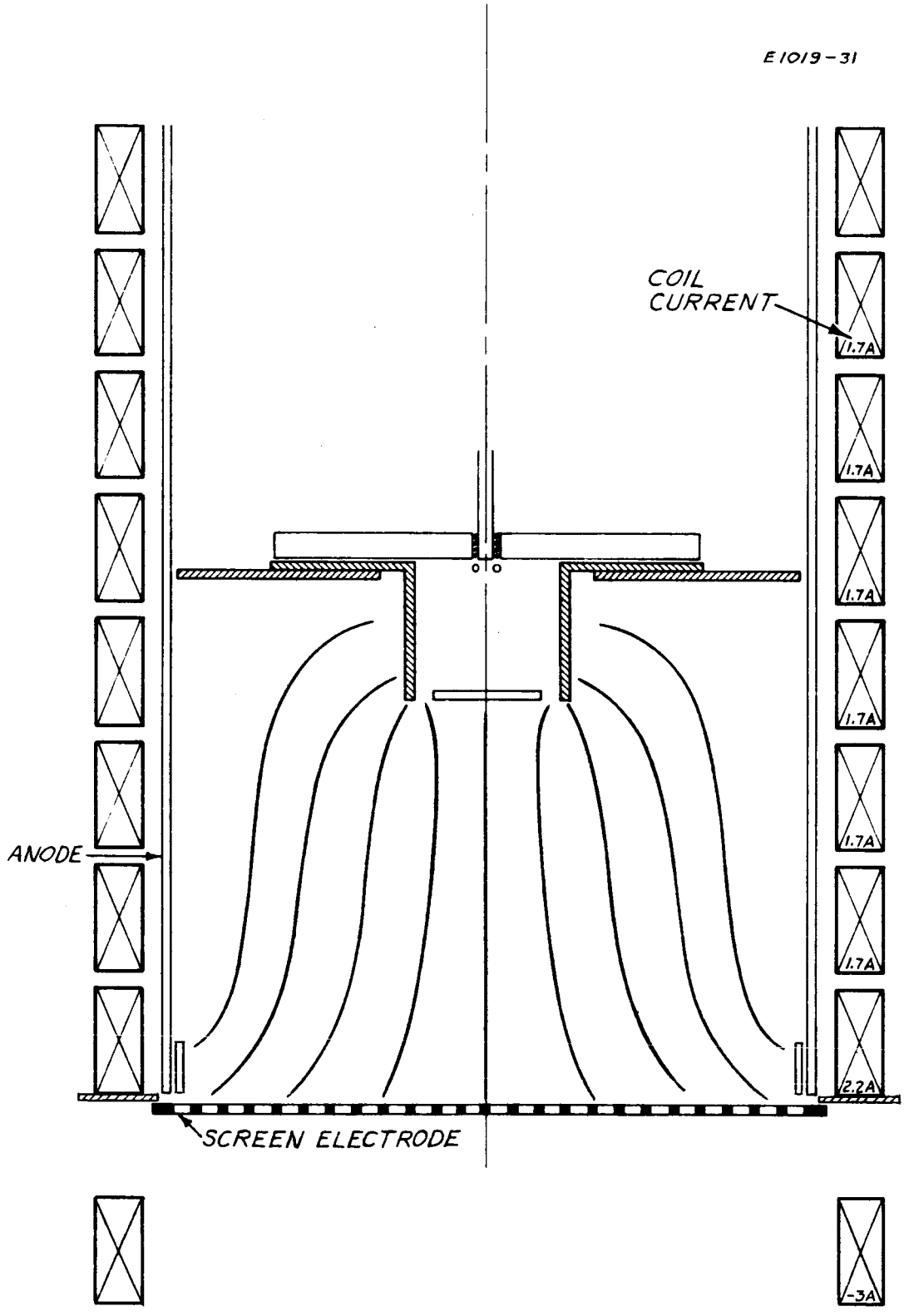

Fig. 40. Magnetic field configuration 40.

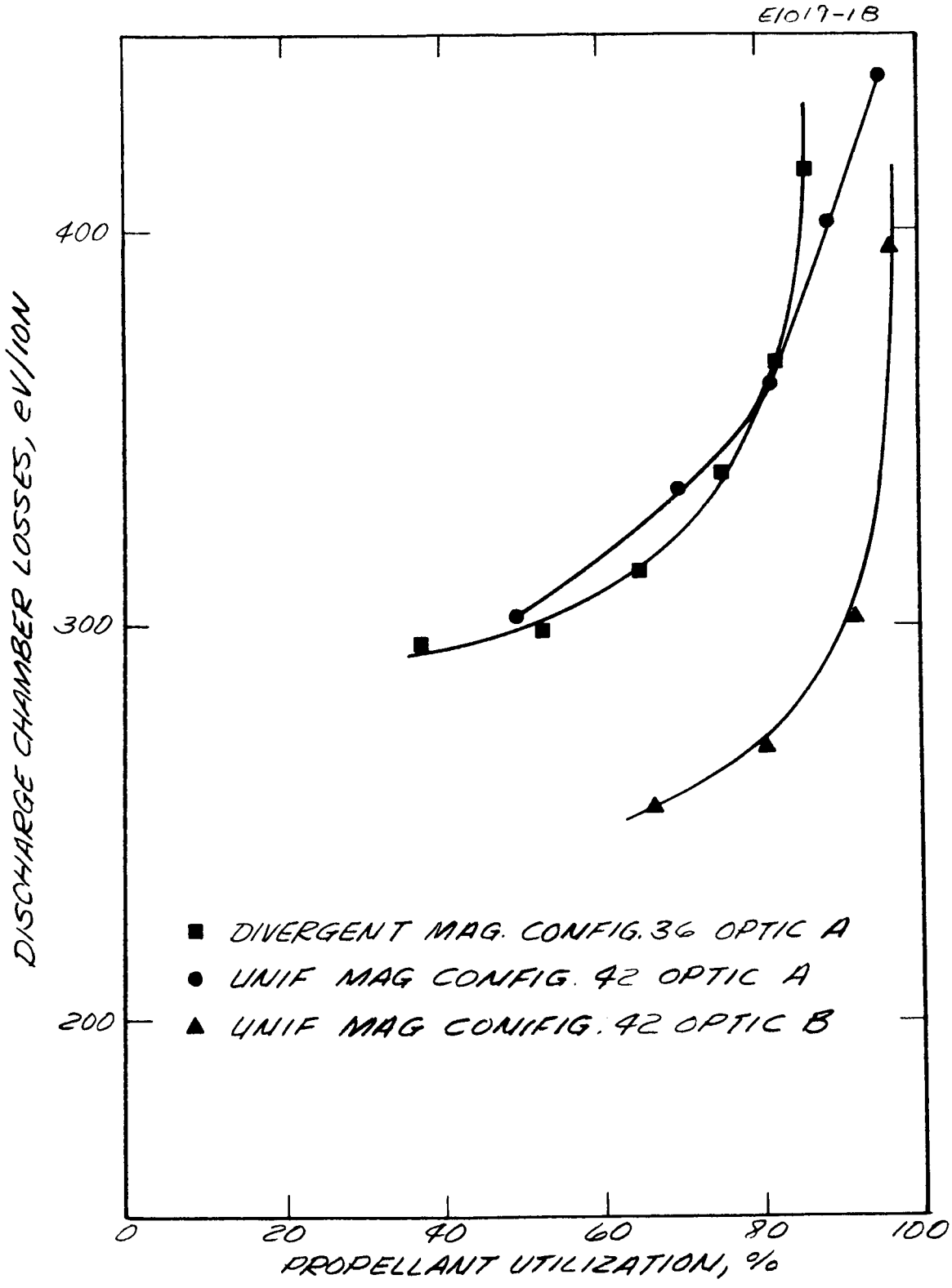

Fig. 41. Performance characteristics of the experimental hollow cathode thruster for two different ion optical systems (magnetic configurations are shown in Figs. 36 and 42). Parameters are given in Table XV.

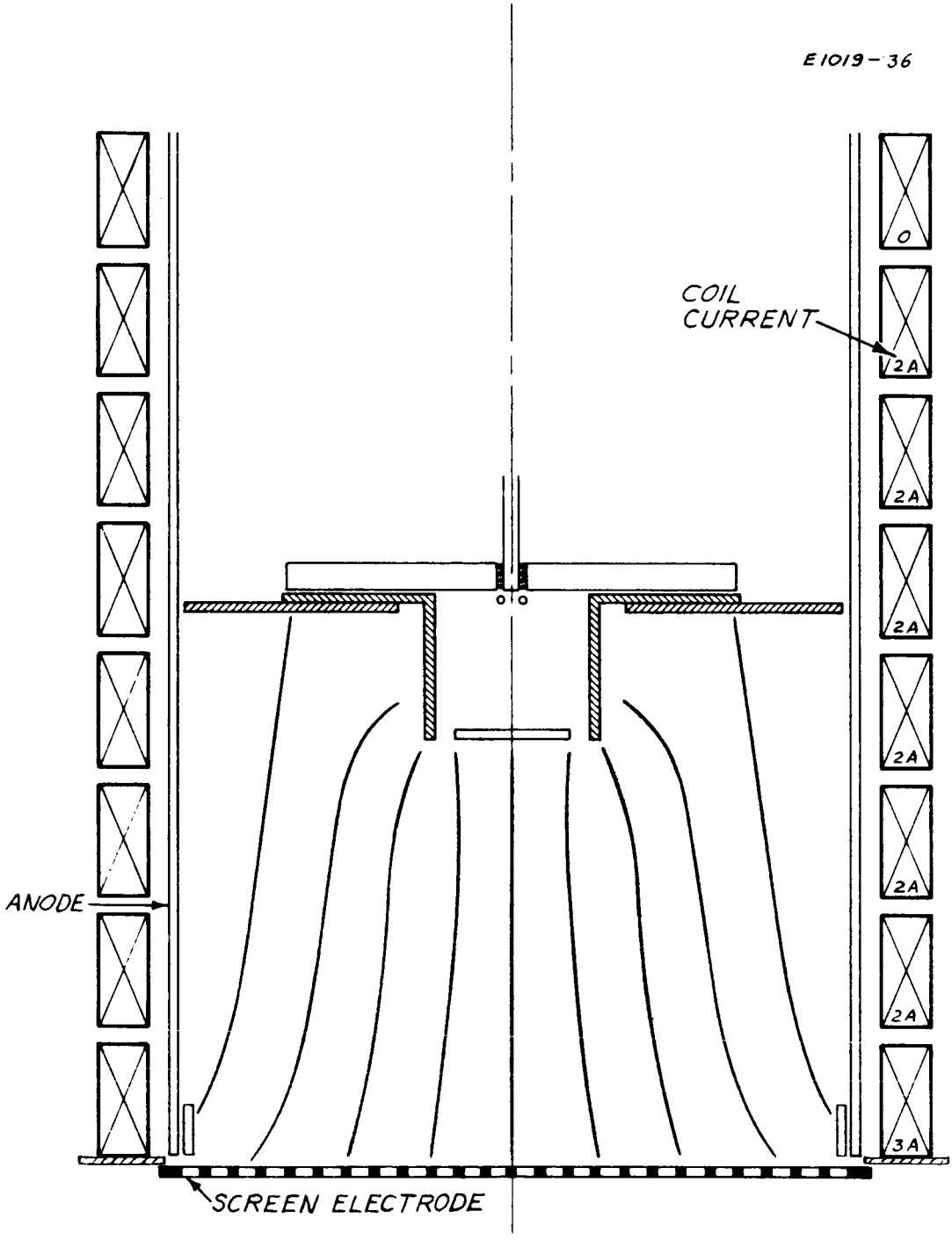

Fig. 42. Magnetic field configuration 42.

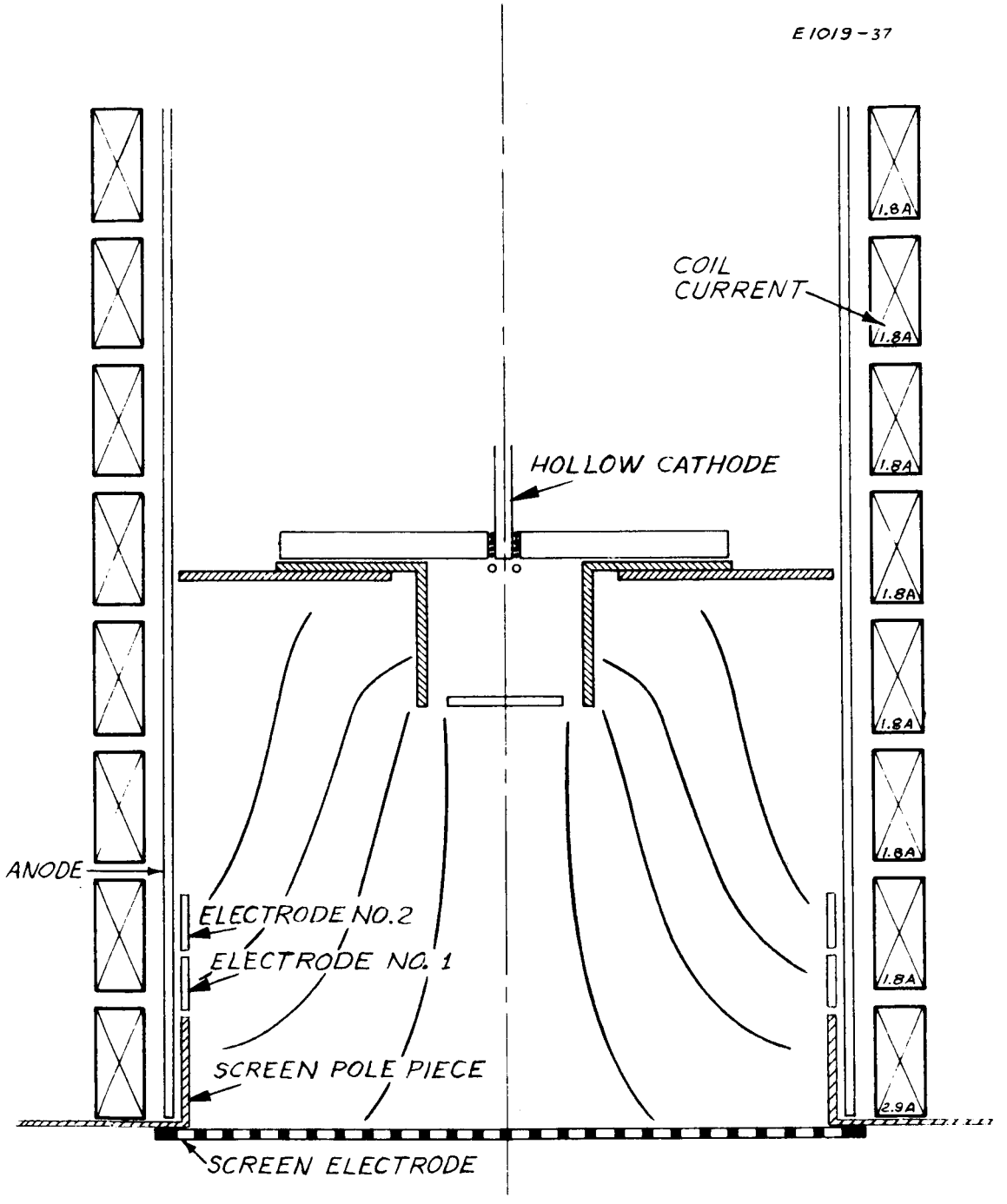

Fig. 43. Magnetic field configuration 43.

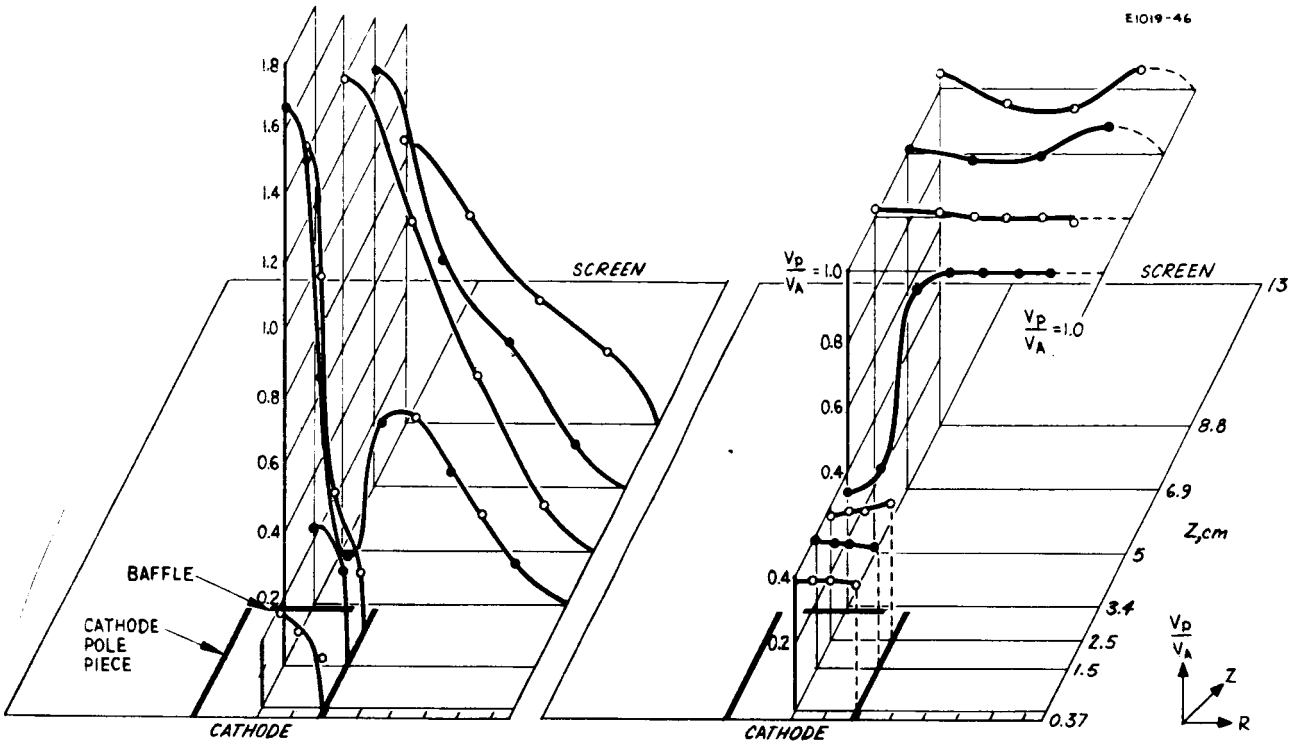

a. PLASMA DENSITY DISTRIBUTION

b. NORMALIZED PLASMA POTENTIAL DISTRIBUTION

OPERATING CONDITIONS

MAGNETIC CONFIGURATION 7D, OPTIC B
STANDARD REVERSE PROPELLANT INJECTION
DISCHARGE VOLTAGE 37V
DISCHARGE CURRENT 17A
ION BEAM CURRENT 298mA
DRAIN CURRENT 0.9 mA

NEUTRAL FLOW 290 mA TOTAL
HOLLOW CATHODE 40 mA
DISCHARGE LOSS 264 eV/ION
PROPELLANT UTILIZATION 82%
ELECTRODE NO. 1 AT CATHODE POT.
ELECTRODE NO. 2 AT ANODE POT.

Fig. 44. Spatial distribution.

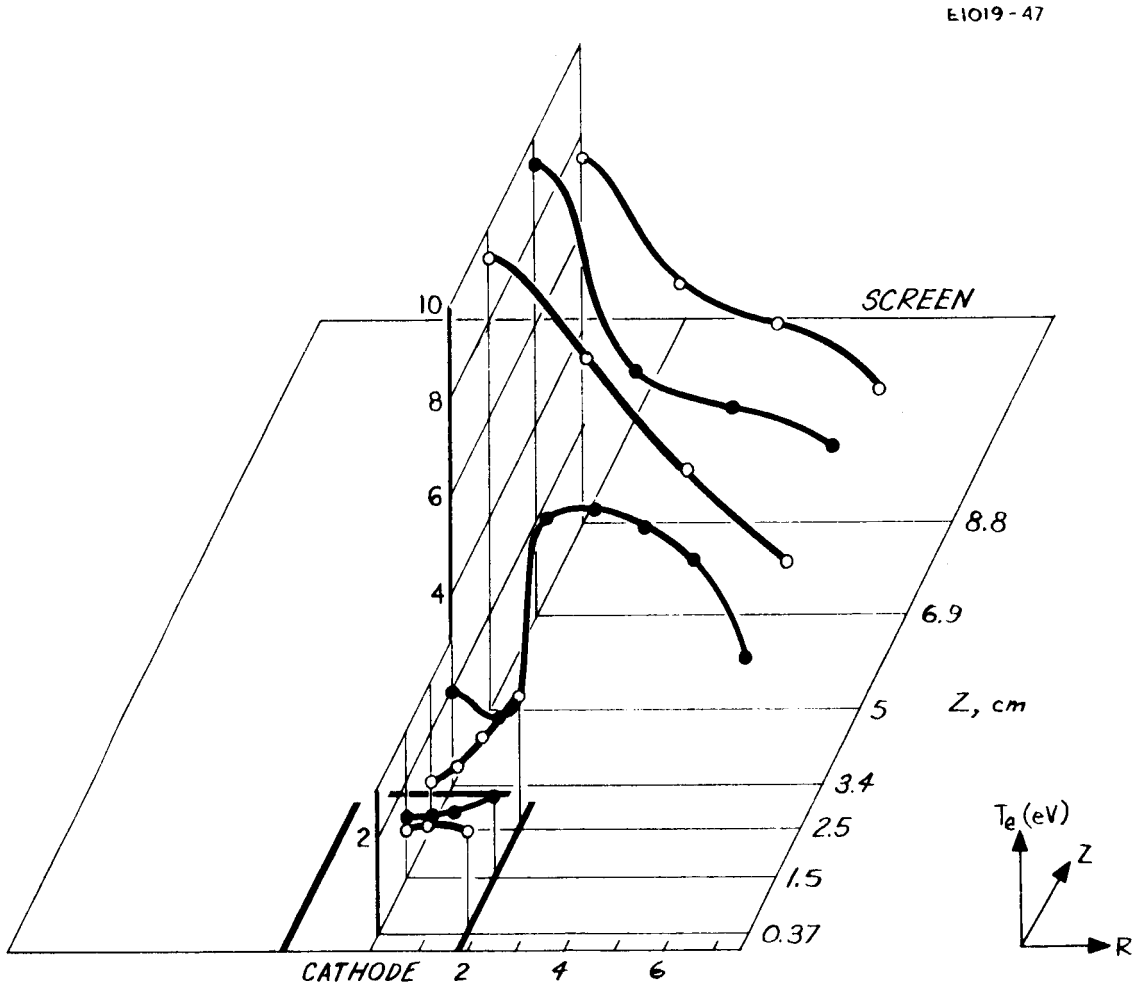

(c) Maxwellian plasma electron temperature in a hollow cathode operated experimental thruster. Probe data obtained with probe 2 shown in Fig. 5. Parameters are given in Table XVI.

Fig. 44. (Cont'd).

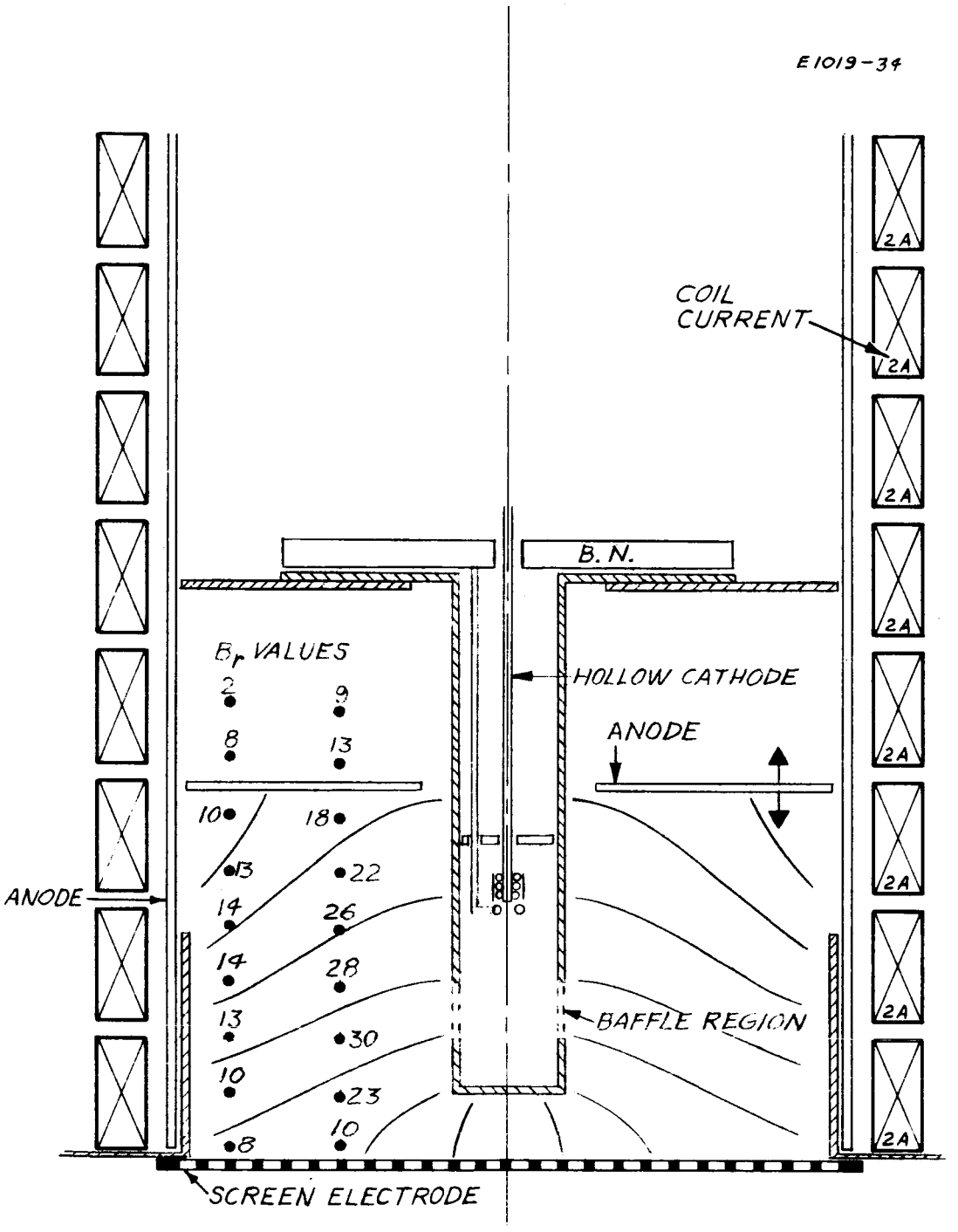

Fig. 45. Radial magnetic field thruster configuration 45.

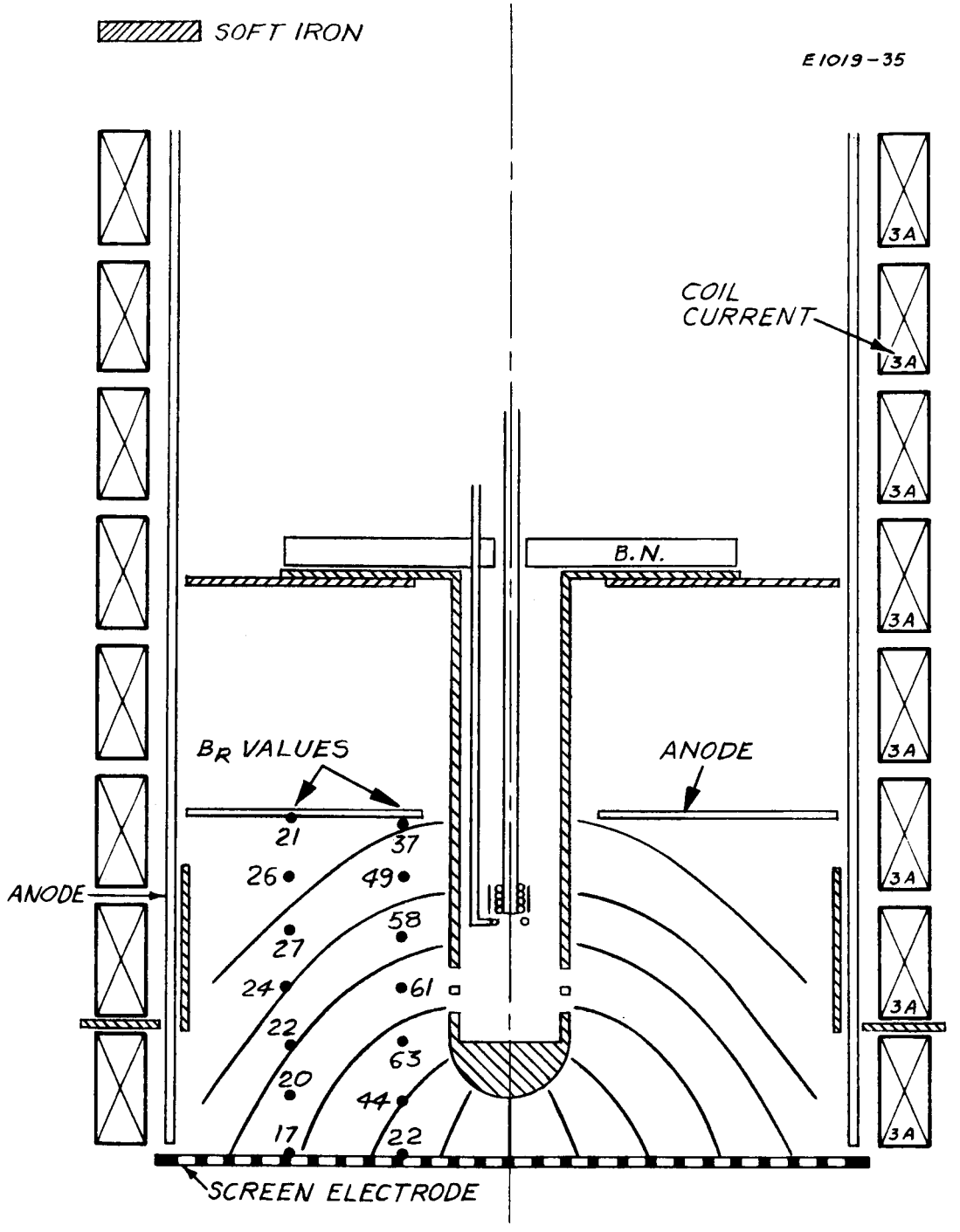

Fig. 46. Radial magnetic field configuration 46.

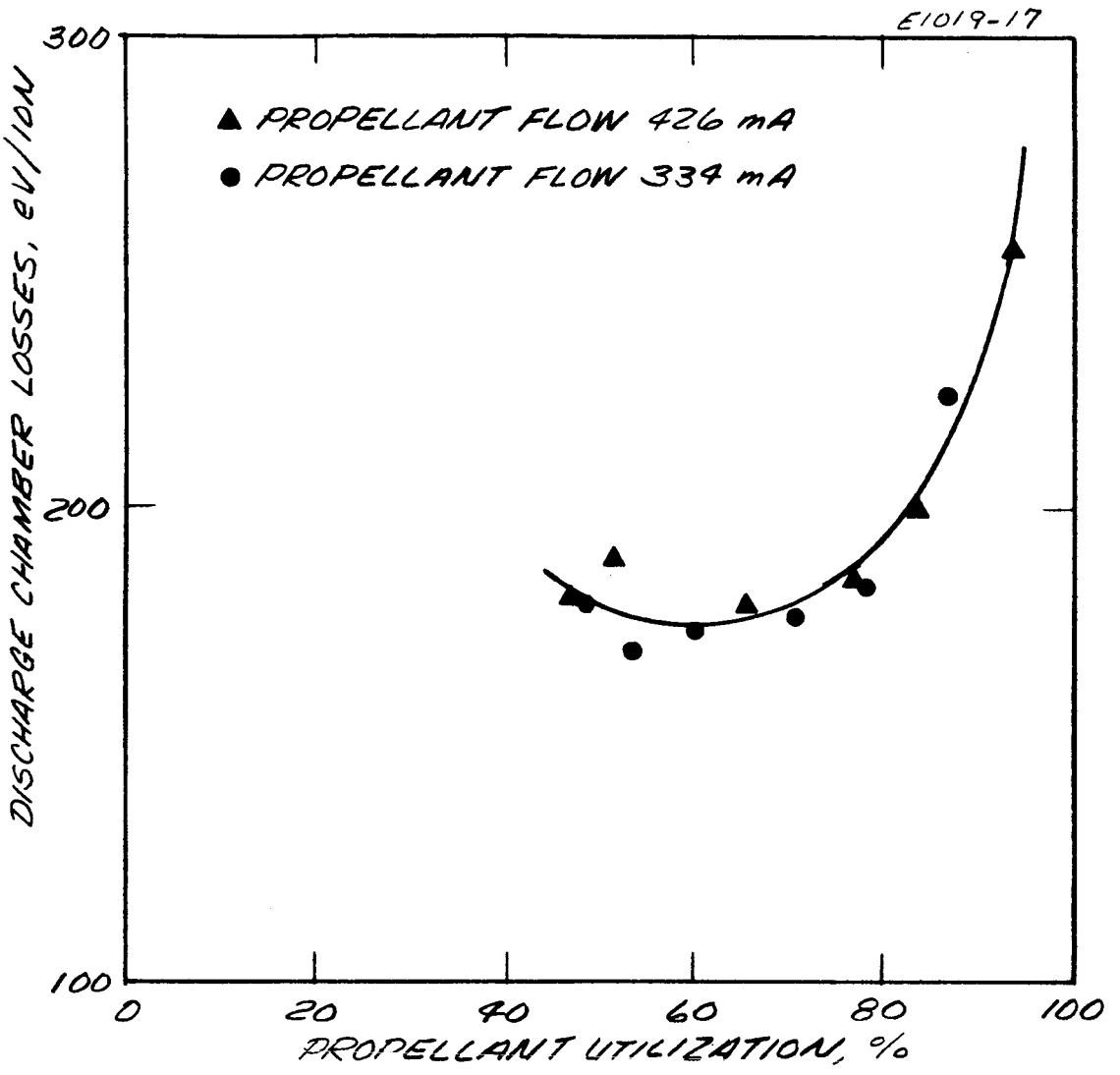

Fig. 47. Performance data of the radio field thruster configuration for different propellant flow levels. Parameters are given in Table XVII.

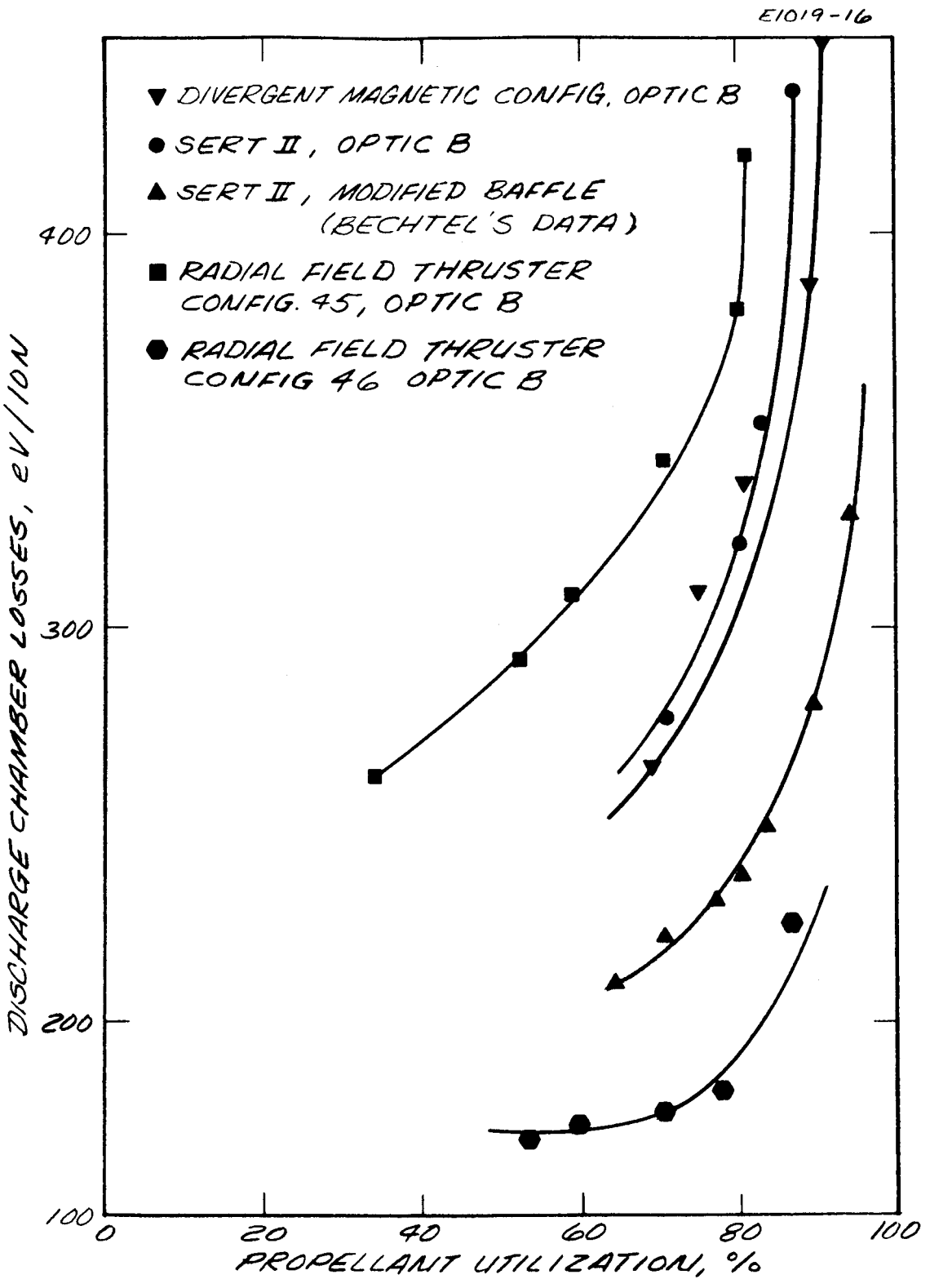

Fig. 48. Performance data for different hollow cathode thruster configurations evaluated under this contract. Also shown are Bechtel's data for the modified SERT-II thruster.

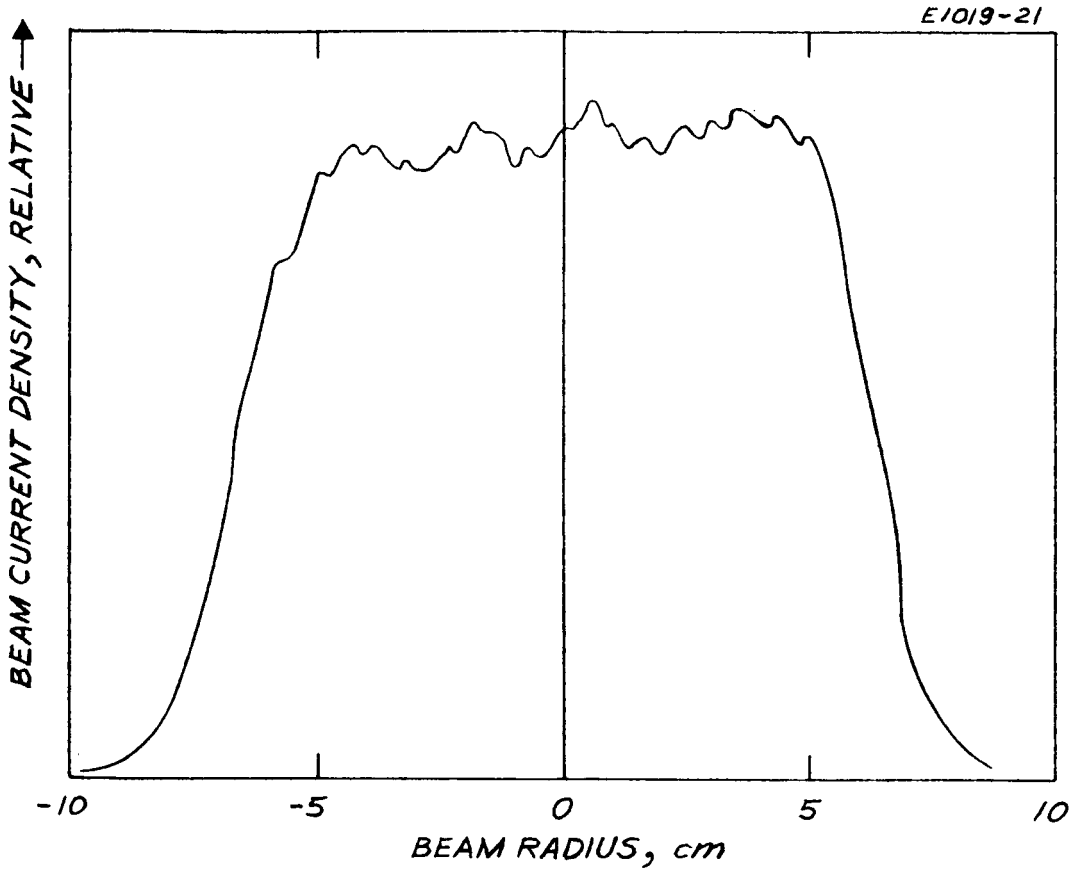

Fig. 49. Beam profile of the radial field thruster; profile measured 1 cm from accel electrode, total ion beam current = 400 mA.

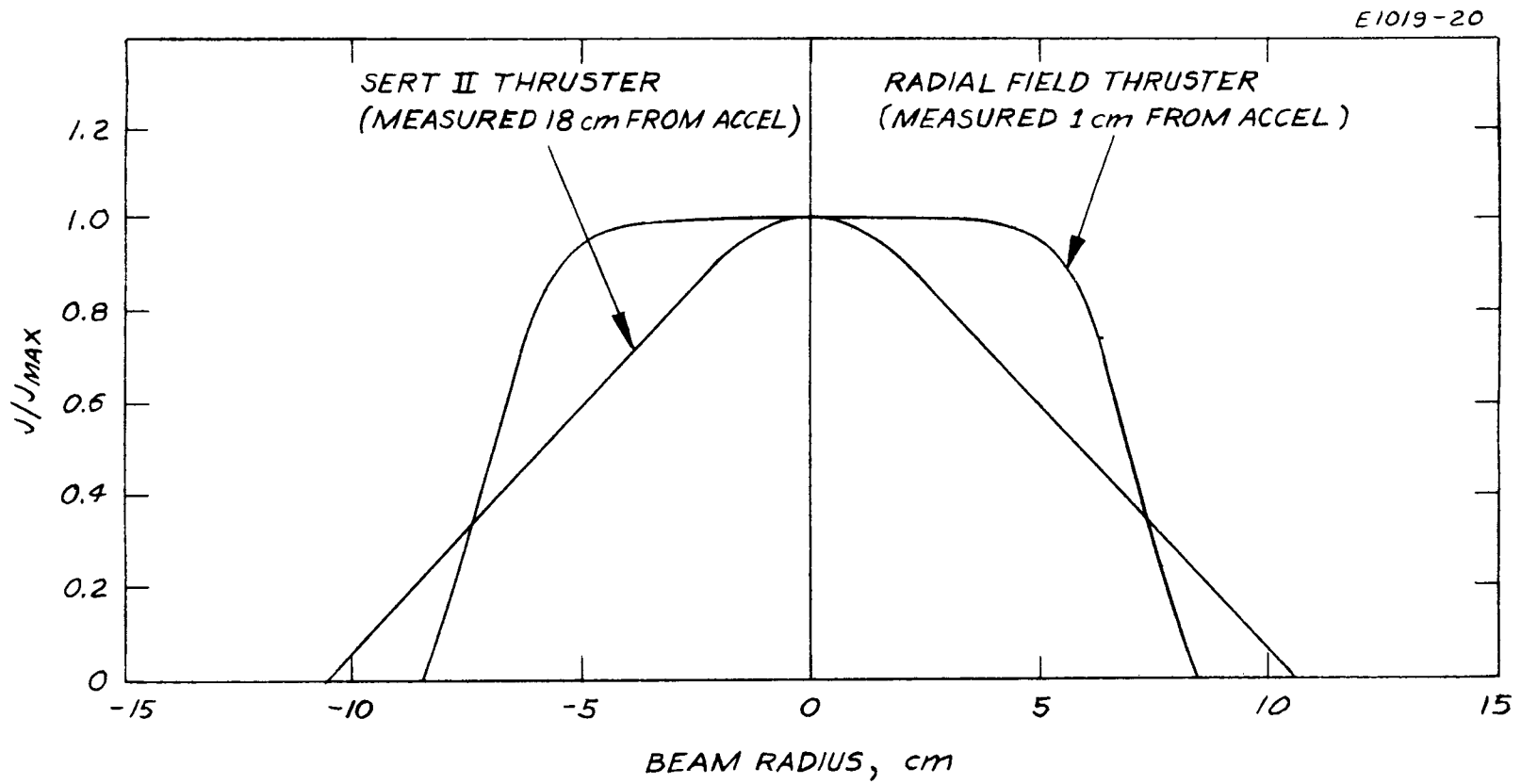

Fig. 50. Normalized and "smoothed" ion beam profiles for the radial field thruster and the SERT-II thruster.

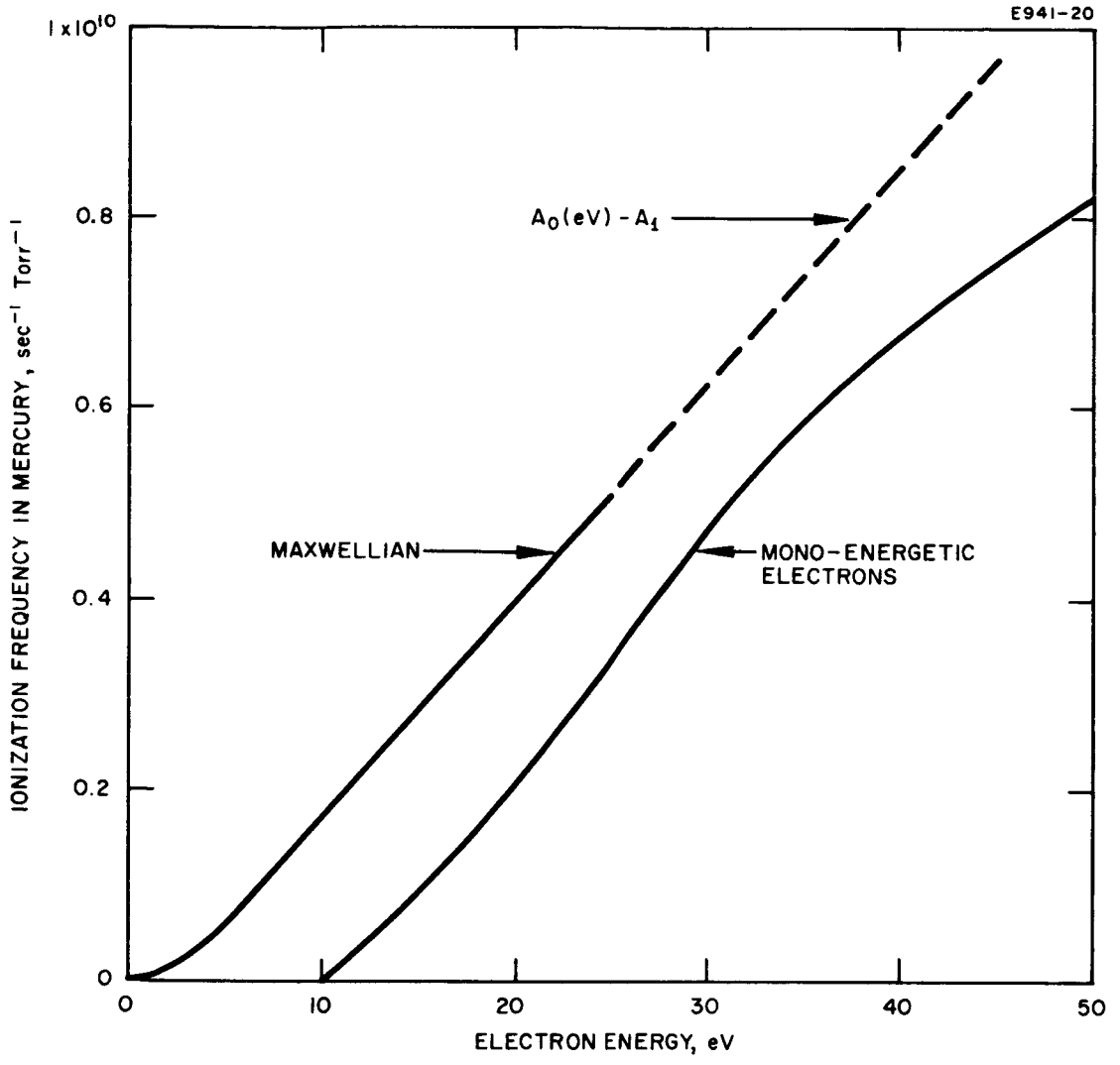

Fig. 51. Ionization rates of monoenergetic and Maxwellian electrons in mercury.

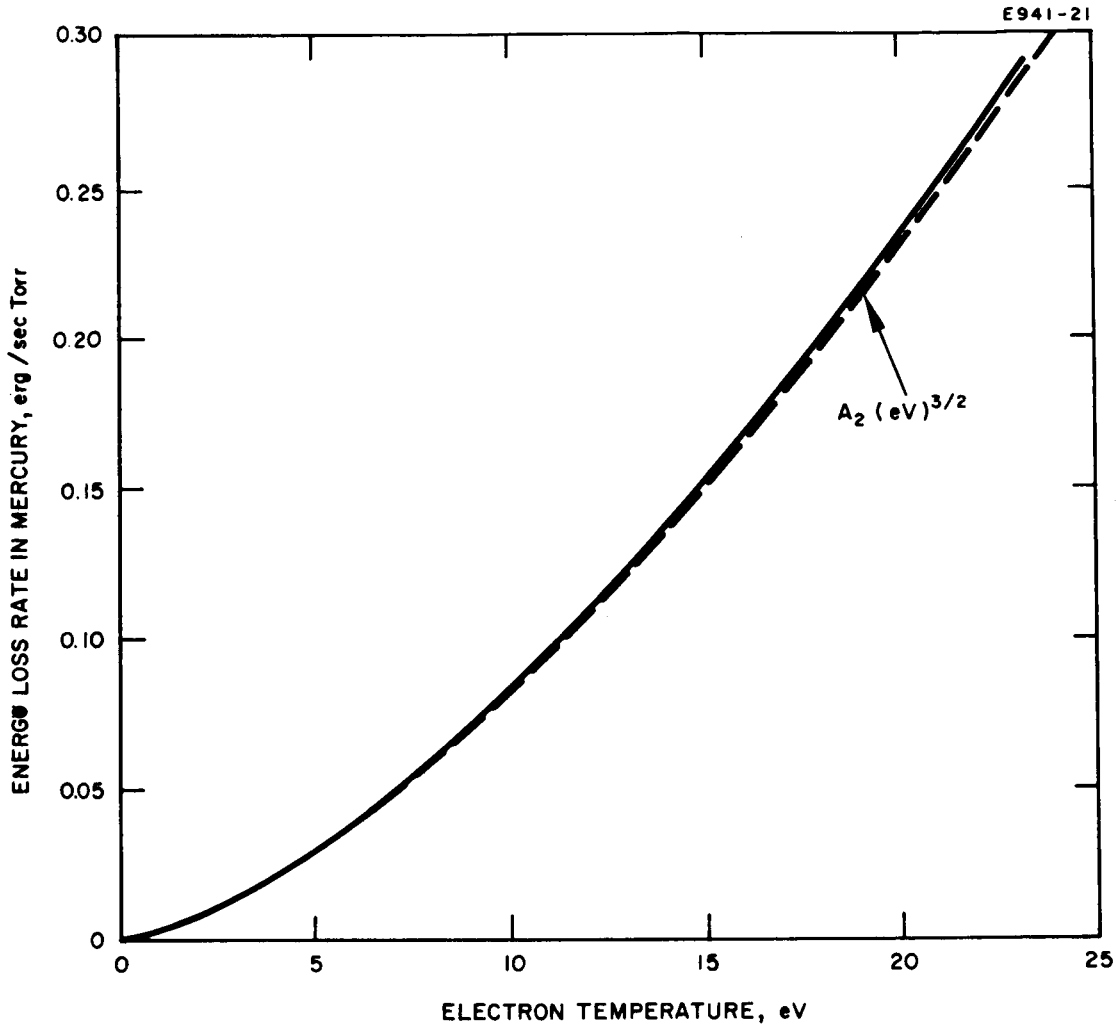

Fig. 52. Energy loss rate of a Maxwellian distribution of electrons as a function of electron temperature in mercury.

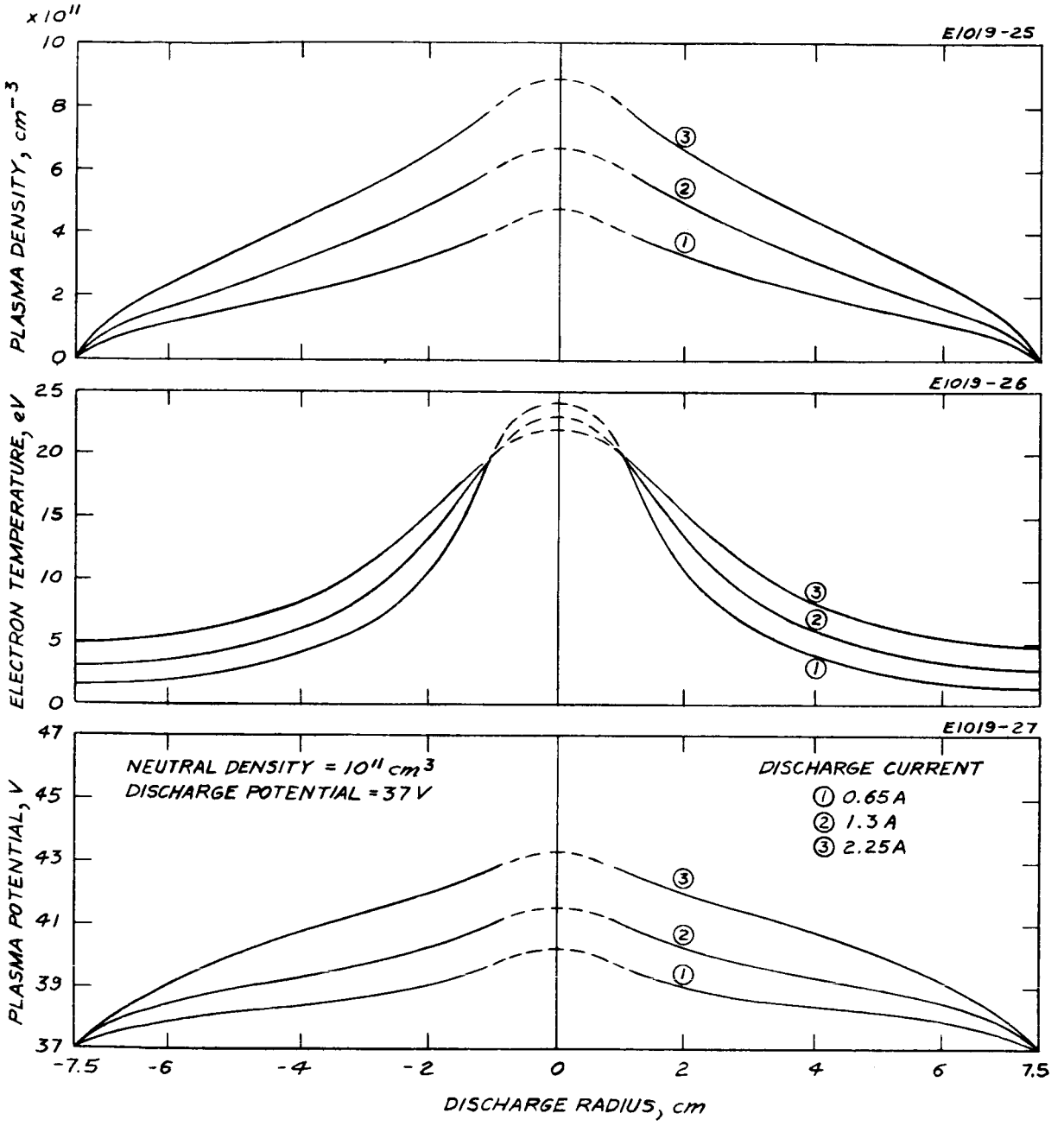

Fig. 53. Theoretically derived plasma density, electron temperature, and plasma potential profiles for a 15 cm diameter thruster.

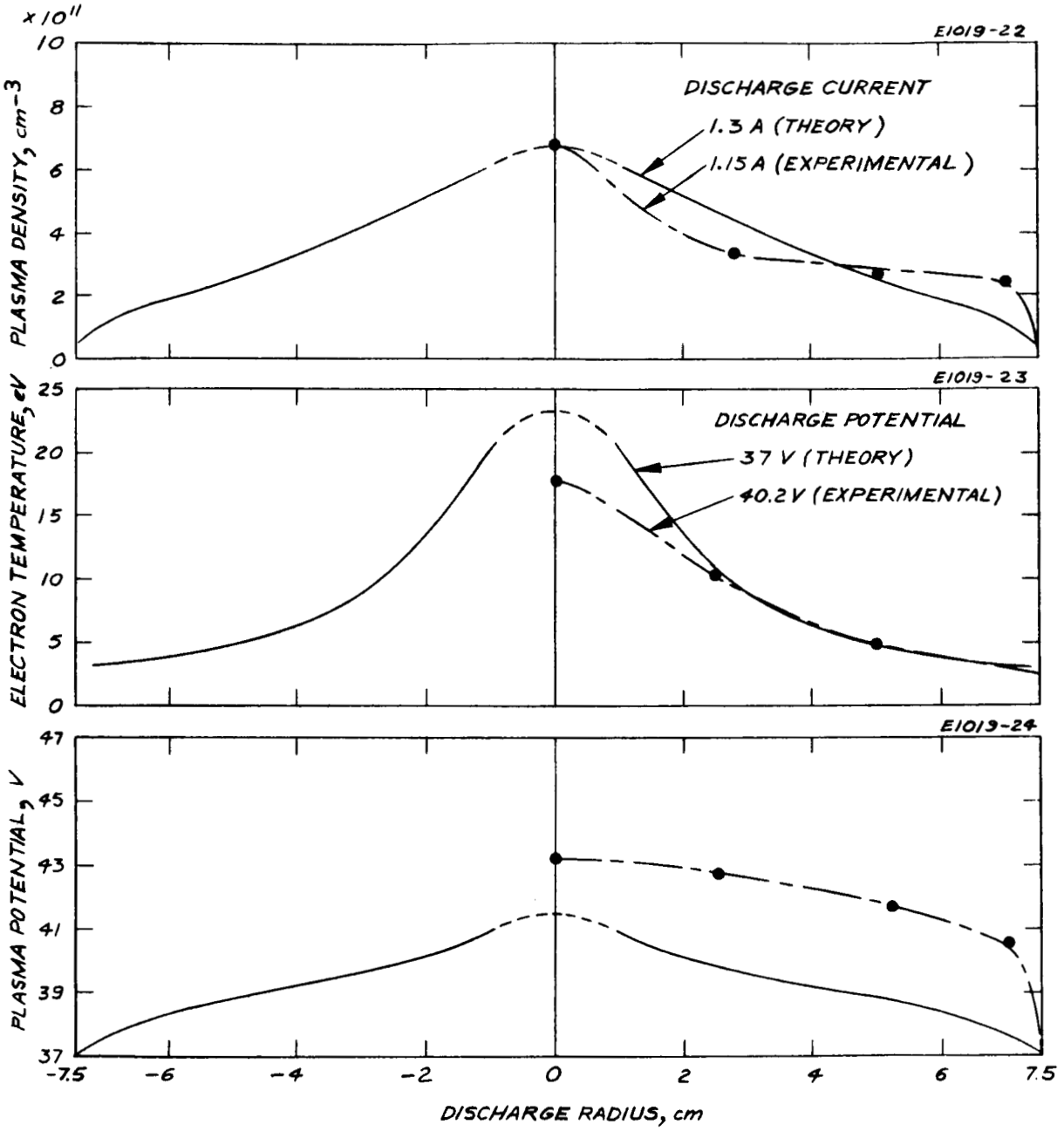

Fig. 54. Comparison of theoretically derived and experimentally observed plasma density, electron temperature, and plasma potential profiles for a 15 cm diameter thruster. The experimental results were obtained with oxide cathode low transmission optics and a uniform magnetic field.

REFERENCES

1. T. D. Masek and E. V. Pawlik, "Thrust System Technology for Solar Electric Propulsion," AIAA Paper 68-541, 4th Propulsion Joint Specialists Conf., Cleveland, June 1968, p. 9.

2. R. T. Bechtel, "Discharge Optimization of the SERT-II Thruster," NASA TMX-52326.

3. R. T. Bechtel, G. A. Csiky, and D. C. Byers, "Performance of a 15 cm Diameter, Hollow-Cathode Kaufman Thruster," NASA TMX-52376.

4. P. D. Reader, "Investigation of a 10 cm Diameter Electron Bombardment Ion Rocket," NASA TN D1163, 1962.

5. P. D. Reader, "Experimental Effects of Propellant Introduction Mode on Electron-Bombardment Ion Rocket Performance," NASA TN D2587, 1965.

6. W. Knauer, and H. Gallagher, "Low Work Function Cathode Development," NASA CR-54682, October 1966.

7. D. W. Maurer and C. M. Pleass, IEEE Electron Device Convention, Washington, D. C., October 1965.

8. F. F. Chen, "Electric Probes," in Plasma Diagnostic Techniques R. H. Huddlestone and S. L. Leonard, Eds. (Academic Press, New York, 1965), Chap. 4, pp. 113-200.

9. I. Langmuir and H. M. Mott-Smith, "The Theory of Collections in Gaseous Discharges," Phys. Rev. 28, 727 (1926).

10. W. B. Strickfaden and K. L. Geiler, AIAA J. 1, 1815 (1963).

11. T. D. Masek and D. J. Kerrisk, JPL Space Programs Summary No. 37-32, Vol. IV.

12. S. Dushman, Scientific Foundations of Vacuum Technique, 2nd ed. Wiley, New York, 1962), p. 32.

13. D. Zuccaro, "Measurement of the Resonant Charge Exchange Cross Section of Mercury and Cesium," AIAA Paper 67-682, AIAA Electric Propulsion and Plasma Dynamics Conference, Colorado Springs, September 1967.

14. F. L. Arnot and G. O. Baines, Proc. Roy. Soc. A151, 256 (1935).

15. W. Bleakney, Phys. Rev. 35, 139 (1930).

16. A. S. Halsted, "Equilibrium Conditions and Beam Focusing Effects in a Beam Generated Plasma," SUIPR Report No. 10, Institute of Plasma Research, Stanford University.